UNIVERSITY OF OKLAHOMA
GRADUATE COLLEGE

IMAGING DEFECTS IN ANTIMONIDE STRUCTURE AND IDENTIFYING THE CAUSES

A THESIS
SUBMITTED TO THE GRADUATE FACULTY
in partial fulfillment of the requirements for the Degree of

MASTER OF SCIENCE

By

Jonathan-David FRANCOIS
Norman,Oklahoma
2019

IMAGING DEFECTS IN ANTIMONIDE STRUCTURE AND IDENTIFYING THE CAUSES

A THESIS APPROVED FOR THE DEPARTMENT OF ENGINEERING PHYSICS

BY THE COMMITTEE CONSISTING OF

Dr. Michael Santos,Chair

Dr. Preston Larson

Dr. Scott Russell

© Copyright by JONATHAN-DAVID FRANCOIS 2019
All rights reserved.

Acknowledgments

In a first time, I would like to deeply thank my advisor Dr. Michael Santos for all the knowledge, advice and support he brought to me in order to complete my thesis research. I would like to thank him for the time spent to teach many materials required to understand this field of study.

In a second time, particular gratitude goes to Dr. Preston Larson for his teaching abilities on every microscope I used throughout all my research and to his amazing availability.

In a third time, I would like to thanks Jeremy Massengale Ph.D. Student in Engineering Physics, and Dr. Rui Q. Yang for providing me many samples to analyze (M and Y series) and giving me the following information and characteristics of each sample.

In a fourth time, I would thank Dr. Scott Russell for teaching the principle of Transmission Electron microscope including manipulating the Zeiss 10A.

My kind regards to Dr. Michael Santos, Dr. Preston Larson and Dr. Scott Russell for being part of my committee.

I want to thank Joyce Hulin and all the faculty and staff of the Department of Physics and Astronomy for their help during my stay at the University of Oklahoma.

I am also thankful to Dr. Jean-Pierre Fontaine for helping me before and throughout my stay here. I would like to thank Dr. Jean-Pierre Fontaine, Dr. Bernard Gruzza and Dr. Joël Leymarie for agreeing to be my French committee.

Moreover, I want to give a special thanks to my family especially my dad for all the love and understanding as well as financial support he gave to me in order to have the possibility to follow this course.

Finally but none the less I would like to thanks my wife Prakairoek François for the indescribable support she brought to me since my first day at the University of Oklahoma and the patience she trusts on a relationship that seems impossible first due to the distance between us.

Contents

1 Background **2**
- 1.1 Molecular Beam Epitaxy . . . 2
- 1.2 Differential Interference Contrast (DIC) Microscope . . . 4
  - 1.2.1 Background and History of DIC . . . 4
  - 1.2.2 Summary . . . 7
- 1.3 Atomic Force Microscopy . . . 7
  - 1.3.1 AFM History and Background . . . 7
  - 1.3.2 Principle of AFM . . . 8
  - 1.3.3 Different Modes of Operation . . . 10
  - 1.3.4 IV. MFP-3D AFM . . . 11
  - 1.3.5 Imaging Modes of the MFP-3D . . . 12
- 1.4 Scanning Electron Microscopy . . . 13
- 1.5 EBSD . . . 17

2 B series InSb Quantum Well **21**
- 2.1 B049 . . . 27
- 2.2 B051 . . . 33
  - 2.2.1 Quality of the scan . . . 39
  - 2.2.2 Orientation Study . . . 41
  - 2.2.3 Grain Determination study . . . 44
- 2.3 Conclusion . . . 45

3 M Series GaSb Buffer Preparation **46**
- 3.1 EBSD Analysis M374 . . . 73
  - 3.1.1 Metallic Droplet Analysis . . . 73
  - 3.1.2 Electron Backscattered Analysis of a Hole Droplet . . . 77
- 3.2 Conclusion . . . 80

4 Y series TPV Interband Cascade Devices **81**
- 4.1 Y064V, 8 Stages without Antimony Soak . . . 83
- 4.2 Y067V, 8 Stages with Antimony Soaks . . . 91
- 4.3 Y074V 15 Stages with Antimony Soaks . . . 99
- 4.4 Y064V Analysis on the Same Area using Different Microscopy Imaging . 112
  - 4.4.1 Y064V EBSD Analysis . . . 116
  - 4.4.2 Quality of the scan . . . 118
  - 4.4.3 Orientation Study . . . 119
  - 4.4.4 Grain Determination Study . . . 121
- 4.5 Conclusion . . . 122

5 Conclusion **124**

Appendices **129**

A Electron Backscattered Diffraction of a Hole Droplet on the surface of M374 **129**
A.1 Quality of the scan 130
A.2 Orientation Study 131

List of Figures

1 Diagram of Molecular Beam Epitaxy growth chamber [32]. 3
2 Diagram of a DIC microscope [24]. 5
3 Differential Interference Contrast Schematic [24]. 6
4 First model of AFM using a scanning transmission microscope tip [14]. . 8
5 AFM principle [20]. 8
6 AFM binding effect occuring on the tip when it gets closer to the surface. 9
7 Process to obtain an image. 10
8 Schematic of the different AFM mode of imaging. 11
9 Setup of the MFP-3D. 12
10 SEM imaging principle [18]. 15
11 SEM column overview [13]. 15
12 Interaction volume representation [13]. 16
13 Close up of objective lens region on SEM with the representation of the different detectors used in the normal imaging mode [34]. 17
14 Simulation of electron backscattered diffraction patterns [1]. 18
15 Diffraction case. 19
16 Bragg's Law diffraction schematic. 19
17 Epilayer composition of B051 and B049. 21
18 Example of a heterojunction in which heavily n-type AlGaAs is grown on lightly doped GaAs [4]. 21
19 Example of a heterojunction in which heavily n-type AlInSb is grown on undoped InSb. 22
20 Figure (a) :Zinc Blende structure schematic [5] , Figure (b) : Crystallographic notation schematic [21]. 23
21 Bandgap as a function of lattice constant for non-nitride III–V compound semiconductors (points) and their random ternary alloys (lines) at zero temperature. 24
22 Lattice Matching process. 25
23 Critical thickness vs mismatch calculated in the case of B049 and B051. . 26
24 B049 background taken with the AFM. 27
25 3D representation of B049 Background. 27
26 Data analysis of B049 Background. 28
27 B049 background taken with the SEM ZEISS NEON. 28
28 Line defects due to misfit dislocations taken with the AFM. 29
29 3D representation of the line defects due to misfit dislocation observed on the surface of B049. 29
30 Data analysis of the line defects due to misfit dislocations taken with the AFM. 30
31 B049 background image taken at different magnifications (10x to 100x) with the DIC microscopes. 31
32 Line defects due to misfit dislocations zoom taken with the AFM. 31

33 3D representation of the line defects due to misfit Dislocation zoom observed on the surface of B049. 32
34 Data analysis of the line defects due to misfit dislocation zoomed taken with the AFM. 32
35 Misfit Dislocation Zoom taken with the DIC microscope. 33
36 Overall B051 background taken at a different magnification with the DIC microscope. 34
37 Overall B051 background taken at a low magnification (60 μm wide by 60 μm long) taken with the AFM. 34
38 3D representation of the B051 background. 35
39 B051 data analysis of the background surface. 35
40 B051 SEM background micrographs. 36
41 B051 DIC line defects due to misfit dislocations. 36
42 B051 data analysis of the line defects due to misfit dislocations taken with the AFM. 37
43 3D representation of B051 Background using a close field of view (7 μm wide by 7 μm long) taken with the AFM. 37
44 Data analysis of the B051 background using a close field of view (7 μm wide by 7 μm long) taken with the AFM. 38
45 B051 defects taken with the FE-SEM ZEISS Neon 40 EsB. 38
46 Map of the EBSD analysis on B049 line defects due to misfit dislocations. 39
47 Mean Angular Deviation (MAD) map and band contrast map which give information about the quality of the scan. 40
48 Inversion pole figures of the line defects due to misfit dislocations present on the surface of B049. 42
49 Phase map of the line defects due to misfit dislocation on the surface of B049. 43
50 Inversion pole figure map with direct projection. 43
51 Grain determination analysis for a tolerance angle of 1.5 degrees. 44
52 Everhart thornley imaging and In Lens detector image taken with the SEM ZEISS NEON at low magnitude (184 X). 47
53 AFM images of the M371 background, figure (a) the height channel which provides useful information about the height of the defects on the sample and figure (b) the amplitude channel which gives the closest representation to what one would be able see using a light microscope. 48
54 Data analysis of the M371 background taken with the Atomic Force Microscope. 48
55 3D representation of M371 background. 49
56 M371 background taken with the DIC Microscope at 40x. 49
57 Holes droplets of M371 taken with the SEM ZEISS NEON. 50
58 Hole droplets from 10x to 100x taken with the DIC Microscope. 51
59 Metallic droplets taken with the SEM ZEISS NEON. 51
60 Metallic droplets from 10x to 40x taken with the DIC Microscope. 52

61 AFM images of an irregularity in M371. 53
62 3D representation of the M371 irregularity present on the surface. 53
63 Data analysis of the M371 irregularity. 53
64 Pyramidal defects observed on the surface of M371 taken with the AFM microscope. 54
65 3D representation of the pyramidal defects on the surface of M371. . . . 54
66 Pyramidal defects observed with the AFM microscope. 55
67 Background of M372 taken with the ZEISS NEON. 56
68 M372 background observed on the AFM. 56
69 3D representation of M372 Background. 57
70 Data analysis of the M372 sample surface. 57
71 M372 background taken with the DIC Microscope. 57
72 Defect formation along a scratch on the surface of M372 taken with the ZEISS NEON at different magnifications. 59
73 M372 defects along a scratch taken with the DIC Microscope. 60
74 Multiple metallic droplets formation on the surface of M372 taken with the ZEISS NEON. 60
75 Multiple metallic droplets, holes droplets and right angles line defects on the surface of M372 taken with the ZEISS NEON. 61
76 M372 metallic droplets taken with the DIC Microscope. 62
77 SEM micrographs of M373 background. 63
78 M373 background taken with the DIC Microscope. 64
79 M373 background micrographs taken with the AFM. 65
80 3D representation of M373 background. 65
81 Data analysis of M373. 66
82 Hole droplet on the surface of M373. 66
83 Hole and metallic droplet on the surface of M373. 67
84 M373 droplets taken with the DIC Microscope. 67
85 Background of M374 taken with the ZEISS NEON. 68
86 DIC micrograph of the M374 background. 69
87 AFM micrograph of the M374 background. 69
88 3D representation of M374 Background. 70
89 Data analysis of the M374 background. 70
90 Metallic droplets in M374 taken with the ZEISS NEON. 71
91 M374 metallic droplets taken with the DIC Microscope. 72
92 Metallic droplet on the surface of M374 taken with the AFM. 72
93 3D representation of the metallic droplet on the surface of M374 imaged with an AFM. 73
94 Data analysis of the metallic droplet on the surface of M374. 73
95 Secondary image of the metallic droplet in M374. 74
96 Band contrast map and Mean Angular Deviation (MAD) map of the metallic droplet taken on the surface of M374. 74

97 Inversion Pole Figure X,Y,Z map of the metallic droplet taken on the surface of M374. 76
98 Inversion Pole Figure map with direct projection on the surface of M374. 77
99 Secondary image of a hole droplet on the surface of M374 used for the EBSD analysis. 77
100 Mean Angular Deviation (MAD) map and band contrast map of the hole droplet taken on the surface of M374. 78
101 Inversion Pole Figure X,Y,Z of the hole droplet. 79
102 Inversion Pole Figure map with direct projection of the hole droplet analysis. 79
103 Band diagram of a three stages in a typical interband cascade photovoltaic prototype [31]. 81
104 Cascade diagram process in an quantum cascade device. 82
105 AFM height channel image and amplitude image of the background of Y064V. 83
106 3D representation of the background of Y064V. 83
107 Data Analysis of the Background of Y064V. 84
108 DIC images at 10x in figure (a) and at 20x in figure (b) of the background of Y064V 84
109 DIC micrographs (a,b) and (c) at 100x of the hillocks that we can encounter on the surface of Y064V. 85
110 SEM hillock images that we encounter on the surface of Y064V, taken with the ZEISS Neon 40 EsB at low magnification (1kX). 86
111 AFM height channel image and amplitude image on a massive hillock area on the surface of Y064V. 87
112 Data analysis of AFM height on a massive hillock area on the surface of Y064V. 87
113 3D representation on a massive Hillock area on the surface of Y064V . . 88
114 Figure (a) AFM height channel and Figure (b) amplitude channel of a zoomed hillock area on the surface of Y064V at high magnification. . . . 88
115 3D representation of a zoomed hillock area on the surface of Y064V. . . . 89
116 Data analysis of a zoomed hillock area on the surface of Y064V. 89
117 Schematic to define the X-axis and the Y-axis in the hillock measurement. 89
118 SEM hillock images that we encounter on the surface of Y064V, taken with the ZEISS Neon 40 EsB at higher magnification (4kX). 90
119 Hole droplet images that we encounter on the surface of Y064V taken with the ZEISS Neon 40 EsB. 90
120 X-ray diffraction (XRD) scans of Y064V and Y067V. 91
121 SEM micrographs of the background of Y067V taken with the ZEISS Neon 40 EsB. Both images were taken using the Everhart-Thornley detector but at different magnifications. 92

122 SEM micrographs of the background of Y067V taken with the ZEISS Neon 40 EsB. Both images were taken using the backscattered detector present on the EBSD camera. The sample was tilted by 70 degrees with respect to the beam using the appropriate EBSD sample holder. 93
123 Background micrographs of the surface of Y067V taken with the DIC Microscope. The top images were taken at 10x and 20x whereas the bottom ones were taken at 40x. 93
124 AFM height channel image and amplitude image of the background of Y067V. 94
125 3D representation of the background of Y067V. 94
126 Data analysis of the background of Y067V. 95
127 SEM hillock images on the surface of Y067V taken with the ZEISS Neon 40 EsB. Every image was taken with the Everhart-Thornley detector. . 96
128 SEM images of the hillock present on the surface of Y067V taken with the ZEISS Neon 40 EsB. Every images was taken using backscattered detector present on the EBSD camera. The sample was tilted by 70 degrees using the appropriate EBSD sample holder. 97
129 AFM height channel image and amplitude image of another hillock present on the surface of Y067V. 98
130 3D representation of another hillock present on the surface of Y067V. . . 98
131 Data analysis of another hillock present on the surface of Y067V. 98
132 Metallic droplet on the surface of Y067V taken with the ZEISS Neon 40 EsB at high magnification (17 kX). 99
133 X-ray diffraction (XRD) scan of Y074V. 100
134 Background of Y074V taken with the ZEISS Neon 40 EsB. The left-hand side image was taken with the Inlens detector and the right-hand side with the Everhart-Thornley detector. 100
135 SEM micrographs of background of Y074V, taken with the ZEISS Neon 40 EsB. Every images was taken using the backscattered detector present on the EBSD camera. The sample was tilted by 70 degrees with respect to the primary beam using the appropriate EBSD sample holder. 101
136 AFM height channel image and amplitude channel image of the background of Y074V. 102
137 3D representation of the background of Y074V. 102
138 Data analysis of the background of Y074V. 103
139 Background of Y074V taken with the DIC Microscope at different magnifications. Figure (a) was taken at 10x, Figure (b) was taken at 20x and Figure (c) was taken at 40x. 104
140 AFM height channel image and amplitude channel image of hillocks present on the surface of Y074V. 105
141 3D representation of Hillocks present on the surface of Y074V. 105
142 Data analysis of hillocks present on the surface of Y074V. 106

143 SEM micrographs of hillocks and new defects present on the surface of of Y074V taken with the ZEISS Neon 40 EsB. Every micrograph was taken using the backscattered detector present on the EBSD camera. The sample was tilted by 70 degrees with respect to the primary beam using the appropriate EBSD sample holder. 107
144 AFM height channel image and phase channel image of a new type of defect present on the surface of Y074V. 108
145 3D representation of a new type of defect present on the surface of Y074V. 108
146 Data analysis of a new type of defect present on the surface of Y074V. . 109
147 AFM height channel image and amplitude channel image of another type of new defect present on the surface of Y074V. 109
148 3D representation of another type of new defect present on the surface of Y074V. 110
149 Data analysis of another type of new defect present on the surface of Y074V. 110
150 AFM height channel image and amplitude channel image of pyramidal defects present on the surface of Y074V. 111
151 3D representation of pyramidal defects present on the surface of Y074V . 111
152 Data analysis of pyramidal defects present on the surface of Y074V. . . . 112
153 DIC images of the hillocks present on Y064V used for an analysis using different microscopes. The images were taken at different magnifications (10x to 100x). 113
154 SEM micrographs of the hillocks present on Y064V used for an analysis using different microscopes taken with the ZEISS Neon 40 EsB in two different configurations. 114
155 SEM micrographs of the hillocks present on Y064V used for a analysis using different microscopes taken with the ZEISS Neon 40 EsB. The image was taken at different magnifications in the EBSD configuration (sample titled by 70 degrees) with the BSE detector present on the EBSD camera. 114
156 Height channel image and amplitude image of the hillock present on Y064V used for a analysis using different microscopes, taken with the Atomic Force Microscope. 115
157 3D representation of the hillock present on Y064V used for an analysis using different microscopes taken with the Atomic Force Microscope. . . 115
158 Data analysis of the hillocks present on Y064V used for an analysis using different microscopes taken with the Atomic Force Microscope. 116
159 Backscattered image used for the EBSD analysis of hillocks present on the surface of Y064V. 117
160 Mean Angular Deviation (MAD) and band contrast map of the EBSD analysis of hillocks present on the surface of Y064V 118
161 Inversion Pole Figure X,Y,Z map of the EBSD analysis of hillocks present on the surface of Y064V. 119
162 Phase map of the EBSD analysis of hillocks present on the surface of Y064V. 120

163 Inversion Pole Figure map with direct projection of the Hillock present on the surface of Y064V. 120
164 Grain determination map of the hillock present on the surface of Y064V for a tolerance angle of 5 degrees. 121
165 Grain determination map of the hillocks present on the surface of Y064V for a tolerance angle of 3 degrees. 122
166 Secondary image of the first hole droplet on the surface of M374 used for the EBSD analysis. 129
167 Mean Angular Deviation (MAD) map and Band contrast Map of the first Hole Droplet taken on the surface of M374. 130
168 Inversion Pole Figure X,Y,Z of the first hole droplet. 131
169 Inversion Pole Figure map with direct projection of the first hole droplet. 131

List of Tables

1 Different AFM modes. 10
2 Advantages and disadvantages of AFM modes. 10
3 Description of the samples of the M series. 46
4 M series data table. 80
5 Hillocks characteristics of the Y series table. 122
6 Background Irregularities table. 123

List of Equations

1 Hooke's Law 1 9
2 Abbe's equation for a light microscope 2 14
3 Abbe's Equation for Electron Microscope 3 14
4 Bragg's Law 4 20
5 Hall Effect Voltage 5 22
6 Distance between two adjacent planes 6 23
7 Lattice matching equation 7 25
8 Equilibrium condition 8 25
9 ϵ_T 9 26
10 Homogenous strain energy density equation 10 26
11 Dislocation's Energy density equation 11 26
12 Spacing between dislocations 12 26
13 Critical Thickness 13 26

Abstract

This thesis is divided into three studies, all using microscopy techniques. All the structures were grown by molecular beam epitaxy.

In the first study, we compared two InSb quantum well devices with the same structure. A conclusion was made that the theoretical layer structure that was used for the two samples is marginally inaccurate and results in structures that are marginally strain balanced. The presence of lines due to misfit dislocations were noticed in both samples even though the second sample, B051, has a better surface condition with minimized lines due to misfit dislocations compared to the first sample B049.

In the second study, we compared four different GaSb homoepitaxial samples to explore the effects of different growth conditions. The samples were a 1-μm GaSb layer grown on a GaSb substrate. These experiments were aimed at finding the best growth parameters to make the buffer layer as smooth as possible. The best sample of this study was M373, with the highest growth temperature of 498°C and a V/III ratio of 2.5. It had the lowest density of defects on its surface. Another sample of this study, M374, had also interesting properties, with the smoothest background and shallowest irregularities of this study. Unfortunately, a higher density of defects in comparison to M373 was observed due to a lower V/III ratio, which caused the desorption of group V material and increased the metallic droplet density on its surface.

Lastly, in the third study, experiments involving three interband cascade photovoltaic prototypes were conducted. Two of them had 8-stages with one employing Antimony soaks during the growth (Y067V) and the other did not (Y064V). The last sample, Y074V, was a 15-stages device with antimony soaks during the growth. The effect of the Antimony soak process and of increasing the number of stages in this study was compared. An improvement in the surface condition with the Antimony soak was observed. Indeed the density of hillocks on the surface of Y067V was 50 times smaller than the density of hillocks of Y064V by adding this Antimony soak process during the growth. The reason was that the residual Arsenic present in the chamber interfered with the composition of the layer one was trying to grow after an arsenide layer. AlAs or AlAsSb layers were created which made the overall semiconductor not strain balanced. The last sample of this study, Y074V, had also some interesting properties, with a shallower average hillock height and a smaller hillock size observed on its surface. However, a hillock density 5 times higher than Y067V was observed which means that some improvements are needed for structures with many stages.

Introduction

The 6.1 $\AA$ III-V compound semiconductors, including GaSb, GaAs, AlSb and their related alloys are an important family of materials for solid states electronic devices such as optoelectronic devices, including lasers, light emiting diodes and thermophotovoltaics. This dissertation is composed of four sections :

The first section explains the overall background needed to understand three independent studies of semiconductor growths. The characterization methods used such as Scanning Electron Microscopy, Atomic Force Microscopy and Differential Interfence Contrast Microscopy. This section also presents the equipment needed to grow semiconductors using Molecular Beam Epitaxy.

Epitaxial growth of high-quality material requires minimizing surface defect densities to minimize nonradiative recombination rates and maximize device yield. High quality first require with growth of smooth buffer layers free of defects. Section three focuses on this issue, using a GaSb substrate and growing a 1-micron GaSb epilayer on it with the aim of minimizing the defect densities by exploring diverse growth conditions.

Sections one and four focus on two independent studies. In section one, we focus on two Indium Antimony quantum well structures. The first one, labeled B049, is a wafer of 1 micron InSb/AlInSb epilayers on a GaAs substrate. The second one B051 is a prototype of a Hall effect sensor using the same layer composition as B049 but after device processing. In section four, a study of interband cascade photovoltaic devices will be conducted. Indeed the cascade process involves a high number of stages, which requires very thick structures. A clear understanding of the surface condition is needed to grow high-quality structures.

1 Background

In this chapter, a detailed explanation of the equipment used either for characterization techniques or growth of the semiconductors will be presented.

1.1 Molecular Beam Epitaxy

In this section, a brief discussion of producing high quality crystalline semiconductors using Molecular Beam Epitaxy (MBE) will be presented.[7] [12]. MBE was initially developed by J. R. Arthur and A. Y. Cho for growth of GaAs and $GaAs/Al_{(x)}$ $Ga_{(1-x)}$ As structures.

MBE is essentially a UHV-based evaporation method. It is a material deposition technique capable of predictably and reproducibly yielding material with impurity levels below ten parts per billion, with unprecedented control over the precision with which the composition and doping of the structure can be designed. Some of these attributes are intrinsic to the MBE process, e.g., slow growth rates and low deposition temperatures. Others, such as material quality and purity, rely on the technology employed.

MBE has now been extended to a wide variety of materials while maintaining key advantages over other techniques of epitaxial film growth such as chemical vapor deposition (CVD), liquid phase epitaxy (LPE), metal-organic vapor phase epitaxy (MOVPE), and related techniques. These advantages include the ability to control growth reproducibly to atomic monolayer dimensions and to monitor the growth process in real-time. With the advantage of an ultra-high vacuum growth environment of MBE, it is possible to study the dynamics of the growth process itself using modulated molecular beam techniques and RHEED (reflection high energy electron diffraction).

According to the Collins Dictionary, epitaxy means the growth of a thin layer on the surface of a crystal so that the layer has the same structure as the underlying crystal. As expressed above, there are several categories of epitaxy which differs by different parameters including the roughness or the growth rate. Molecular Beam Epitaxy (MBE) has the lowest growth rate which allows precise control of the sample morphology [10]. The MBE technique is used when the degree of lattice mismatch between two layers is significant or when we have a low tolerance for different layer thickness. The low substrate temperature as well as the slow growth rate, typically less than one monolayer per second reduces the probability of defects formation. In short, if one is designing a really precise thin-film device for computing, optics, or photonics then MBE is one of the techniques to choose.

In order to make a new crystal using MBE, we have to start with a base material called a substrate . Materials often used as a substrate are silicon, germanium, or gallium arsenide [35]. Typically, the first step involves heating your substrate to hundreds of degrees (for instance 500–600°C or about 900–1100°F [35]). This is followed by firing

relatively precise beams of atoms or molecules, heated up in their gas forms, at the substrate from "guns" called effusion cells. We need one "gun" for each different beam, shooting a different kind of molecule at the substrate, depending on the nature of the crystal we are growing.

The molecules land on the surface of the substrate, condense, and build up very slowly and systematically in ultra-thin layers, so the crystal is grown one atomic layer at a time. This is the reason why MBE is an example of what is called thin-film deposition. However, in order to create a crystal precisely, one cannot use atmospheric conditions. Indeed at atmospheric pressure, the air density is high enough that if one shoot molecules in the direction of the substrate they will scatter in the air and would never reach the surface of the substrate. In short, the longest mean free paths are desirable for the material beams we are evaporating on the substrate. Consequently, one need to change the vacuum conditions to address this issue. The vacuum is obtained by a combination of pumps. First, a rough vacuum with a mechanical pump is established. Then a high vaccum environment is reached using a turbo molecular pump and finally a very high vacuum environment is created with a cryo-pump and a sputter ion pump. The level of vacuum is measured by an ion gauge inside the vacuum chamber of the MBE. One reason that MBE is such a precise way of making a crystal is that it happens in highly controlled conditions: extreme cleanliness and what is called an ultra-high vacuum (UHV), so no dirt particles or unwanted gas molecules can interfere with or contaminate the crystal growth.

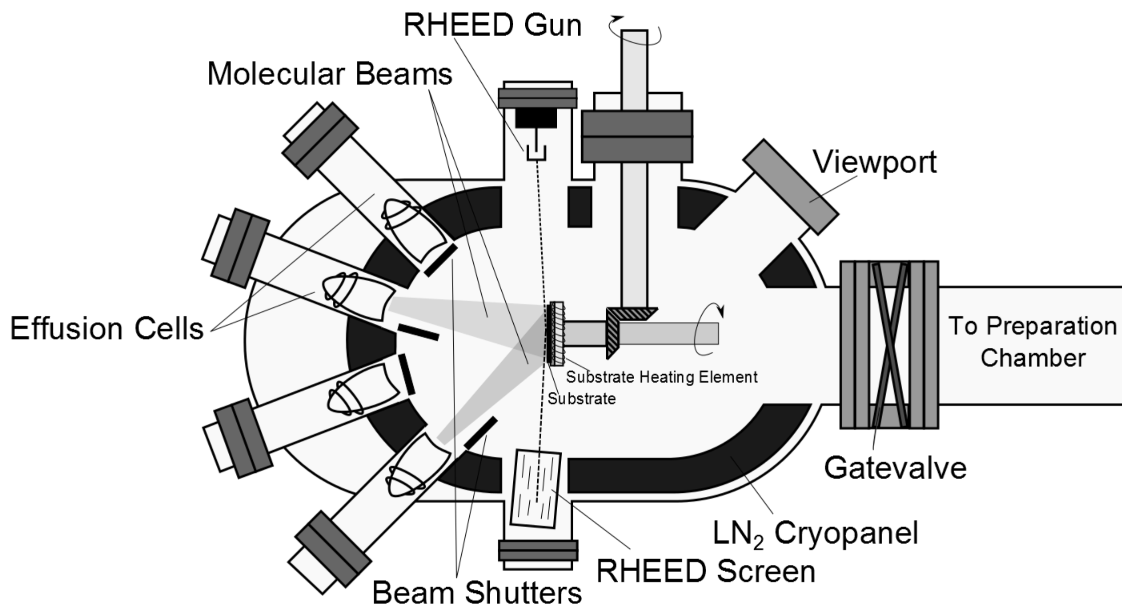

Figure 1: Diagram of Molecular Beam Epitaxy growth chamber [32].

Figure 1 depicts the diagram of the MBE growth chamber. It is possible to block the flux of each beam using beam shutters as we can see in the figure above (fig.1). The

growth rate is directly linked to the flux of this beam and it is desirable to have the flux as steady as possible. The effusion cell heating is monitored by a thermocouple and a closed-loop control system is implemented to help stabilize the flux. When it has reached the desired condition, the shutter placed in front of the effusion cell is opened which allows the beam to impinge on the substrate wafer. The atoms will find preferred sites on the surface of the wafer and this is how the structure grows. As it is an on-off system at a very slow growth rate, it allows precise control over the composition of the structure.

1.2 Differential Interference Contrast (DIC) Microscope

1.2.1 Background and History of DIC

In this subsection, a DIC microscope and the fundamental concepts of this type of microscopy are introduced.

The basic differential interference contrast (DIC) system was invented by Francis Smith in 1955. The DIC microscope is a modified polarized light microscope with two Wollaston prisms added, one to the front focal plane of the condenser and a second at the rear focal plane of the objective. Several years later, Georges Nomarski, a Polish-born French physicist, modified the standard Wollaston prism configuration to enable these exceedingly thin optical components to be physically located away from the aperture conjugate planes.[24]

The optical components of a DIC microscope do not mask the objective and thus does not restrict the numerical aperture. Thanks to this process, much higher resolution can be maintained including imaging on relatively thick specimens like the semiconductors present in this dissertation.

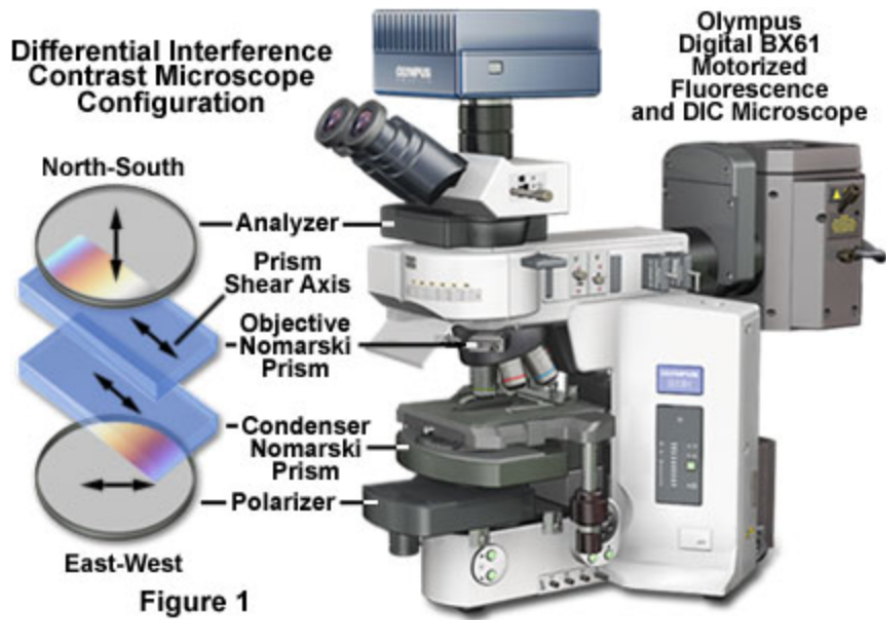

Figure 2: Diagram of a DIC microscope [24].

Figure 2 shows a typical differential interference contrast configuration for a modern transmitted light microscope also equipped for fluorescence illumination. A polarizer and analyzer are inserted into the optical pathway before the condenser and after the objective, respectively. Several beam splitting (modified Wollaston or Nomarski) prisms designed to accommodate objectives having different focal lengths and aperture sizes are installed in the condenser turret assembly, while a single Nomarski prism (compatible with all objective specifications) resides in a slider frame positioned in the nosepiece.

Images obtained in differential interference contrast microscopy have a distinctive shadow-cast appearance as if they were illuminated from a highly oblique light source originating from a single azimuth. This effect renders specimens in a pseudo-three-dimensional relief and is an indicator of actual topographical structure. This effect gives a rough idea about the surface conditions of a semiconductor. However, DIC is a qualitative rather than a quantitative technique.

Because the sampling and reference beams both traverse a similar region of the specimen which is confined to a spatial separation of fewer than two micrometers, DIC will not yield accurate measurements of specimen refractive index or thickness.

The wave pairs employed in differential interference contrast are generated by the action of a birefringent beam splitter (either a Wollaston or Nomarski compound prism) on a plane-polarized wavefront of coherent light originating from a tungsten filament and focused into the front focal plane of the microscope condenser (where the beam splitter is positioned).

After wavefronts generated by the beam splitting prism pass through a specimen phase gradient, they are recombined through differential interference by a second prism and an analyzer (another polarizer) to yield a high-contrast rendition of the gradient. In distinction, however, the DIC image corresponds to the mathematical first derivative, rather than the magnitude, of the gradient profile obtained from the specimen optical path difference.

In general, only four basic components are required to configure a research or standard laboratory bright field microscope for observation in differential interference contrast:

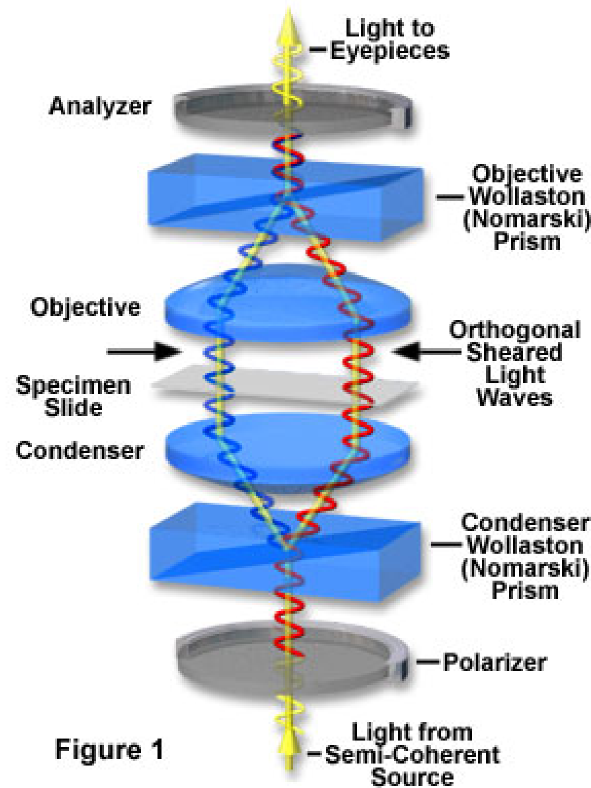

Figure 3: Differential Interference Contrast Schematic [24].

- **1) The Linear Polarizer:** Inserted into the optical pathway between the microscope light port, this component is designed to produce the necessary plane-polarized light for interference imaging.
- **2) Condenser Wollaston or Nomarski Prism:** In order to separate the polarized light emanating from the polarizer into two components, a specialized beam-splitting prism is placed in or near the conjugate focal plane of the condenser iris diaphragm aperture as illustrated in the figure above. This results in the splitting of the incident wavefronts of plane-polarized light into mutually orthogonal polarized components thanks to the Wollaston or Nomarski prism.

- **3) Objective Nomarski Prism:** Positioned behind the objective a second beam splitting prism is employed to recombine the sheared wavefronts in the conjugate plane of the objective rear aperture. This component, which is an element critical to interference and image formation, is also termed the objective prism.

- **4) Analyzer:** A second linear polarizer is installed behind the objective prism. Termed an analyzer, this polarizing element is positioned in the optical pathway before the tube lens. Components of circular and elliptically polarized light arriving from the objective prism pass through the analyzer and subsequently undergo interference to generate the DIC image at the microscope intermediate image plane (eyepiece fixed diaphragm or camera system projection lens aperture).

1.2.2 Summary

Differential interference contrast microscopy is basically a beam-shearing interference system in which the reference beam is sheared by a minuscule amount, generally somewhat less than the diameter of an Airy disk. In fact, each point in the specimen is represented by two overlapping Airy disks in the final image, one being brighter and the other darker than the background.

The condenser prism converts each wavefront illuminating the specimen into two slightly displaced, parallel beams that are orthogonally polarized relative to each other, while the objective prism serves to recombine the beams. The combination of these two prisms, which are mirrored onto one another by the optical system, is a key feature in the ability of differential interference contrast to form sharp images with a numerical aperture.

The resulting DIC images possess a shadow-cast appearance that effectively displays the gradient of optical paths for both low and high spatial frequencies. Those specimen regions where optical paths increase along a reference direction appear brighter (or darker), while the regions where path differences decrease appear in reverse contrast. Steeper gradients in optical path difference result in greater contrast. A wide variety of specimens are good candidates for imaging with differential interference contrast, including very thin filaments or sharp interfaces, which produce good contrast even when their diameter falls below the resolution limit of the optical system.

1.3 Atomic Force Microscopy

1.3.1 AFM History and Background

Atomic force microscopy (AFM) was developed when people tried to extend the scanning tunneling microscopy technique (STM) to investigate electrically non-conductive materials, like proteins[33] [2]. In 1986, Binnig and Quate demonstrated for the first time the

ideas of AFM, which used an ultra-small probe tip at the end of a cantilever [9]. AFM is a scanning probe microscope in which a topographical image of the sample surface can be achieved based on the interactions between a tip and a sample surface.

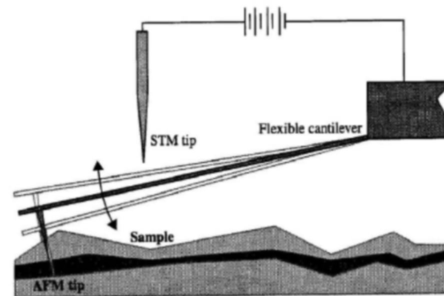

Figure 4: First model of AFM using a scanning transmission microscope tip [14].

1.3.2 Principle of AFM

A typical AFM consists of a cantilever with a small tip (probe) at the free end, a laser, a 4-quadrant photodiode, and a piezo scanner as seen in figure 5.

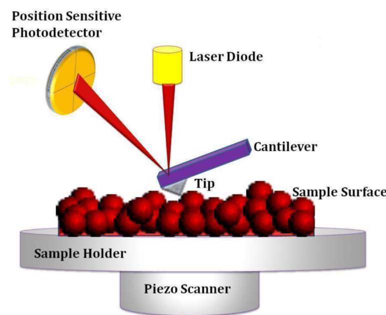

Figure 5: AFM principle [20].

As shown in figure 5, the AFM brings a probe in close proximity to the surface.

- The force is detected by the deflection of a spring, usually a cantilever (diving board).
- Forces between the probe tip and the sample are sensed to control the distance between the tip and the sample.
- The laser is focused to reflect off the cantilever and onto the sensor.

- The cantilever is designed with a very low spring constant (easy to bend) so it is very sensitive to force as we can see in the picture below.

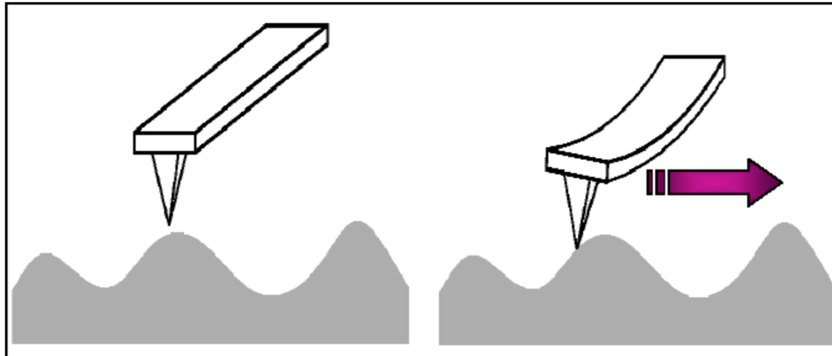

Figure 6: AFM binding effect occuring on the tip when it gets closer to the surface.

When the tip, which is attached to the free end of the cantilever, comes very close to the surface, attractive and repulsive forces due to the interactions between the tip and the sample surface cause a negative or positive bending of the cantilever. This bending is detected by the help of a laser beam. The cantilever can be thought of like a spring. The quantity of the generated force between the tip and the surface depends on the spring constant (stiffness) of the cantilever and the distance between the tip and the surface. This force can be characterized by Hooke's Law.

$$\vec{F} = kx \tag{1}$$

where F is the resulting force, k is the spring constant and x is the cantilever deflection.

If the spring constant of the cantilever is less than that of the surface, bending occurs in the cantilever and this deflection is monitored. As the tip travels across the sample, it moves up and down according to the surface properties of the sample (e.g. topography). These fluctuations are sensed by the interactions (electrostatic, magnetic, capillary, van der Waals) between the tip and the sample. The displacement of the tip is measured and a topographical image is obtained.

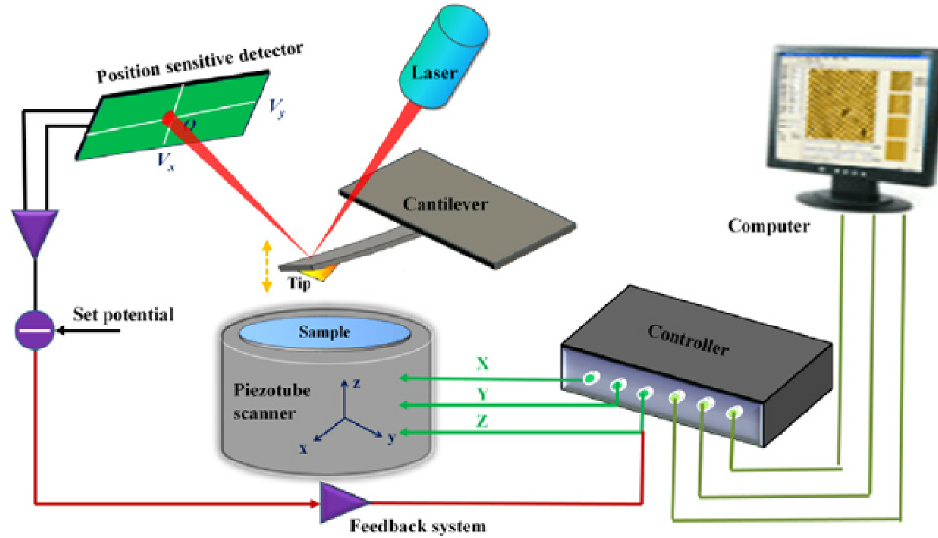

Figure 7: Process to obtain an image.

1.3.3 Different Modes of Operation

There are three modes of force on the tip used to acquire images :

AFM Modes of Operation	Working Principles	Relative Forces
Contact Mode	Physical contact (Tip/Surface)	Repulsive Force
Non-contact Mode	No contact (Tip/Surface)	Attractive Force
Tapping Mode	Intermittent/Short Contact (Tip/Surface)	Repulsive/ Attractive

Table 1: Different AFM modes.

AFM Modes of Operation	Advantages	Disadvantages
Contact Mode	High scan speed, high resolution	Damaging the surface
Non-contact Mode	Low resolution/no damage	Slow scan speed, time consuming
Tapping Mode	High resolution/minimal damage	Slow scan speed

Table 2: Advantages and disadvantages of AFM modes.

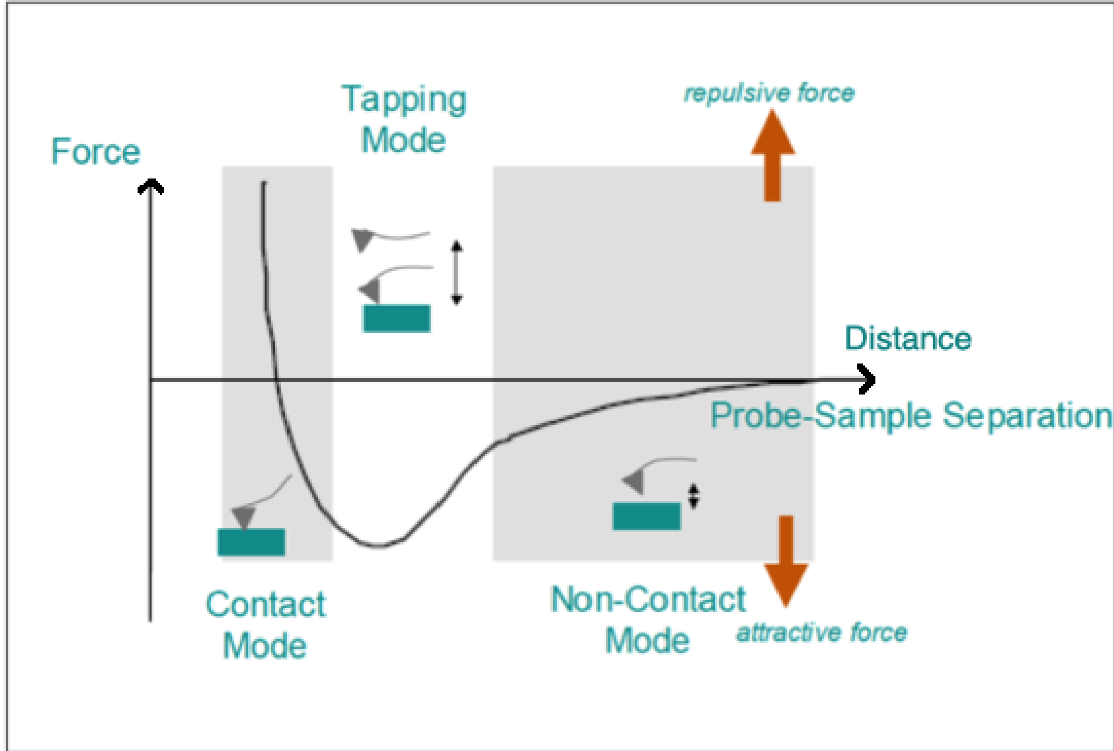

Figure 8: Schematic of the different AFM mode of imaging.

For the research presented here, all samples were imaged using non-contact mode. This study focuses on defects that could occur during the growth process of the semiconductors and the objective was to avoid artifacts due to contact of the tip with the sample.

When the tip approaches the surface of the sample, van der Waals forces cause attraction. In the non-contact region, the distance between the probe and the surface is around tens to hundreds of angstroms. In contact region, total van der Waals forces are positive (repulsive force) because the overlapping of the electron shells (Pauli Principle).

1.3.4 IV. MFP-3D AFM

In this subsection, the process and the main part of the AFM used to measure the topography (height, depth, shape) of the defects present on the surface of each sample will be presented. The model of AFM that was used for this research is the MFP-3D manufactured by Asylum Research.

The major parts of the MFP-3D AFM are:

- **The isolation chamber :** The isolation chamber is a heavy steel chamber with special acoustic damping materials and vibration isolation pads under the legs.

This part has a crucial role in high-resolution AFM images which involve isolating the AFM from lab noise and vibrations.

- **The AFM head :** The AFM head moves the cantilever vertically as the sample moves laterally beneath it. It also contains optics for illuminating and optically imaging the sample and cantilever from above.
- **The Scanner :** The AFM component holds the sample and scans it laterally in X and Y directions beneath the tip.
- **The Base :** A metal plate on which the head and the scanner sit. It contains an optical microscope with CCD cameras and sample illumination controls for optically viewing the sample and cantilever.

In order to get an image with the MFP-3D AFM, one needs to use the software called Igor Pro. This software was developed by WaveMetrics which is a stand-alone program that has extensive scientific graphing and image processing capabilities.

Major parameters such as the setpoint voltage, the integral gain and the scanning speed are important to maintain good tracking and feedback to produce high quality images.

1.3.5 Imaging Modes of the MFP-3D

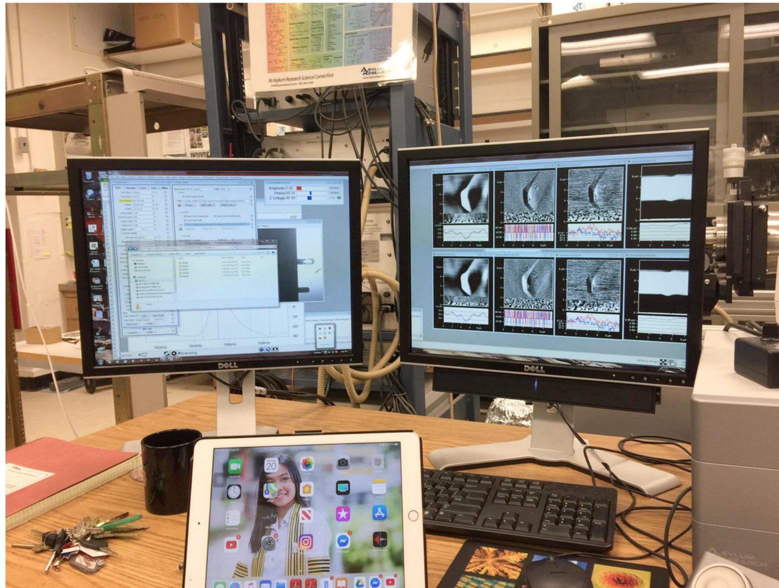

Figure 9: Setup of the MFP-3D.

Figure 9 presents the software interface of Igor Pro, explained in the previous section. If all channels are selected, eight different images can be obtained as seen on the right screen. Within those images, there are two different groups: the images that were collected in the forward scan direction called trace and those collected in the reverse scan direction called retrace. Collecting these two types of images is useful to check the cantilever probe geometry. If a large difference between the two images is observed, it may indicate a problem with the cantilever which could then be addressed.

With this AFM four different images can be obtained: Height, amplitude, phase, and the Z sensor. Only the physical meaning of the height and the amplitude images are explained here since the two others were not relevant in our studies.[8]

- **The height :** In order to know the topography of an image, the focus should be on the channel called height. This is the type of image most commonly published. The height is an image from the corrected Z-piezo voltage (tip height found by feedback loop) and gives true surface height data. Usually, the data are presented as a map of differently colored pixels, with a color bar relating the color to height.This is very useful, as, on such an image, it's possible to see both lateral (XY) and height(z) measurements. In the Z direction, very accurate measurements can be made. However, one reason other types of images are commonly shown is that such "height maps" do not really "look like" the object in question. In other words, the appearance of a certain shape is very different than in optical (or electron) microscopy.What this means, is that to the casual observer such images do not display easily the shape of the features. Ways around this include shading the image, and more commonly, creating a pseudo-3D image from the height data. However, an alternative is to show the deflection (or amplitude) image.
- **The Amplitude:** Because the amplitude image is equivalent to a map of the slope of the sample, this channel often displays the shape of the features more easily. However, it should be noted that the Z-scale in deflection or amplitude is completely meaningless in terms of the sample structure. In the Non-Contact Mode, the AFM tries to keep the amplitude constant. An amplitude image shows how the tip is deflected as it encounter the sample surface. Images are similar to the topography showing the map of the slope of the sample, but the Z scale is not linear. In other words, the amplitude image is the image of an error signal of amplitude. The scale does not reflect the real height of the features.

1.4 Scanning Electron Microscopy

The SEM used for this research is the ZEISS Neon 40 ESB which is a Field Emission SEM using a very sharp tungsten wire filament. The microscope is a dual beam Focused Ion Beam (FIB)/SEM which allows etching of the surface as we are imaging it. It is

composed of a 0.1-30kV Schottky emitter (SEM) and a 2-30 kV Ga liquid metal ion source (FIB). The magnification is 20x to 900,000x [18]. One particularly important parameter when dealing with EM microscopes or every microscope, in general, is the resolution. The smallest or best resolution that a microscope can provide allows one to see features that cannot be observed by the naked eye.

The resolution is defined as the smallest separation at which two point objects can be seen as distinct. In a regular light microscope, like the Differential Interference Contrast microscope seen before, the resolution is limited by the wavelength 200 nm.[11] Abbe's equation defines the diffraction-limited resolution which is :

$$D_o = \frac{0.612\lambda}{nsin\alpha} \tag{2}$$

where α is the half aperture angle, n sin α is considered as the numerical aperture, λ is the wavelength of the incoming light source and D_o is the ultimate resolution. Therefore small numbers of D_o mean higher resolutions. However, this definition of Abbe's equation is defined for the light microscope. Using an electron microscope one can push this limit using electrons due to the fact that electrons have a much smaller velocity-dependent wavelength and then can provide a much higher resolution.By using this principle one can obtain another definition of D_o which is :

$$D_o = \frac{0.753}{\alpha\sqrt{V}} \tag{3}$$

where V is the accelerating voltage and D_o is in nm.
An electron microscope is composed of these major parts :

- Vacuum pumps
- Electron source
- Electromagnetic lenses/ coils
- Electron detectors

The mean free path, which is the distance a particle takes before colliding with another one, needs to be maximized. By getting rid of the air present in the chamber we can meet this goal. Depending on the type of microscope we are using we will need different vacuum regimes. In our case for the ZEISS Neon 40 EsB because it is a field emission scope we need to reach a vacuum regime called Ultra High Vacuum regime (10^{-10} Torr) in the gun or source chamber. The advantage of using a field emission

scope is to have a more coherent beam and a better resolution which is crucial for seeing tiny defects on the surface of semiconductors.The imaging principle used on a Scanning Electron Microscope is described in figure 10.

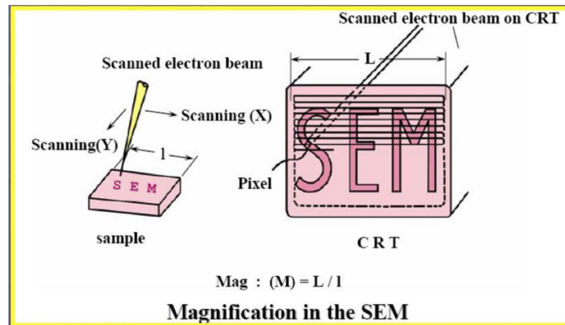

Figure 10: SEM imaging principle [18].

An image is formed using this process: a convergent beam of electrons probe different locations across the surface of the sample which results in a signal at each point detected by various detectors. The magnification is set by the scanned area on the surface of the sample. Therefore a wider area scanned corresponds to a lower magnification whereas a smaller area scanned corresponds to a higher magnification.

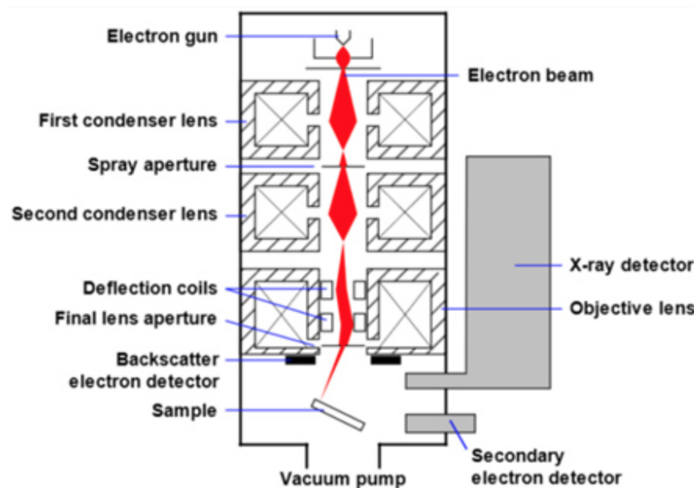

Figure 11: SEM column overview [13].

Figure 11 presents the general schematic of an SEM column. The SEM imaging technique is a nondirect imaging technique and require appropriate detectors for each signal produced from the beam-specimen interaction. These signals are collected and form different SEM images depending on the type of signal collected. A relevant parameter to determine is how far inside the sample we can collect information. In other words how

deep does the electron beam go through the sample while producing scattered electrons that still have enough energy to escape and be detected by the detectors.

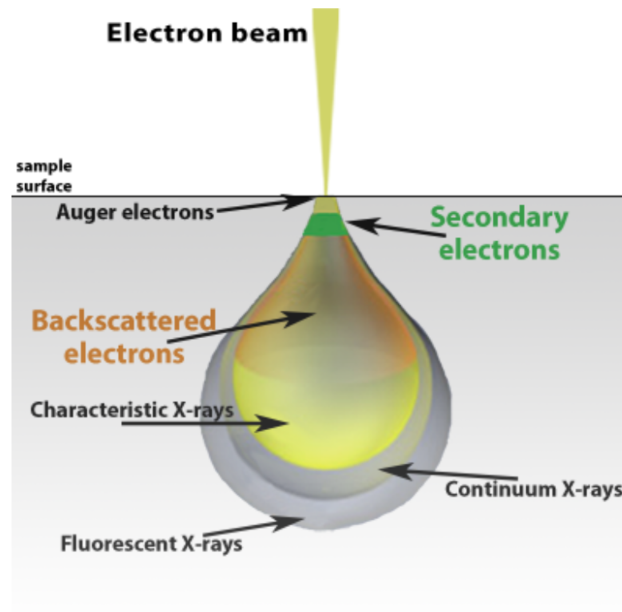

Figure 12: Interaction volume representation [13].

As seen in figure 12, the interaction volume is the region over which the beam electrons interact with the specimen and then generate an image[11]. The size of the interaction volume depends on the beam properties, such as the accelerating voltage and the specimen properties. Indeed when the electron beam hits the surface of the sample, it penetrates the sample to a depth of a few microns.[13] As the electrons interact with the sample, they produce secondary electrons, backscattered electrons, and characteristic X-rays (fig.12). These signals are collected by one or more detectors to form images which are then displayed on the computer screen. The detectors that collect the useful signals resulting from the beam specimen interaction are positioned in the chamber to maximize different but useful sample data.

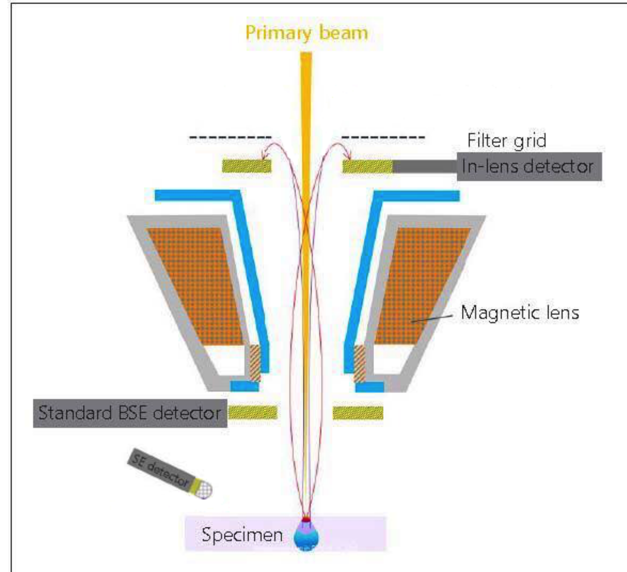

Figure 13: Close up of objective lens region on SEM with the representation of the different detectors used in the normal imaging mode [34].

Figure 13 shows the three main detectors used for imaging the semiconductors in this thesis. The first detector is the backscattered electron detector. This detector gives atomic number contrast, topographical contrast and crystalline contrast information. This detector is the most appropriate one to see defects on the surface of a semiconductor. Unfortunately, the backscattered detector had an issue during the year this research was conducted. However the EBSD camera provides an equivalent backscattered detector as the one presented before. The only difference with this detector is that we need to use the EBSD sample holder where the sample is tilted by 70° with respect to the incoming electron beam. This detector is called a forescattered backscattered detector.

The closest detector to the specimen surface labeled SE detector on the diagram above, is called an Everhart-Thornley detector. It detects mostly secondary electrons (90 %) but it also detects a small fraction of backscattered electrons around 10%. In comparison, the inlens detector collects only secondary electrons for producing a true secondary image. Consequently, the Everhart-Thornley detector will give us more information about the topography of the surface of the sample.

1.5 EBSD

In order to have more information about the topography of the surface of the semiconductors, it is important to try to determine the crystalline orientation of the defects present on its surface. Accordingly using a technique related to SEM called Electron Backscattered Detector (EBSD) is a judicious choice. First, a brief overview of EBSD is presented and then the advantages of this technique are described.

In order to explain the principle of EBSD, we use three sources offered by Oxford Instrument. [29] [16] [15], the manufacturers of the EBSD equipment used here.

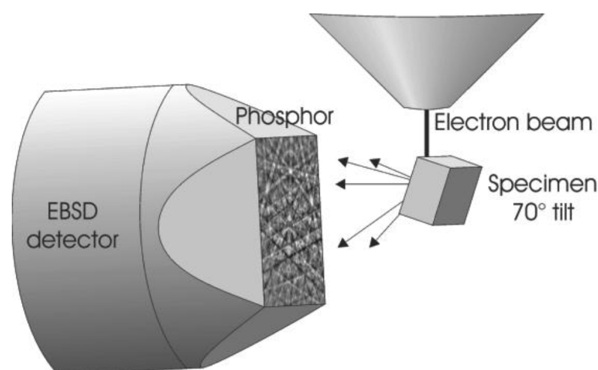

Figure 14: Simulation of electron backscattered diffraction patterns [1].

EBSD is a scanning electron microscope based technique that gives crystallographic information about the microstructure of a sample. In EBSD, a stationary electron beam interacts with a tilted crystalline sample (tilted at 70°) and the diffracted electrons form a pattern that can be detected with a fluorescent screen called the EBSD detector as seen in figure 14. The diffraction pattern is characteristic of the crystal structure and orientation in the sample region where it was generated. Hence the diffraction pattern can be used to determine the crystal orientation and provide more information about the topography of the surface of the semiconductor in our study.

The exact process of EBSD is quite simple, In order to get information about the crystal orientation we need to acquire data from several points on the sample. Indeed the electron beam probes a certain number of points defining the scanning area. When every point is probed, the resulting map reveals the grain morphology, orientations and boundaries. The diffraction patterns obtained at each point can lead to further analysis and information such as the preferred crystal orientation (i.e. texture) within the sample. Thus a complete and quantitative representation of the microstructure can be established with EBSD. Each point is made from the same material but the grains/crystals can be oriented in different ways. Then each point results in a different backscatter pattern. Finally after all the data is analyzed by the software, the crystal orientation of the defects present on the surface of the sample could be determined.

In order to understand the principle of Electron Backscattered Diffraction we need to explain the term of diffraction.

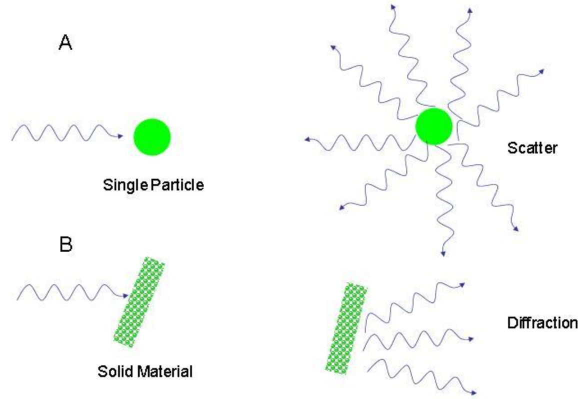

Figure 15: Diffraction case.

In the figure above (fig.15), we have two general cases for diffraction. In case A, when electrons interact with a single particle, the incident beam is scattered uniformly in all directions. In case B, when electrons interact with a solid material the scattered beams can add together in a few directions and reinforce each other to yield diffraction. The regularity of the material is responsible for the diffraction of the beams. In this study we are operating in case B. The diffraction pattern related to this case is a cloud diffraction pattern. This is due to the phenomena of interference. Interference occurs among the waves scattered by the atoms when crystalline solids are exposed to X-rays or electrons. There are two types of interference depending on how the waves overlap one another. Constructive interference occurs when the waves are moving in phase with each other. Destructive interference occurs when the waves are out of phase.

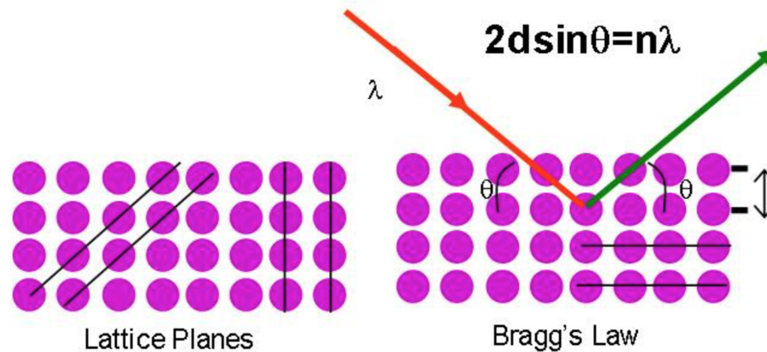

Figure 16: Bragg's Law diffraction schematic.

As seen in figure 16 Bragg's Law describes the condition to have constructive interference.

The relationship describing the angle at which a beam of X-rays or electrons of a particular wavelength diffracts from a crystalline surface was discovered by Sir William H. Bragg and Sir W. Lawrence Bragg and is known as Bragg's Law

$$2dsin\theta = n\lambda \quad (4)$$

where λ which is the wavelength of the x-ray or electrons, θ is the scattering angle, n is the integer representing the order of the diffraction peak and d is the inter-plane distance of (i.e atoms, ions, molecules).

Bragg's law can give information about the inter-plane distance. In addition, Energy Dispersive Spectroscopy can determine the concentration of different elements around the defects that we are interested in. However, as we noted in figure 12, X-rays could be formed microns away from the electron beam sources therefore if the defects are less than a micron it makes it difficult to have a reliable idea of the actual composition of the defects or around them because the defect in itself is too small.

EBSD like the X-ray diffraction technique is able to analyze the sample texture however EBSD is complementary to the standard method of measuring texture using X-ray diffraction. This is due to the fact that EBSD goes further because it can relate the texture present to the microstructure of the material. In addition, textures which vary from place to place in a sample can be studied easily. Accordingly, we get further crucial information using EBSD that is not possible to obtain using Xray diffraction.

2 B series InSb Quantum Well

In this part, we will study two devices involving InSb quantum well heterostructures with the same epilayer compositions but grown at different times.

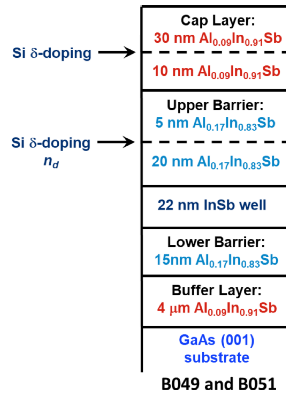

Figure 17: Epilayer composition of B051 and B049.

As seen in figure 17, B049 and B051 wafers are heterostructures composed of different layers with different material composition, grown on a substrate with a much different lattice constant. The first sample, labeled B049, is a wafer of 1 micron of InSb/AlInSb epilayers on a GaAs substrate oriented in the [001] direction. The second one, labeled B051, is similar to B049 but after device processing. This device is a prototype of a Hall Effect sensor array. By comparing these two similar samples, the effects of device processing on the surface of the semiconductor will be studied. The term of heterojunctions devices or heterostructures need to be explained first in order to understand how it differs from the general term of a semiconductor.

Figure 18 is an example of heterostructure from Solid State Electronic Devices, 6th Edition (2005), written by Ben G. Streetman and Sanjay Kumar Banerjee: [4]

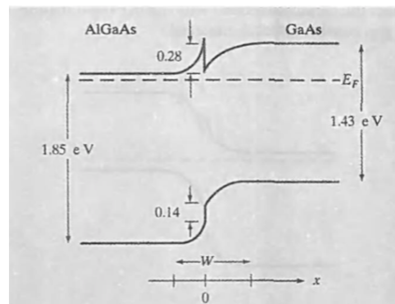

Figure 18: Example of a heterojunction in which heavily n-type AlGaAs is grown on lightly doped GaAs [4].

A heterostructure device consists of a material involving heterojunctions, which are junctions between two semiconductors with different bandgaps as can be seen in figure

18. Indeed on the band diagram, one can notice that the energy gap on the GaAs side is smaller than the energy gap on the AlGaAs side. The availability of heterojunctions and multilayer structures in compound semiconductors opens a broad range of applications for device development such as field effect transistors, semiconductor lasers or, like in our case for B051, Hall effect sensors.

The aim of this study is to maximize the electron mobility by reducing the density of defects in the semiconductors. This is the case for the Hall Effect sensor, in which a higher μ_e decreases the current produced $\overrightarrow{I}$ for a given applied voltage. In other words, the higher the electron mobility, the more sensitive the sensor will be. The sensor array is composed of 9 sensors cells, each with the geometry shown in the optical microscope image below (fig. 19).

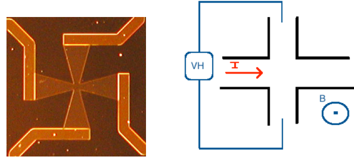

Figure 19: Example of a heterojunction in which heavily n-type AlInSb is grown on undoped InSb.

$$V_H = \frac{\overrightarrow{I} \times \overrightarrow{B}}{en} \tag{5}$$

Now that a brief explanation of the two samples was made one needs to understand what is at stake when one is growing epilayers on a substrate. A previous description of the principles of Molecular Beam Epitaxy (MBE) used to grow the layers on the surface of the substrate was made in the background section. However, further precautions to reduce the types of defects encountered in this study need to be made.

The technique used to grow every sample studied in this dissertation is a technique called epitaxial growth or epitaxy. It allows growth of an oriented single crystal layer on a substrate wafer. One requirement to obtain high crystallinity is the principle of Lattice-Matching. When one is growing some epitaxial layers composed with the same material that was used for the substrate, similar to what will be discussed in the second part of this thesis concerning a growth of a thin layer of GaSb on a GaSb substrate, there is a natural matching of the crystal lattice and consequently we obtain a high-quality single-crystal layers result.

However, in fact, it is most likely to choose epitaxial layers with lattice constants that differ from the substrate, which is the case of the first and last section of this thesis.

The epitaxial layers obtained are strained, partially strained or relaxed, which will be explained below. All of materials presented in this thesis have a zinc blende structure, which is a face-centetered cubic lattice with a two-atom basis.

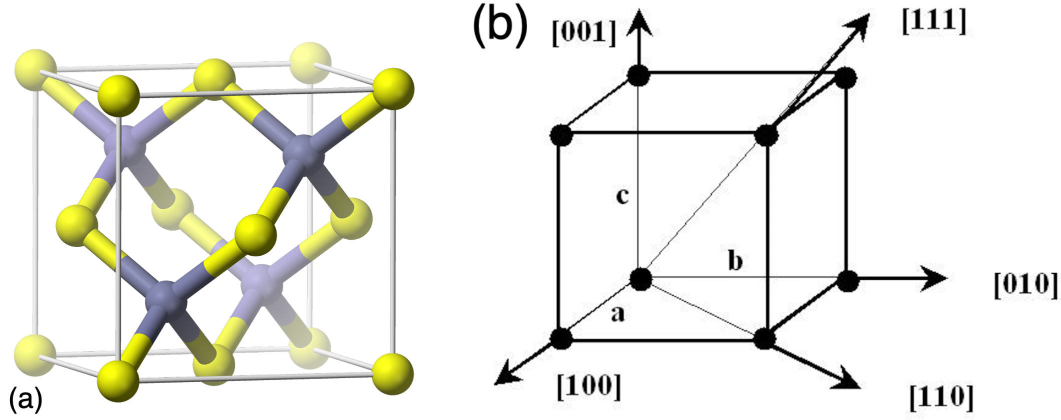

Figure 20: Figure (a) :Zinc Blende structure schematic [5] , Figure (b) : Crystallographic notation schematic [21].

As shown in figure 20, the basis atoms are one Group-III atom and one Group-V atom. The lattice constant,a_o, is the length of the cubic unit cell and the basis atoms are $\frac{a}{4}(\hat{x}+\hat{y}+\hat{z})$ apart. The epilayers are oriented with the Z-direction normal to the surface. In figure (b), a schematic of the different orientations is presented. The three integers h,k and l are called the Miller indices; these three numbers define a set of parallel planes in a lattice. One advantage of taking the reciprocals of the intercepts is avoidance of inifinities in the notation. [4] The a, b and c notation is simialar to the x,y and x one used in the EBSD analysis below. (100) is the plane perpendicular with the a vector in figure (b), (010) is the plane perpendicular with the b vector and (001) is the plane perpendicular with the c vector.

The distance d between two adjacent planes labeled (hkl) is equal to :

$$d = \frac{a_o}{(h^2 + k^2 + l^2)^{1/2}} \tag{6}$$

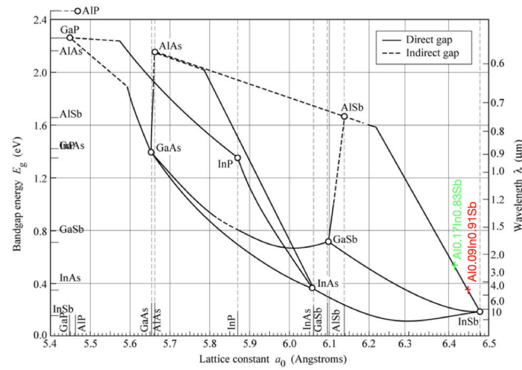

Figure 21: Bandgap as a function of lattice constant for non-nitride III–V compound semiconductors (points) and their random ternary alloys (lines) at zero temperature.

In figure 21, a graph of the bandgap energy vs the lattice constant of various III-V semiconductors is depicted. The points on the graph corresponds to the different binary compounds and the lines that link one to another depicts alloy of both compounds. By varying the concentration of an alloy, one can engineer a bandgap suitable for a given application. Knowing that AlSb has a lattice constant of 6.1355 A and InSb has a lattice constant of 6.4794 A one can determine by a simple calculation the lattice constant of an epilayer. In our study (fig.17),the material is composed of $Al_{0.09}In_{0.91}Sb$,with a lattice constant of 6.4485 A, and $Al_{0.17}In_{0.83}Sb$ with a lattice constant of 6.4201 A. The different epilayer compositions studied in this section are highlighted in red and green in figure 21. As seen a small variation of the concentration of one alloy in comparison to another has a huge effect on the lattice constant of the semiconductor. Therefore one has to be careful and cannot grow every alloys with different concentrations if a material with interesting properties is the aim.

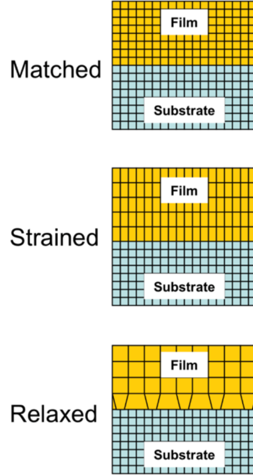

Figure 22: Lattice Matching process.

The strain due to lattice mismatch between the film and the substrate, calculated with respect to the strained lattice is defined as : [28]

$$\epsilon_m = \frac{a_f - as}{a_f} \tag{7}$$

where ϵ_m is the strain imposed and a_f is the corresponding lattice spacing of a free-standing film.

For a small lattice mismatch, a thin film material will strain to the lattice structure of the substrate, creating a pseudomorphic structure. However, strain accommodation is not possible if the film is too thick.In that case, dislocation defects are created at the interface, leading to a relaxed epilayer as the film returns to its original lattice structure above the interface, as illustrated in the schematic above (fig.22). A study of misfit dislocations and surface morphology of lattice-mismatched GaAs/InGaAs heterostructures [23] exhibits the distribution of lines due to misfit dislocations in a form of a well-defined cross-hatch pattern. Consequently, we should be careful to not exceed a critical thickness which depends on the lattice mismatch which could lead to line defects due to misfit dislocations if this requirement is not satisfied.The critical layer thickness computation requires mechanical equilibrium.[30] [27] The total strain energy per unit area ϵ_T should be a minimum with respect to the in-plane strain e :

$$\frac{\partial \epsilon_T}{\partial |e|} = 0 \tag{8}$$

evaluated at $|e| = f$, where f is the mismatch between the film and the substrate. In this case ϵ_T is defined as a sum

$$\epsilon_T = \epsilon_H + \epsilon_D \tag{9}$$

of the homogeneous strain energy density ϵ_H:

$$\epsilon_H = 2G\Big(\frac{1+\nu}{1-\nu}\Big)e^2 h \tag{10}$$

and the areal energy density of the dislocation ϵ_D:

$$\epsilon_D \equiv \frac{E_l}{p} \tag{11}$$

where E_l is the energy per unit length of a given dislocation line, p is the spacing between the dislocations in the assumed rectangular array and G is the shear modulus.

The spacing between dislocations is given by :

$$p = \frac{b}{f - |e|} \tag{12}$$

where b is the magnitude of Burger's vector. By combining the equation of ϵ_H (eq.9) and the spacing between the dislocations (eq.10) respecting the mechanical equilibrium condition (eq.7) one can obtain an equation for the critical thickness h_c:

$$h_c = \frac{b}{4\pi f(1+\nu)}\Big[\ln\Big(\frac{h_c}{b}\Big) + 1\Big]. \tag{13}$$

where b is the magnitude of the Burger's vector and ν the Poisson ratio, proper to each material studied.

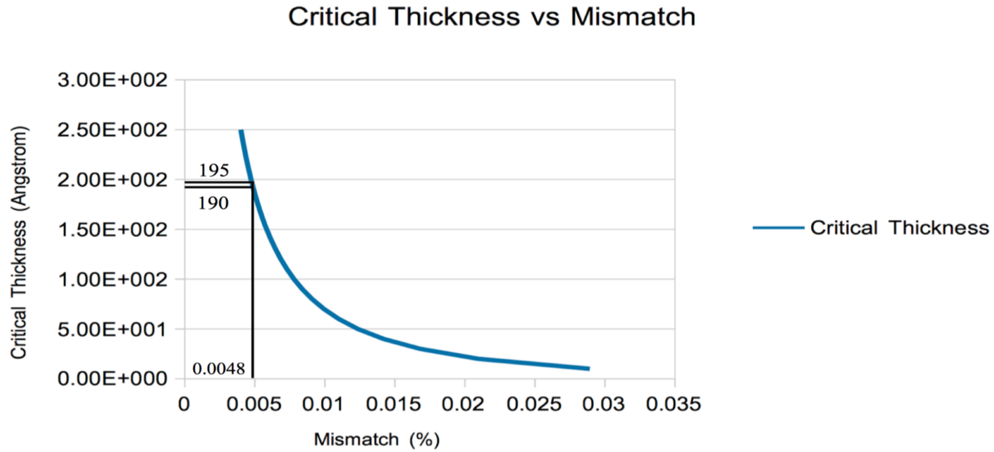

Figure 23: Critical thickness vs mismatch calculated in the case of B049 and B051.

As shown in figure 23, the calculated critical thickness versus Mismatch is depicted. In this study, the buffer layer is fully relaxed. For the lower barrier and the upper barrier with a composition of AlSb 17% and InSb 83%, the mismatch calculated is -0.0043 % and the critical thickness is 195 Å for growth on the relaxed buffer layer. For the InSb quantum well layer, the mismatch is 0.0048 % and the critical thickness is 190 Å for growth on the relaxed buffer layer. Comparing those values with the intended composition that was seen in the introduction, one can see that the critical thickness for the barrier layers is almost exceeded. Now that the principle of lattice matching was explained, the two samples will be studied looking for the presence of line defects due to misfit dislocations on their surfaces.

2.1 B049

Figure 24 shows an AFM image 7 um wide by 7 um long depicting the overall surface condition.

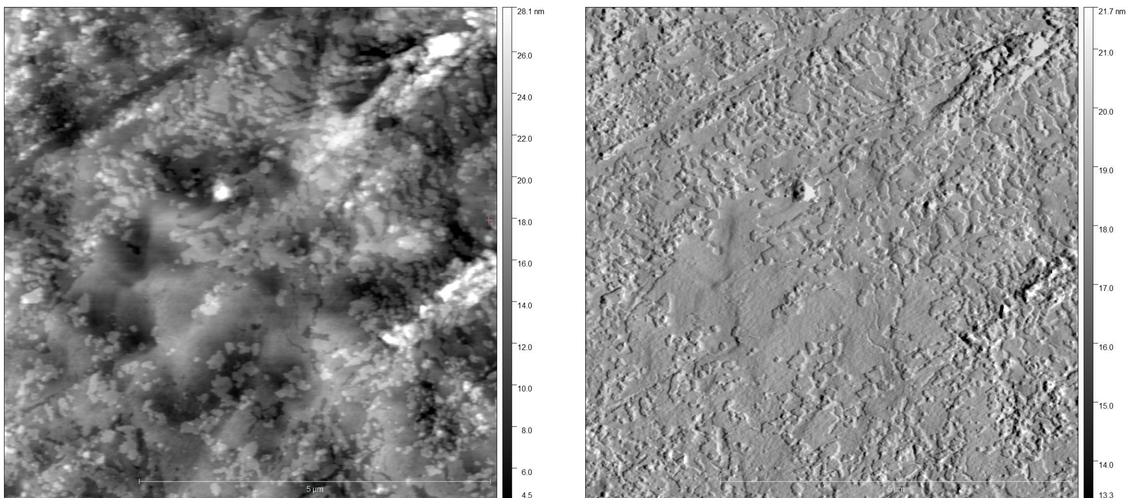

Figure 24: B049 background taken with the AFM.

As seen in figure 24, the surface is rough with several topographical variations.

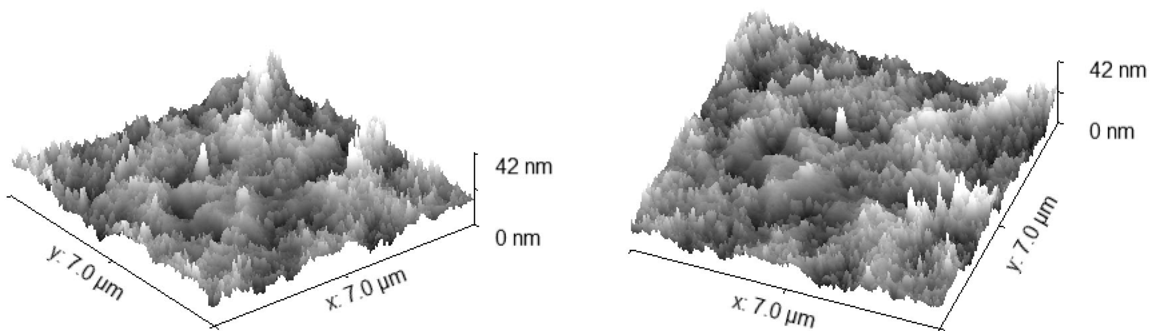

Figure 25: 3D representation of B049 Background.

Figure 25 depicts the 3D AFM representation of the B049 background. As noticed with the Z scale, the background surface height oscillates with a 42 nm range which is not negligible.

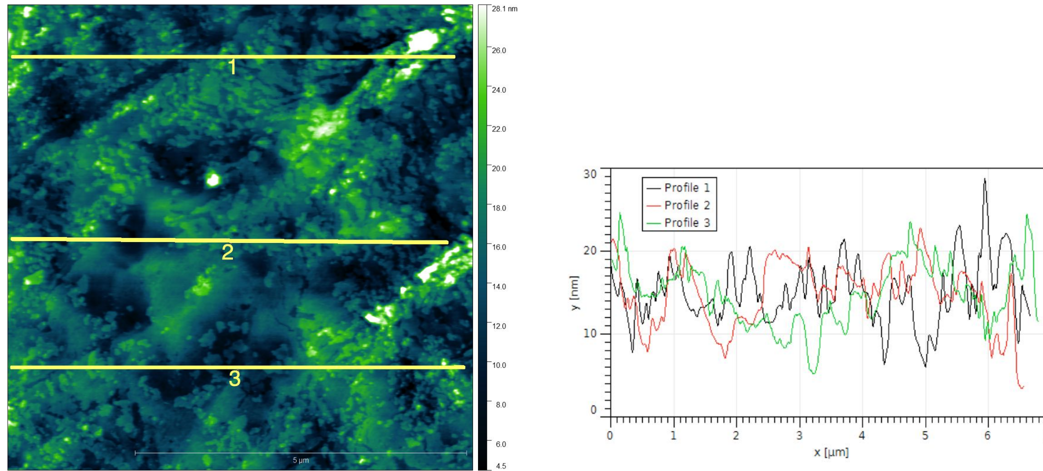

Figure 26: Data analysis of B049 Background.

From the data analysis depicted for the AFM image shown in figure 26, an overall background containing holes on its surface with a depth of 11.5 nm and irregularities of 12nm were noted. Therefore one can say that features on the surface vary by ca. $\pm$ 10 nm which is shallow in comparison to the thickness of the sample of 4.5 μm. In this example, the RMS roughness is 4.1 nm which is a piece of reliable information due to the close field of view. Indeed a low density of dust contamination throughout the surface was noted in this example.

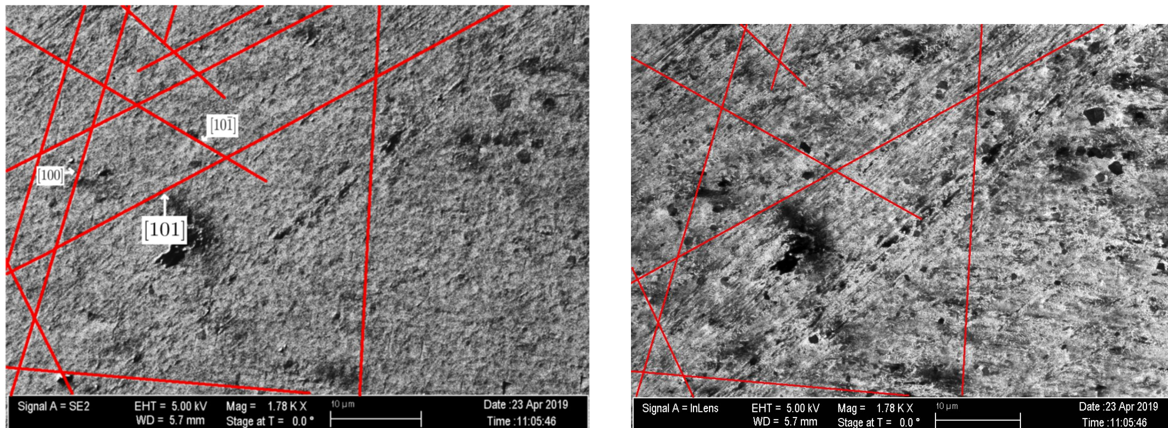

Figure 27: B049 background taken with the SEM ZEISS NEON.

Figure 27 shows SEM micrographs of B049. The left micrograph was obtained using an Everhart-Thornley detector whereas the right micrograph was obtained using an Inlens detector. The difference between these two detectors is that the Inlens detector detects

only secondary electrons for producing a true secondary image. In contrast, the Everhart-Thornley detector will also detect a small portion of backscattered electrons, which will give us more information about the topography of the surface of the sample.

Consequently, line defects due to misfit dislocations due to lattice mismatch between the epilayers and the substrate are less visible on the left micrograph.

The highlighted red lines on the left picture are defects on the surface of the heterostructure. These defects are line defects due to misfit dislocations oriented as planes normal to the [100], [101] and $[10\overline{1}]$ directions.The presence of many lines on this sample showed that the epilayer thickness could have exceeded the critical thickness for lattice relaxation but we need further investigation to confirm this theory. An investigation using the AFM will be conducted in order to determine which layers are responsible for these defects.

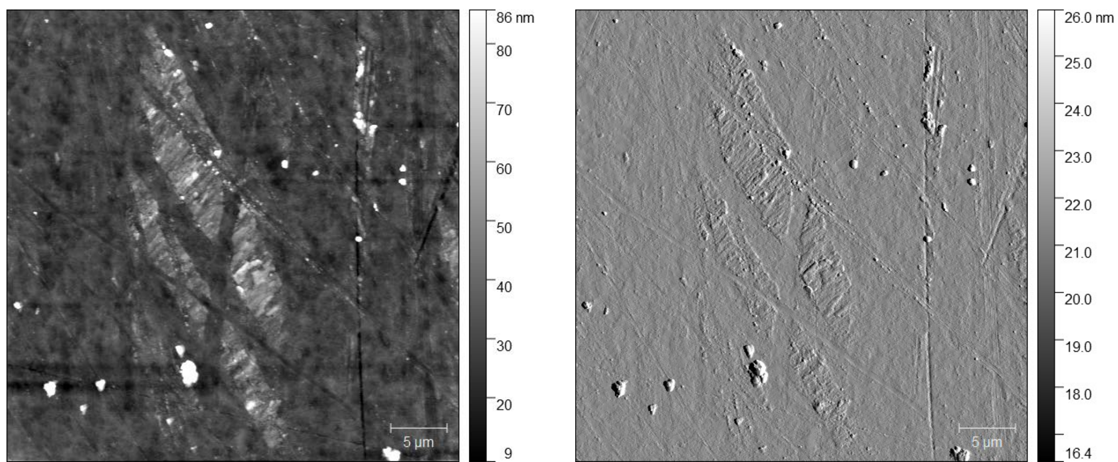

Figure 28: Line defects due to misfit dislocations taken with the AFM.

As seen in figure 28, the AFM shows that the surface is covered with line defects which are due to misfit dislocations.

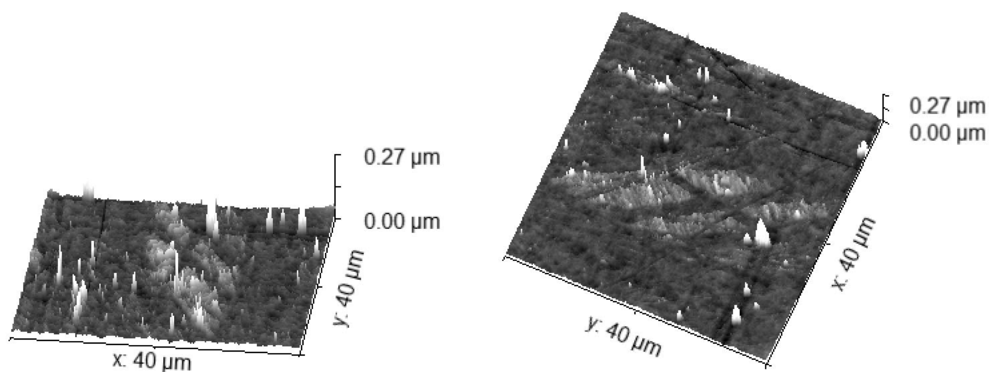

Figure 29: 3D representation of the line defects due to misfit dislocation observed on the surface of B049.

The 3D representation of the surface, figure 29, does not give information about the depth of the lines on the surface due to the fact that the only emphasized features are dust contamination.

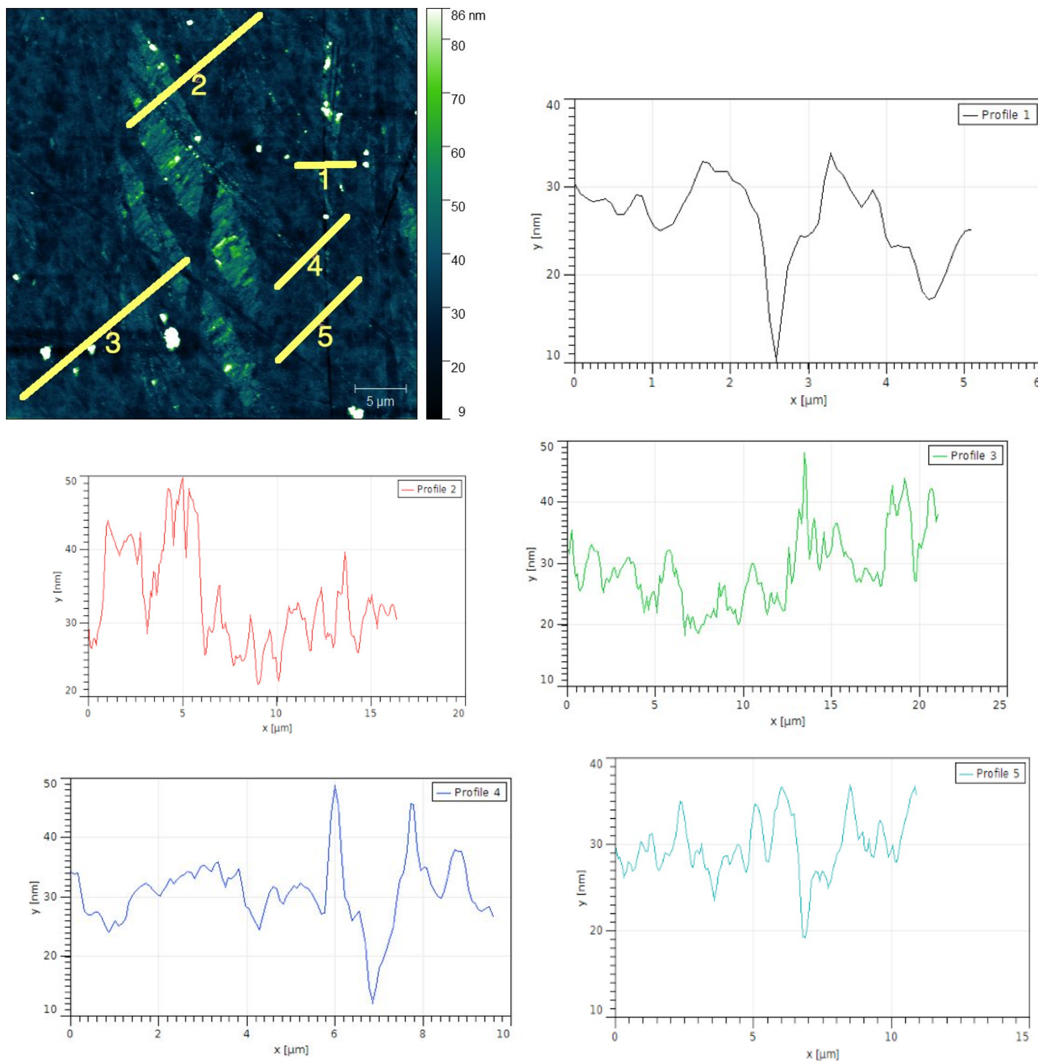

Figure 30: Data analysis of the line defects due to misfit dislocations taken with the AFM.

We extracted the line profiles at different points along the line defects due to misfit dislocations (fig.30). Taking a closer look at profiles 1 and 4, the line profiles drop abruptly and increase in the same manner, inducing that we actually measured the depth of the line defects. From profile 1 and 4, line defects with a depth of 30 nm and 40 nm were measured respectively. Comparing this depth to the layer structure of B049 in figure 24, it would mean that the cap layer is almost fully relaxed since 40 nm is the thickness of this layer. In this example, the RMS roughness is 10.3 nm due to the dust contamination on the surface. By averaging the RMS roughness on various sites on the

surface an average roughness of 7 nm was obtained.

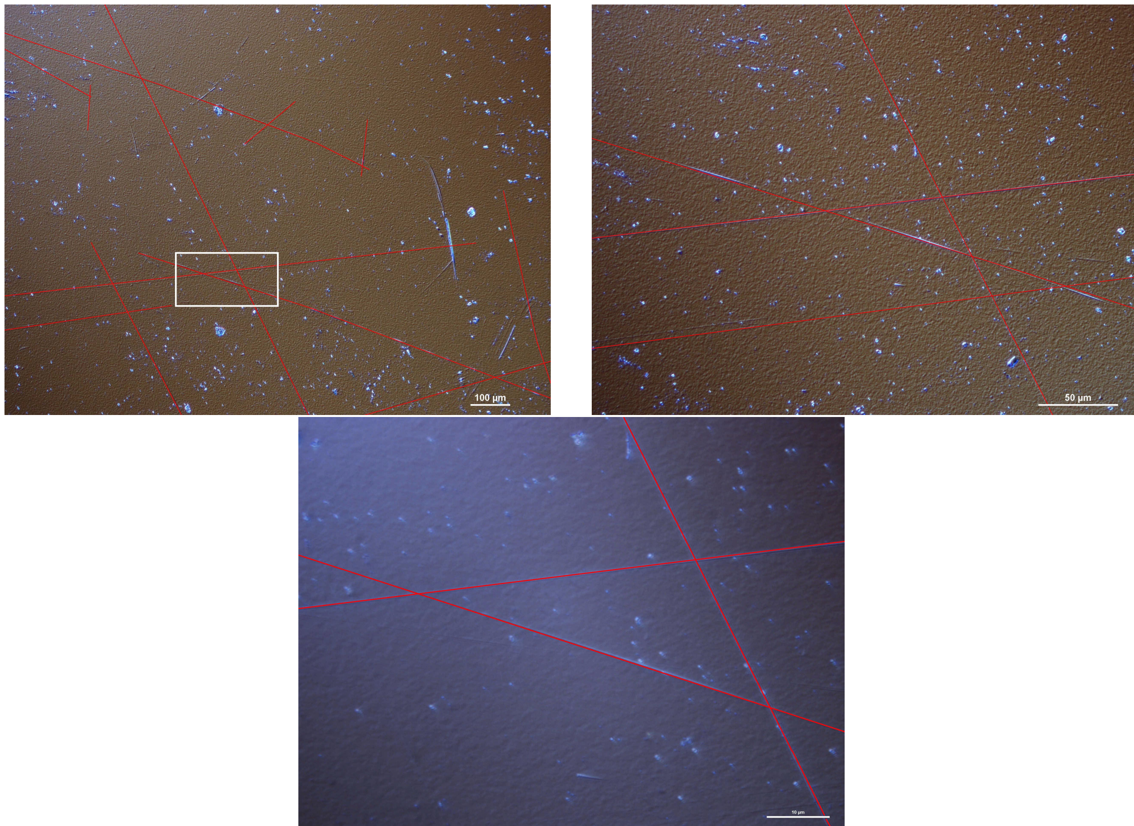

Figure 31: B049 background image taken at different magnifications (10x to 100x) with the DIC microscopes.

In figure 31 the line defects due to misfit dislocations are still noticeable using the DIC microscope. However, the blue features on the surface due to dust contaminations were noticed.

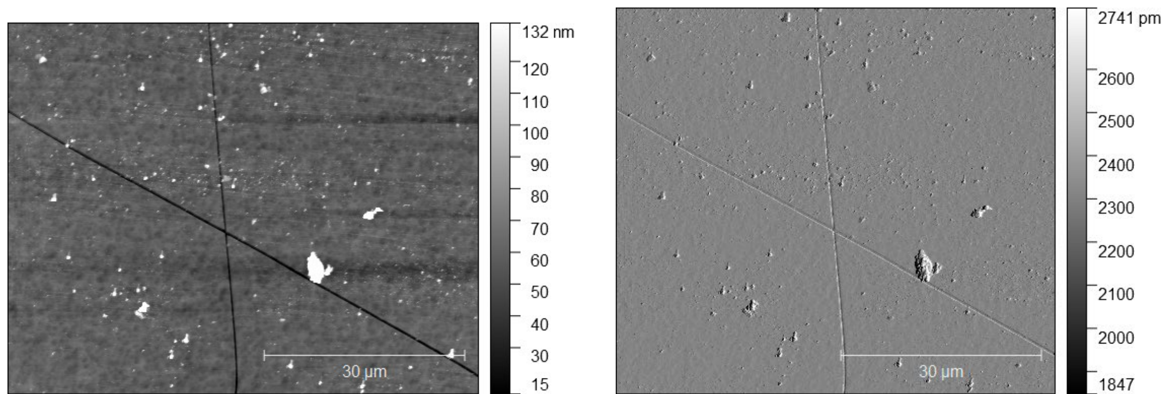

Figure 32: Line defects due to misfit dislocations zoom taken with the AFM.

Figure 32 exhibits the line defects due to misfit dislocations seen under the AFM at high magnification. (7 μm by 7 μm).

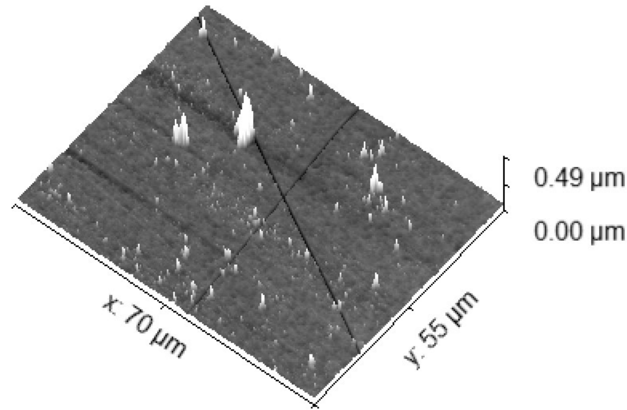

Figure 33: 3D representation of the line defects due to misfit Dislocation zoom observed on the surface of B049.

As noted in figure 33 no information about the depth of the lines was obtained due to dust contamination.

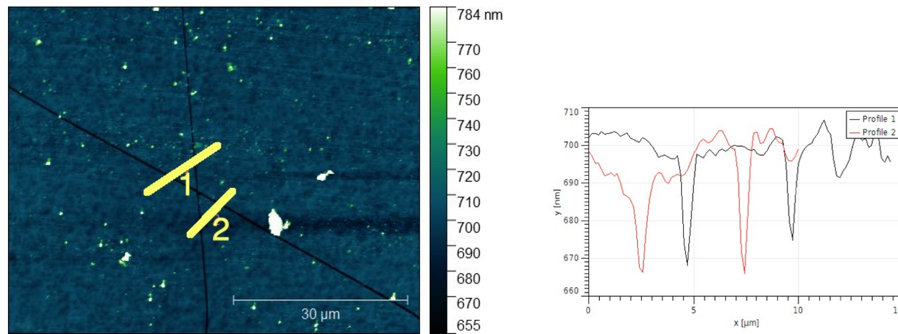

Figure 34: Data analysis of the line defects due to misfit dislocation zoomed taken with the AFM.

By extracting the line profiles at different points along the line defects due to misfit dislocations (fig.34), one can measure the depth of the defects when the line profiles drop abruptly and increase in the same manner. From both profiles, the line defect depth is 30 nm, which means that the depth is close to the InSb quantum well thickness and may affect the electron mobility.

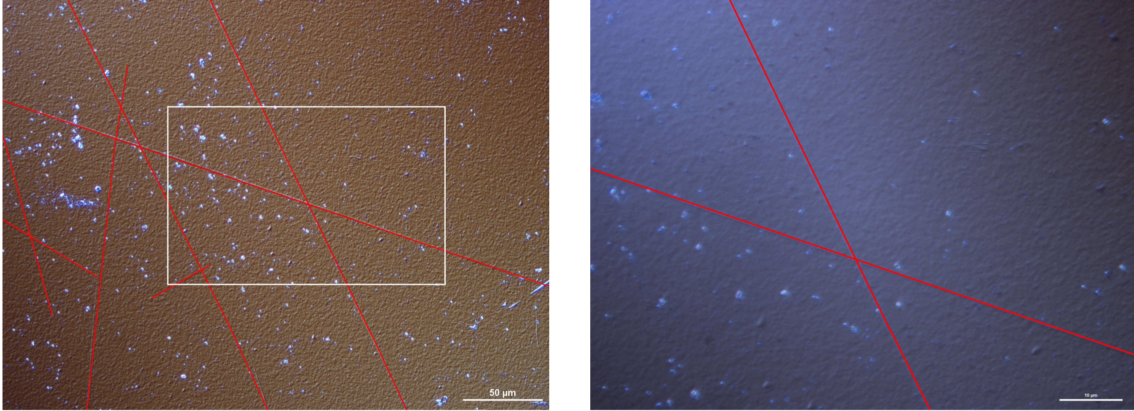

Figure 35: Misfit Dislocation Zoom taken with the DIC microscope.

From the same point of view but using the DIC microscope (fig.35) the presence of the misfit dislocation that we analyzed previously with the AFM are still apparent.

2.2 B051

The study will now compare the previous sample B049 with the new one B051 similar to B049 but after device processing. Therefore this comparison will study the effect of device processing.

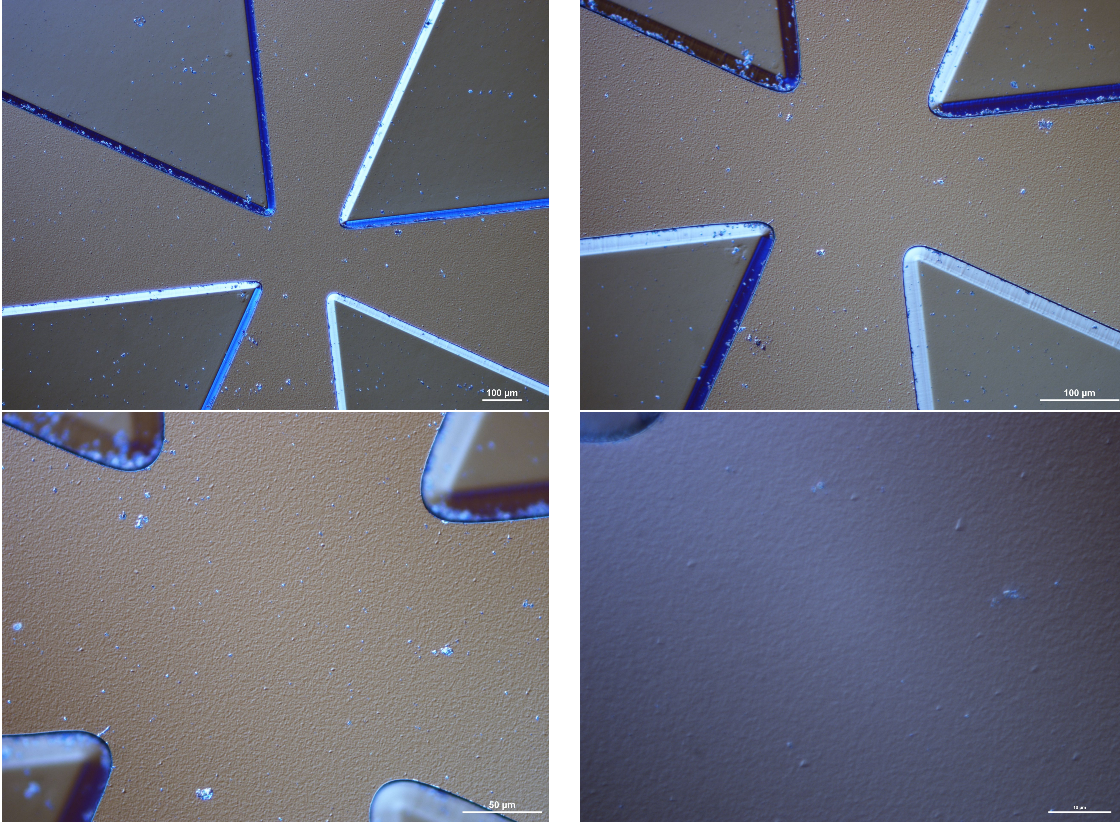

Figure 36: Overall B051 background taken at a different magnification with the DIC microscope.

As seen in figure 36, the non presence of line defects due to misfit dislocations, at magnifications from 10x to 100x, was noted.

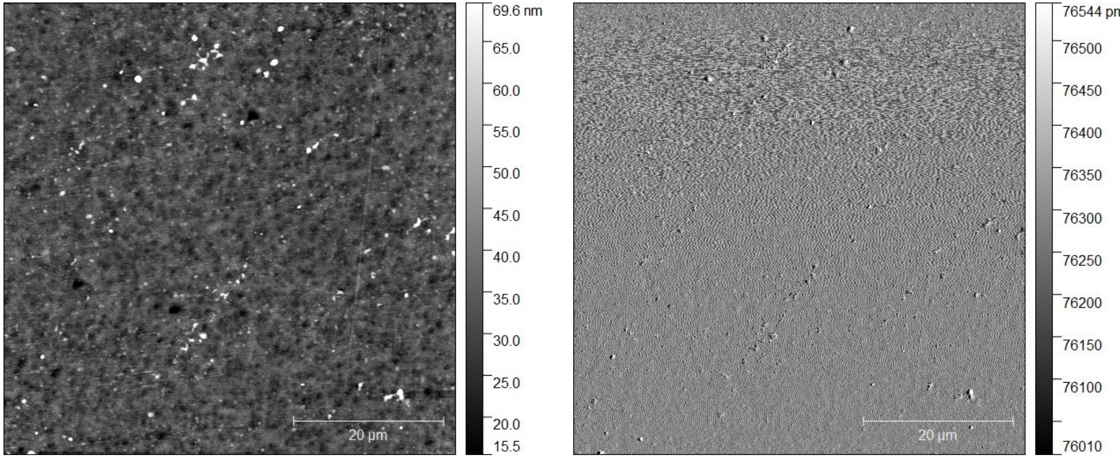

Figure 37: Overall B051 background taken at a low magnification (60 μm wide by 60 μm long) taken with the AFM.

Figure 37 shows a background that is fairly smooth with no misfit dislocations lines on the surface.

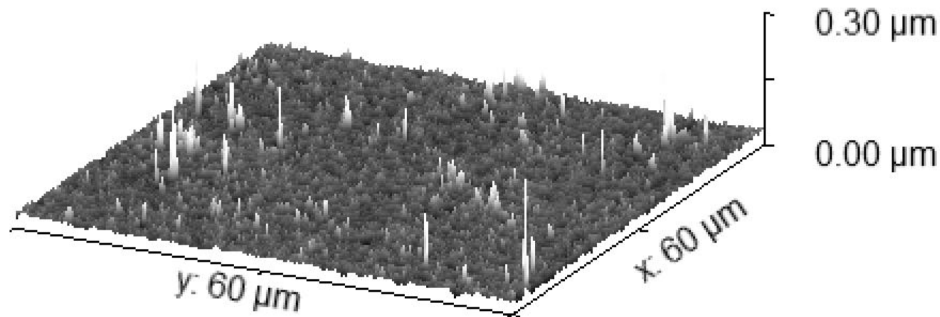

Figure 38: 3D representation of the B051 background.

Figure 38 depicts the surface condition of the background of B051. A smooth overall surface except the white dust contamination features was noted.

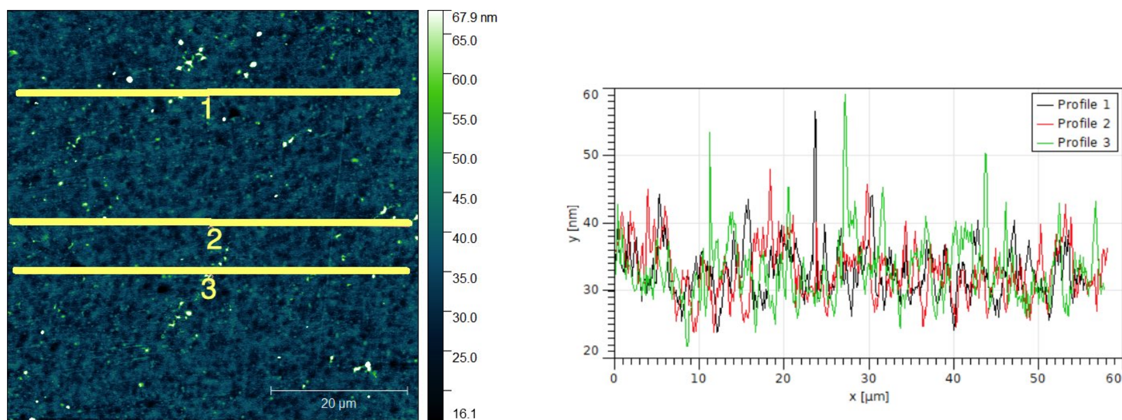

Figure 39: B051 data analysis of the background surface.

From data analysis extracting the line profiles at strategic points on the surface of B051 the graphic above in figure 39 was obtained. The overall background is at a height of 35 nm with irregularities oscillating between $\pm$ 15 nm. In this example, the overall roughness RMS is 6.1 nm. By averaging the RMS using additional data an average RMS of 5.1 nm was calculated. A higher roughness in this example was calculated due to more dust contamination.

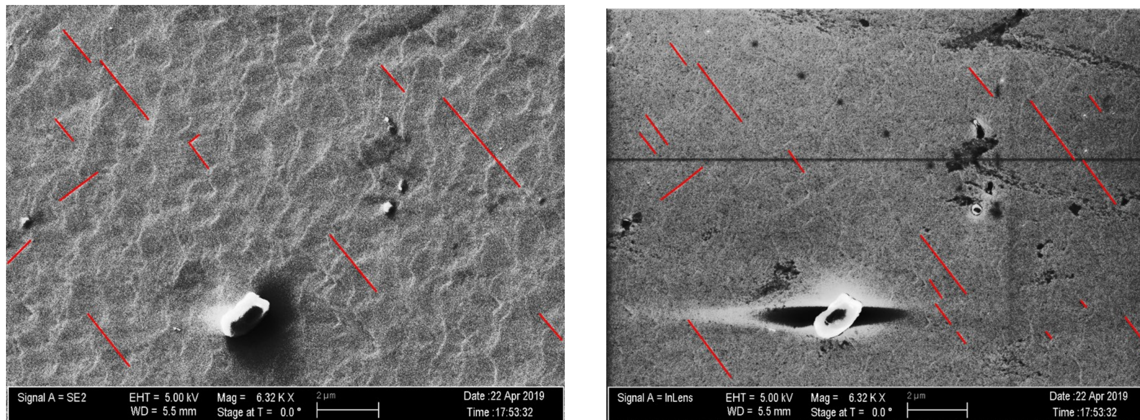

Figure 40: B051 SEM background micrographs.

Figure 40 shows SEM image of B051 background. The left micrograph was obtained with an Everhart-Thornley detector, whereas the right one was obtained with an Inlens detector. The horizontal lines noted on the right micrograph is due to a charging issue of the sample, which did not occur for B049. Indeed the area of the B051 sample was bigger than the one of B049 sample. Therefore the path to the ground was longer. Attenuated line defects due to misfit dislocations including a smoother surface condition were noted in this case. These differences indicate that there are differences between the layer structures of B049 and B051, even though they are nominally the same.

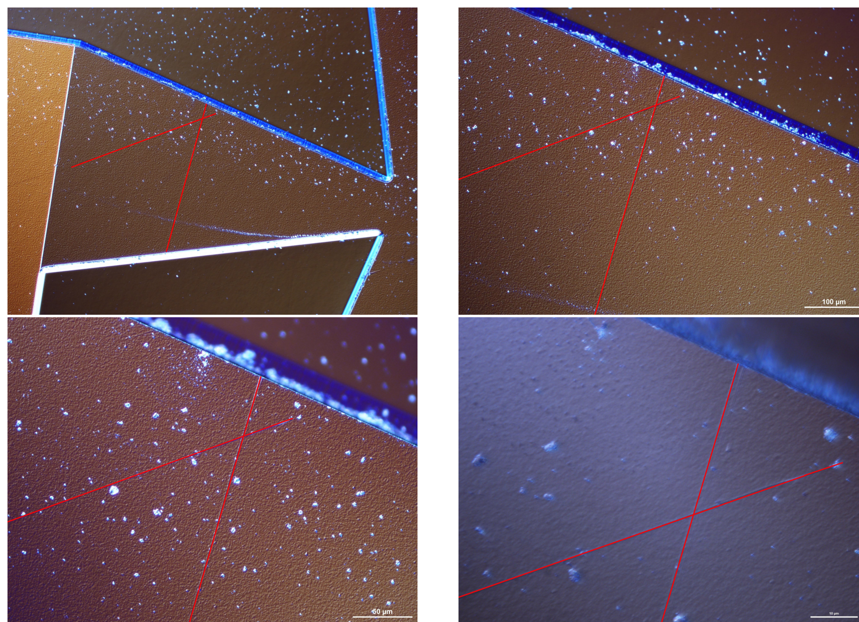

Figure 41: B051 DIC line defects due to misfit dislocations.

The presence of line defects due to misfit dislocations, highlighted in red in figure 41 was noted.A comparison of the surface condition of B051 with B049 from the same field

of view (7 μm by 7 μm) will be now conducted.

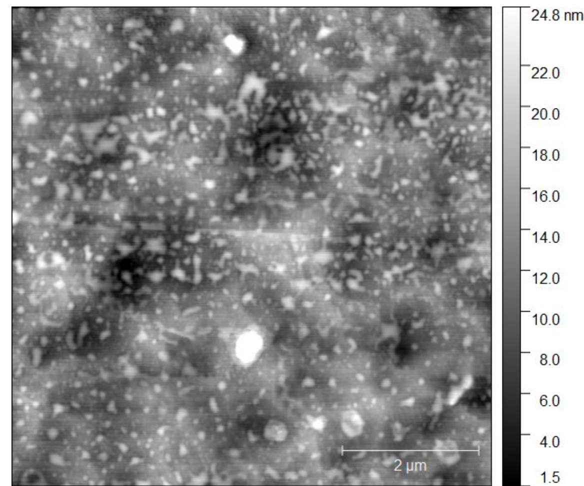

Figure 42: B051 data analysis of the line defects due to misfit dislocations taken with the AFM.

By comparing the background of the B051 sample with the background of B049 (fig.25) many similarities can be noticed. Indeed the surface is rough with an abundance of dust contamination characterized by the white features on its surface.

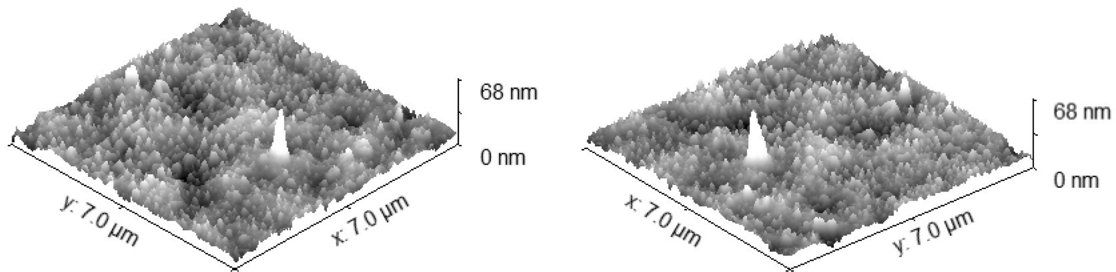

Figure 43: 3D representation of B051 Background using a close field of view (7 μm wide by 7 μm long) taken with the AFM.

The 3D representation of B051 gives more information about the surface condition of this sample (fig.43). By comparing the 3D representation of B049 (fig.25) with this representation one can see that both representations are almost identical except the fact that B051 surface is smoother with less topographical variations.

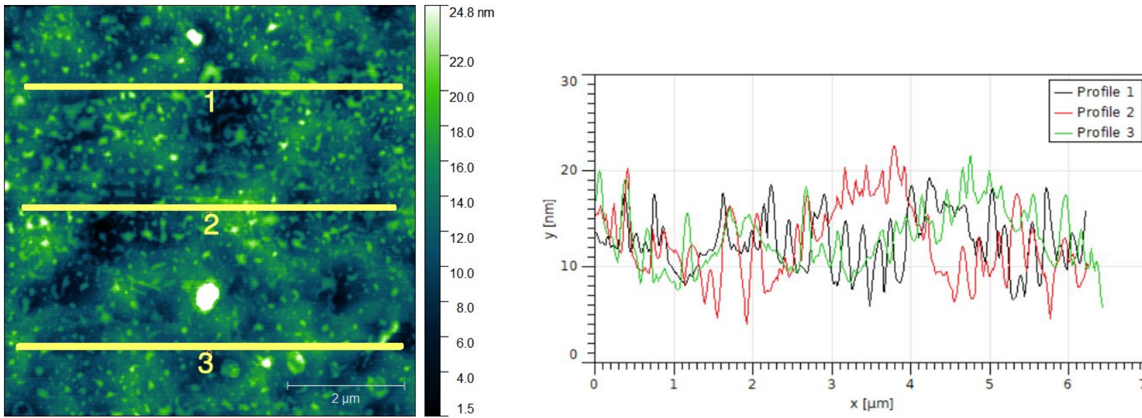

Figure 44: Data analysis of the B051 background using a close field of view (7 μm wide by 7 μm long) taken with the AFM.

From data analysis, figure 44, extracting the line profiles at strategic points on the surface of B051 a graph depicting the overall background variation was obtained. A background height of ca. at 15 nm high with features on the surface of $\pm$ 10 nm was noted. An overall roughness of 3.6 nm which is also a piece of reliable information due to the close field of view was obtained. Using the same field of view on the BO49 sample surface a higher roughness of 4.1 nm was measured previously.

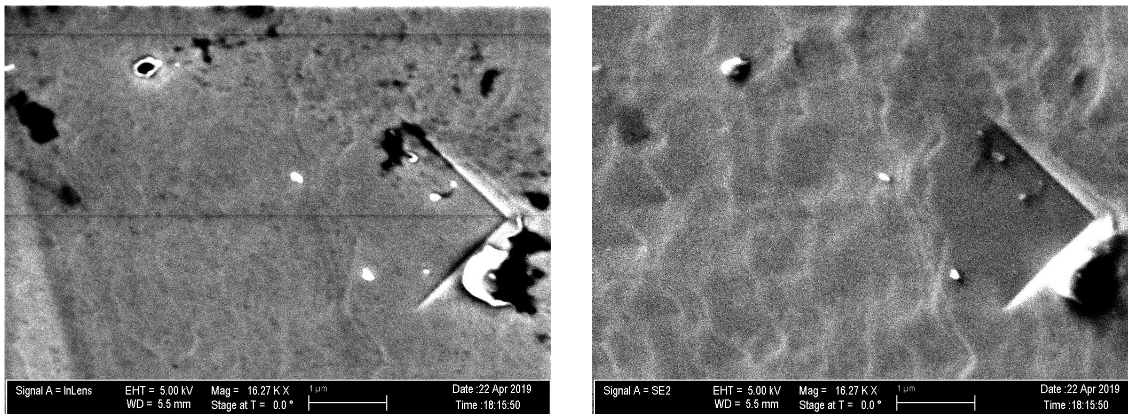

Figure 45: B051 defects taken with the FE-SEM ZEISS Neon 40 EsB.

Figure 45 shows SEM images illustrating defects on the surface of B051. Those defects are typical quantum wells defects. However, the black horizontal lines should be not taken into account since it is due to a charging effect with this sample.

The comparison between B051 and B049 was extended with further analysis on the defects present on the surface using an SEM technique called EBSD (Electron Backscattered Detection). The process of this technique was explained in the background part. An analysis of B049 instead of B051 was made since the line defects due to misfit dislocations are present throughout the surface of B049.

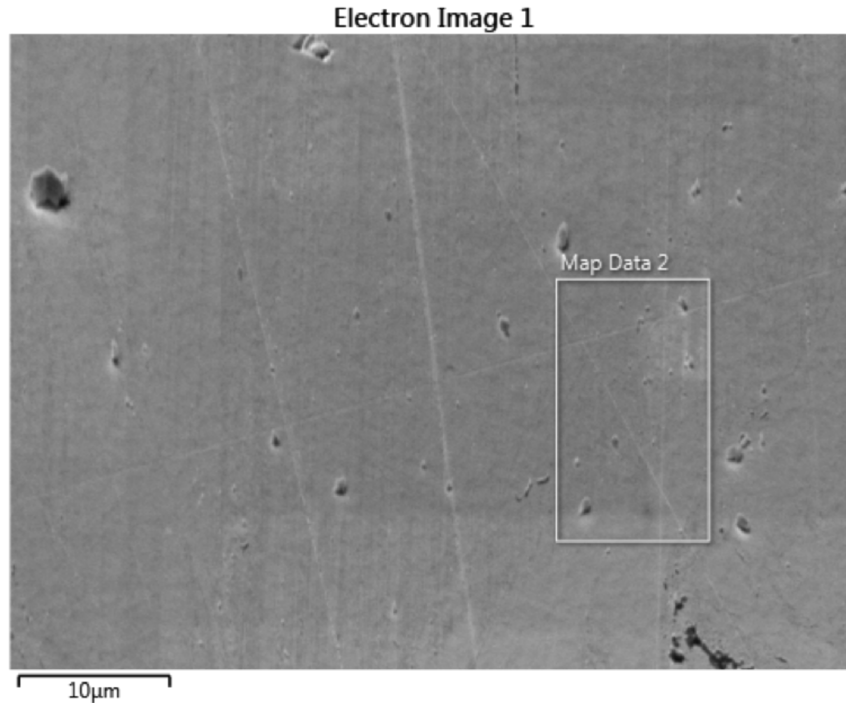

Figure 46: Map of the EBSD analysis on B049 line defects due to misfit dislocations.

Figure 46 shows the area that was scanned for our study using a true secondary image. Line defects due to misfit dislocations were noticed.

2.2.1 Quality of the scan

When one are dealing with an EBSD scan the first thing to do is to look at the different map that the EBSD analysis provides to us. Some of them like band contrast or the MAD (Mean Angular Deviation) give information about the quality of the scan. Therefore it allows us to have critical thinking about the data obtained to determine whether or not the data are reliable.

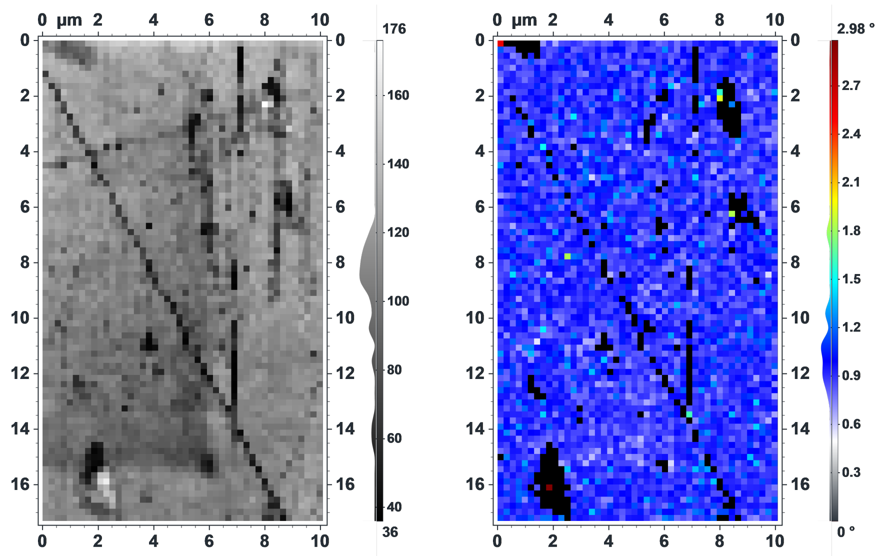

Figure 47: Mean Angular Deviation (MAD) map and band contrast map which give information about the quality of the scan.

Figure 47 displays the band contrast map and the MAD map. The band contrast process is as follows : An EBSD pattern map is acquired to define a certain number of positions to probe throughout the area scanned to get a diffraction pattern at each point. The resolution of the MAD and band contrast map in this study is not high. It is a consequence of the probing mechanism used to obtain an EBSD pattern map. Indeed by defining several points to probe throughout the area, one is setting up the resolution of the resulting EBSD Pattern map. In this example a resolution of 256 by 256 pixels (equals to 256 by 256 points probed) was used because a higher resolution would be more time consuming and also we would contaminate the sample more. Indeed at 3×10^{-6} Torr typical vacuum level for an FE-SEM one is creating 1 monolayer of carbon atoms per second and this would be too thick for a really high-resolution map which could result in a meaningless diffraction pattern. Concerning the band contrast map, at each point of the scan a value of how the scan fit the model (different phases/materials present in the semiconductor) is determined and it is represented through the band contrast using a greyscale base, 256 shades of grey, zero corresponding to black and 255 corresponding to white. Indeed a darker point on the band contrast map is synonymous to a poor fit and a lighter one is synonymous to a better fit.

In figure 47 the overall band contrast map is at a greyscale close to roughly 110-120 as seen on the vertical greyscale bar. This value is close to the median greyscale level (122) which means that the scan is overall reliable. The only poor fit spots (black spot) noticed on the band contrast map are due to dust contaminations or throughout the line defects due to misfit dislocations. The line defects due to misfit dislocations appear as poor fit areas due to a shadow effect. Indeed they probably deserve a better fit but they appear as black since the incoming electrons probing these spots are not reflected to the

EBSD phosphor screen. Therefore the software has no information from the incoming electrons in these areas it defines them as poor fit areas. Concerning the Mean Angular Deviation (MAD) Map, at each point of the scan, the misfit angle between the Kikuchi bands used for the model of the scan and the real band is calculated to depict them in the MAD map. A misfit angle of 0.5 degrees is considered as an excellent fit [25] because it is almost impossible to fit the model perfectly. In our case, an average misfit angle is 0.9 degrees was obtained, which could be considered as reasonable due to the complexity of the semiconductor structure. In addition, from the Aztech Data Base of the different material, an exact concentration of InSb, GaAs, and AlInSb composing our sample was not found.Consequently, by just adding those three phases separately an error was committed. Nevertheless, this angle is not far from the suitable angle used for an EBSD pattern. Therefore one can conclude that the data that we obtained are reliable.

2.2.2 Orientation Study

The orientation of the line defects due to misfit dislocations present on the surface of B049 will be now studied.

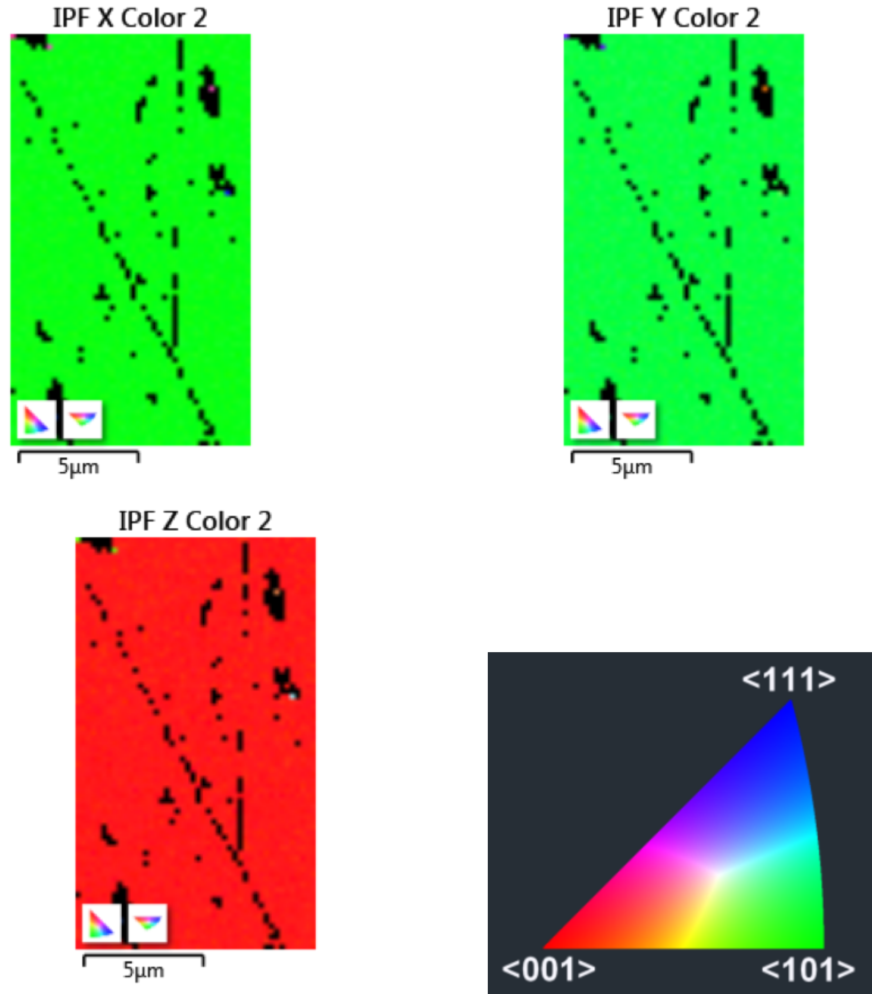

Figure 48: Inversion pole figures of the line defects due to misfit dislocations present on the surface of B049.

In figure 48 the inverse pole figure maps related to the 3 orientations X, Y, Z are depicted. As seen the X and Y inverse pole figure map both face the same orientation, the 101 direction. On the Z direction, it is facing the 001 direction which is the orientation of the substrate. However, as observed in the previous figure 48 we are suffering from the shadow effect along the misfit dislocation lines which means that we do not know the real orientation of these defects.

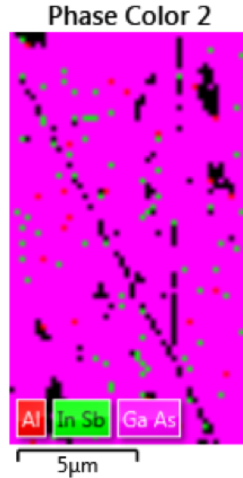

Figure 49: Phase map of the line defects due to misfit dislocation on the surface of B049.

Figure 49 displays the phase map of the EBSD analysis of the surface of B049. One can notice that we are seeing the substrate GaAs much more than InSb or Al. Taking a closer look at the semiconductor structure (fig.17) a thickness of AlIn or InSb epilayers close to 5 μm was measured. However, in comparison to the thickness of the substrate, the InSb layers are thinner which explains why we are feeling the substrate more in the Phase map.

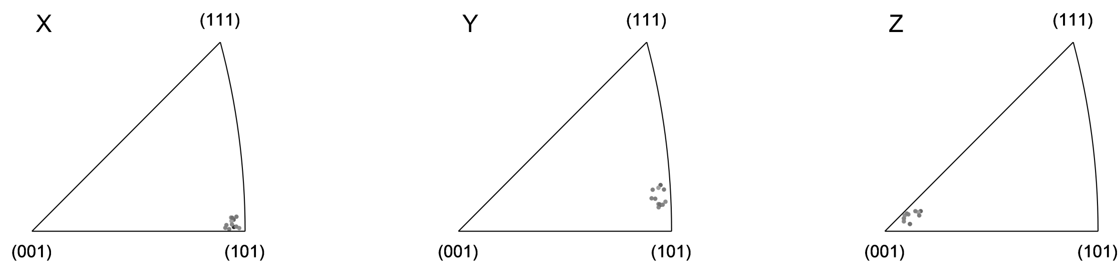

Figure 50: Inversion pole figure map with direct projection.

In figure 50 another representation of the inverse pole figure map is presented. In an inverse pole figure, the axes of the projection sphere are aligned with crystal directions. The directions plotted are the stereographic projection of crystal directions parallel to either the normal direction (ND), rolling direction (RD) or transverse direction (TD) in the sample. The inverse pole figure can help visualize certain types of textures.In an inverse pole figure map, sample directions in the crystallographic coordinate system are plotted because the axes of the projection sphere are aligned with crystal directions.[22]The directions plotted are the stereographic projection of crystal directions parallel to either the normal direction (ND), rolling direction (RD) or transverse direction (TD) in the sample. Therefore an inverse pole figure can plot the different direction in terms of the

major crystal directions [100], [110] and [111].The main advantage of the representation above in figure 50 is that in an inverse pole figure, each data point appears as a single point. Consequently using this representation we have more information about the number of points pointing in each major direction. The triangular shape of an inverse pole figure is based on the Laue group of the relevant phase. This determines the size of the "unit triangle" such as the symmetrically equivalent space in the whole stereographic projection.As noticed before in figure 48 the X and Y direction are pointing in the [101] direction. However, this representation gives more information. Indeed we can notice that the Y direction is slightly off the 101 direction in comparison to the X-direction which is precisely at the 101 direction. Concerning the Z direction it confirms that the background is facing the 001 direction.

2.2.3 Grain Determination study

Now the orientation of the area scanned was determined another study trying to know whether or not there is some localized misorientation on the surface of B049 will be conducted. This analyis is called a grain determination study.The misorientation of each pixel with the four (north, south, east and west) neighbors is examined. When the misorientation exceeds the "grain tolerance angle", a boundary is defined. Once all the pixels boundaries are defined, they are regrouped to form grains. From a grain determination with a tolerance angle of 5 and 2 degrees both grain determination maps remained identical.

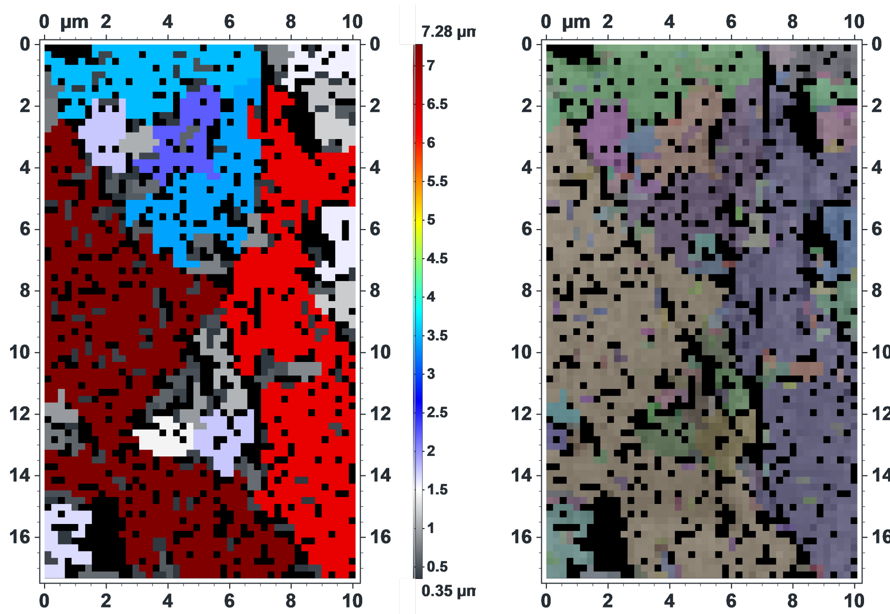

Figure 51: Grain determination analysis for a tolerance angle of 1.5 degrees.

As seen in figure 51, with a lower tolerance angle of 1.5 degrees many different grains were noticed. The difference between the two maps depicted in figure 51 are the following

: The left side map is the main that determine the grain size of the grains as seen from the lateral scale bar whereas the right side only depicts the grain with different colors.One can also see that the major grains detected are on both sides of the line defects due to misfit dislocations. It is a useful analysis which shows that the line defects have some consequences on the orientation of the overall background.

2.3 Conclusion

The study of the InSb quantum well structure shows how the surface condition of a semiconductor can change from one sample to another, even though in theory they should be identical. The EBSD analysis is really useful in this study, showing that the substrate orientation can change from 1.5 degrees because of the line defects due to misfit dislocations present on the surface of B049. Comparing the theorical composition values with the intended composition that was seen in the introduction, one can notice that the critical thickness is close to being exceeded for the barrier layers. Future work would include using X-ray diffraction to measure the alloy percentages for each material present in the sample in order to determine if the misfit dislocations arose from inaccurate alloy compositions.

3 M Series GaSb Buffer Preparation

In this section, a comparison of four different samples, all based on GaSb using different growth conditions will be made.

The table below shows a breakdown of the growth conditions of the GaSb buffer layer structures that were grown.

Sample	Etched	OD T (° C)	Growth T(° C)	Sb heat/cool (Torr)	Sb growth (Torr)	V/III
M371	No	515	424	1.1×10^{-6}	1.1×10^{-6}	2.594
M372	Yes	505	452	1.1×10^{-6}	1.1×10^{-6}	2.594
M373	No	525	498	7.44×10^{-7}	1.06×10^{-6}	2.505
M374	No	525	480	9.42×10^{-7}	1.06×10^{-6}	2.205

Table 3: Description of the samples of the M series.

OD refers to oxide desorption. The oxide desorption process involves heating the substrate to a sufficiently high temperature where 3D formations are observed in the RHEED pattern (sometimes referred to as spots). These would be 3D formations because one is essentially "pitting" the surface as one removes the oxide and leaves behind the group III material. This is a general indication that the oxide layer is being removed from the surface. Generally, and within guidelines discussed in numerous papers for different materials, the substrate is heated up to a sufficient temperature to observe this change in the RHEED pattern, then heating continues for another 10-15°C and then one waits for 10-15 minutes while the oxide desorbs. Many things in MBE growth are experience/experimentally driven so it can be very hard to exactly quantify things, but this is a general rule of thumb.

Sb heat/cool refers to the Sb flux used during the temperature changes from the initial heat up for Oxide desorption and the subsequent cool down to prepare for growth. During the growth of M372, the pyrometer reading varied between 492°C and 518°C during oxide desorption and between 442°C and 462°C during growth. The averages of these values are listed in the table.

Lastly, V/III means the group V (Sb) to Group III (Ga) flux ratio during growth. MBE growth is done under what is called a group III limited growth rate. This means that the stoichiometry driven growth is directly limited by the amount (or flux) of the group III material present. So, the group III flux will be set by your chosen growth rate. For the group V portion, one cannot use a simple 1 to 1 ratio between the III to V. This is because the vapor pressure of the group V materials (given that the growth is carried out at UHV conditions) requires substantially more group V flux than group III flux to avoid the desorption of the group V material during growth. Therefore, the V/III ratio is often reported as a means for one research group to determine the correct conditions for their growth, based on other's growths. I.E. by knowing what one group used for their V/III ratio, and the growth rate that you want to use for your own growth, you can determine the necessary group V flux needed.

All temperatures listed above are as reported by the optical pyrometer on the GenXplor MBE system. Reproducing the exact same environment in the MBE chamber is nearly impossible. However, in this study the temperatures and fluxes were intentionally varied in order to assess the extent to which they may alter the growth outcomes. Indeed by changing the growth conditions this study will determine whether or not it changes the surface condition of each sample.

A lower Sb flux was used during temperature changing pauses in growth compared with the flux used during actual growth for M371 to M374. It is a growth technique well known in the community. A high pressure is not needed since no material is growing at this time. However, a remaining pressure in the chamber is needed during pauses to ensure that there is enough of a background pressure to avoid desorption of the group V material from the surface. From this array of different growth conditions, differences can be noticed from a sample to another. M371 was grown using the conventional method explained by Hao Ye.[37] For M372, one can notice that the substrate was etched using hydrochloric acid. Consequently, the substrate surface has a treatment in advance to the growing process of a thin of GaSb on the surface.This sample is a 1-micron GaSb epilayer on a GaSb substrate etched using HCl acid of concentration around 36.5 % to 38% to remove the oxide on the substrate surface and afterward create a new oxide using deionized water. Indeed this new oxide is easier to remove in the MBE than the original oxide present on the GaSb substrate. Once the new oxide is formed on the substrate surface this one is heated in an MBE to get rid of it before growing an epilayer of 1 μm of GaSb on it.

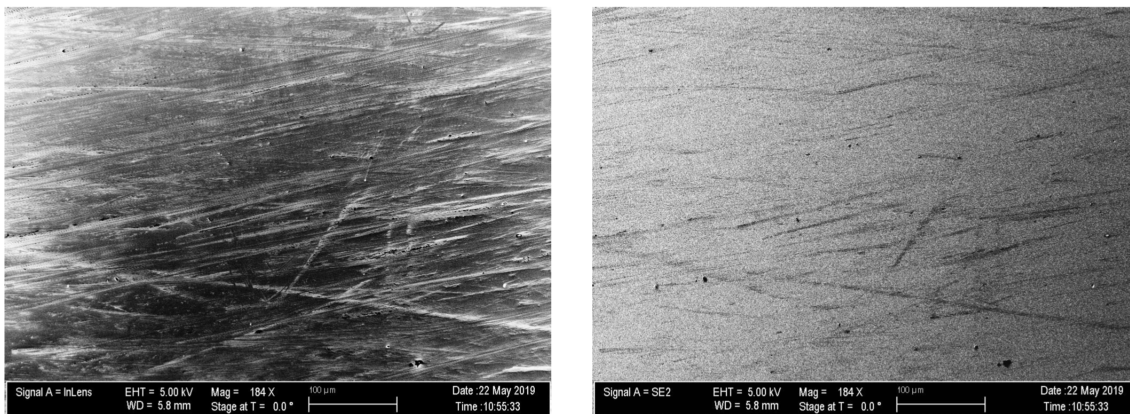

Figure 52: Everhart thornley imaging and In Lens detector image taken with the SEM ZEISS NEON at low magnitude (184 X).

Figure 52 depicts the surface condition of M371 under the SEM at low magnification. A high density of defects was noted. Larger white shapes due to dust contamination were observed on both micrographs. Moreover, some lines on the surface of the sample were observed. These lines are due to carbon contamination issues or due to the cleaving step after taking the sample out of the MBE chamber.

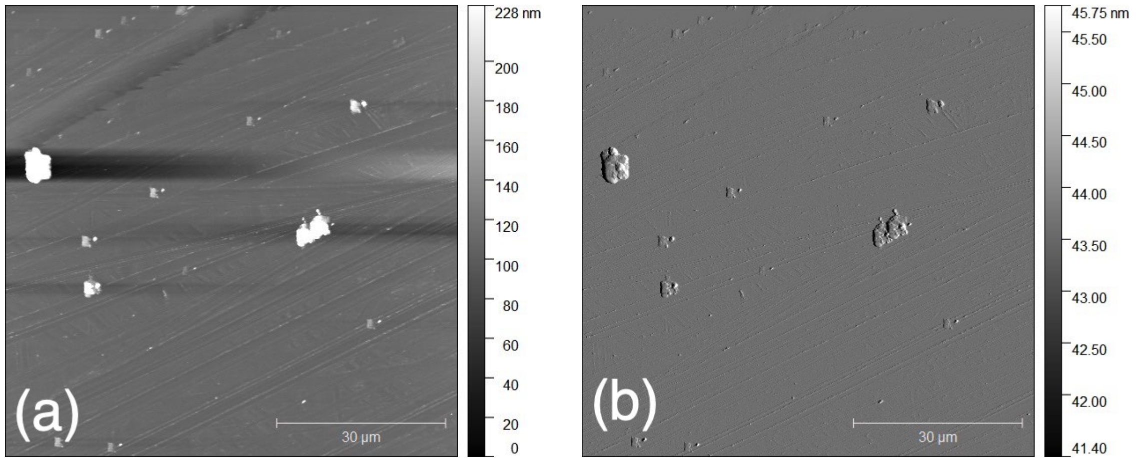

Figure 53: AFM images of the M371 background, figure (a) the height channel which provides useful information about the height of the defects on the sample and figure (b) the amplitude channel which gives the closest representation to what one would be able see using a light microscope.

Figure 53 confirmed the presence of lines and irregularities throughout the surface. Dust contamination characterized by white features were also observed.

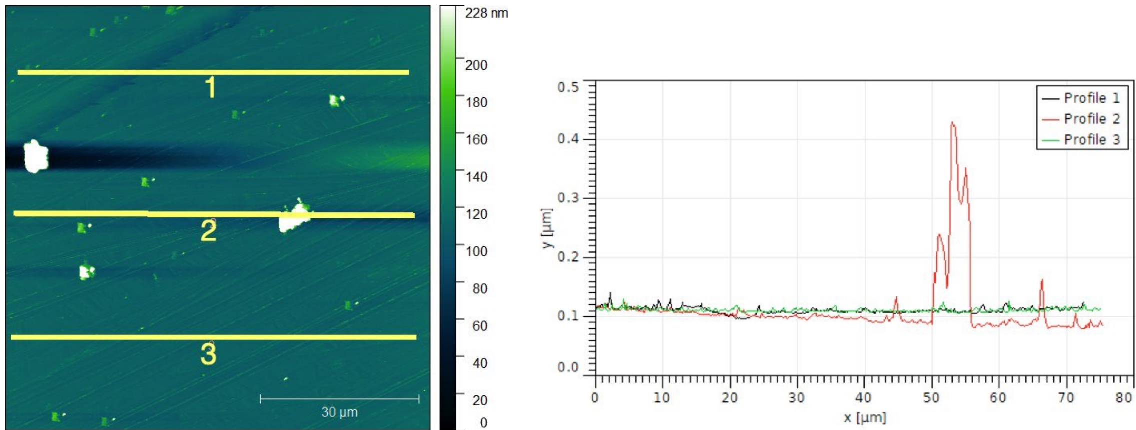

Figure 54: Data analysis of the M371 background taken with the Atomic Force Microscope.

As seen in figure 54, extracted line profiles show a smooth surface condition with very little topographical variations.

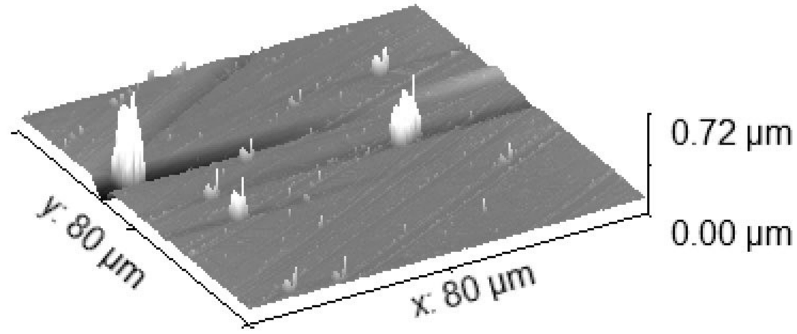

Figure 55: 3D representation of M371 background.

From the 3D representation of the background of M371 (fig.55), irregularities including some lines on the surface of the sample were observed. Using additional data from four different sites on the sample, an average roughness (RMS) of 14.6 nm was noted with irregularities encountered of 48.8 nm height, a consequence of dust residues.

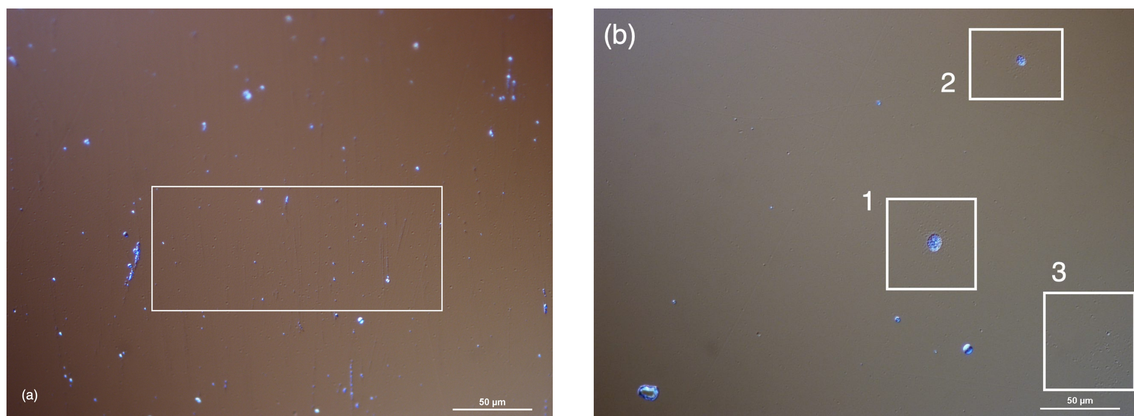

Figure 56: M371 background taken with the DIC Microscope at 40x.

As seen in figure 56, in both cases (a) and (b) the surface is covered with shallow holes, highlighted in white boxes. Blue features on the surface due to dust contamination and some shallow lines were observed. By averaging the density of defects on different sites on the sample a defect density of 5.00×10^4 cm^{-2} was measured.

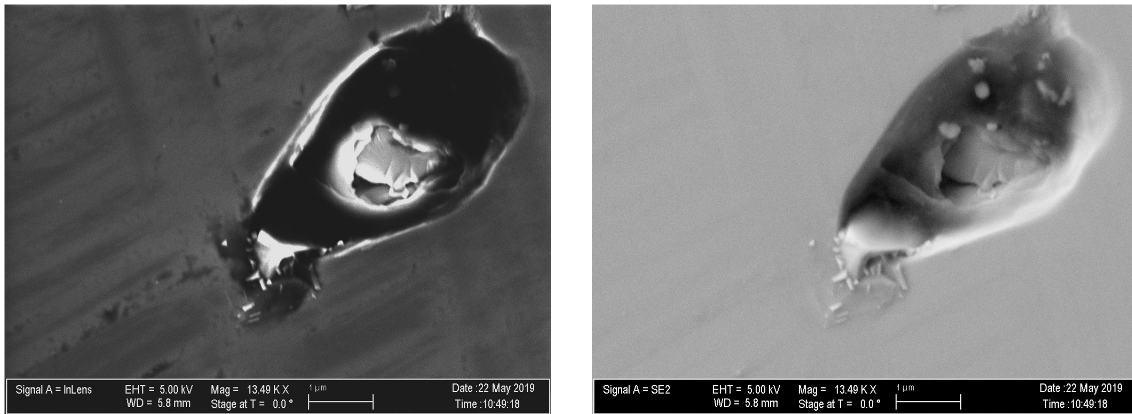

Figure 57: Holes droplets of M371 taken with the SEM ZEISS NEON.

Figure 57 depicts an example of a hole droplet. Some characteristics from those hole droplets were drawn :

- Inside the holes the matter tried to continue to grow which resulted in haphazard shapes
- Around the hole droplets, lines that formed right angles are present
- The hole droplets have an average length of 3 μm

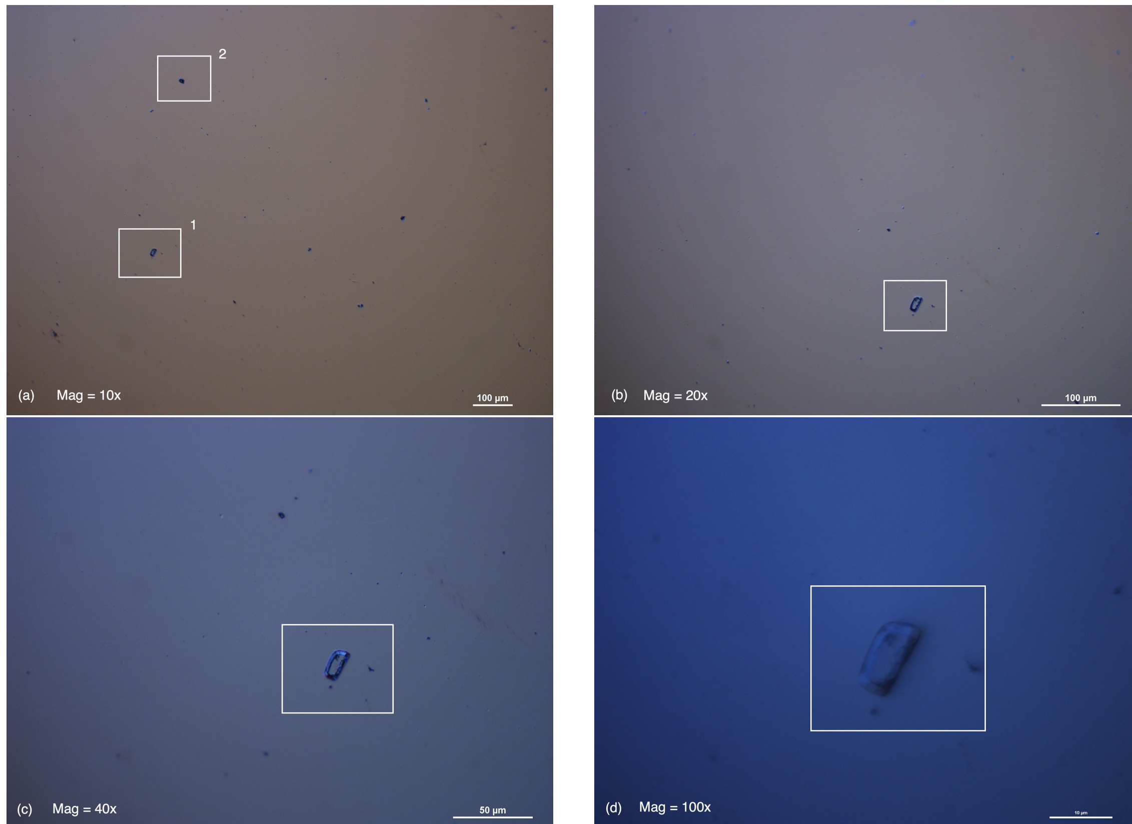

Figure 58: Hole droplets from 10x to 100x taken with the DIC Microscope.

Figure 58 presents an example of hole droplets at different magnifications, from 10x to 100x using DIC optical micrography. The overall background is smooth except the two hole droplets, highlighted in white boxes in figure (a), separated by ca. 800 μm. Blue features throughout the surface were also noted as a consequence of dust contamination.

The second type of defects encountered on the surface were metallic droplets.

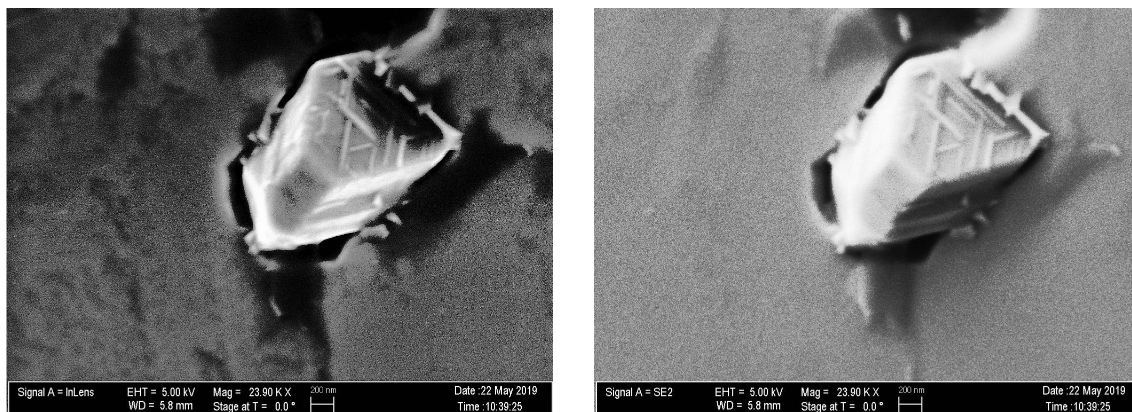

Figure 59: Metallic droplets taken with the SEM ZEISS NEON.

As seen from the SEM images in figure 59, examples of metallic droplets was noted. The shape of this type of defect is close to a hexagonal shape with sharp angles. In comparison to the hole droplet analyzed previously the average length of the metallic droplet is roughly half the one of the hole droplet. Some lines on the metallic droplet itself were distinguished.

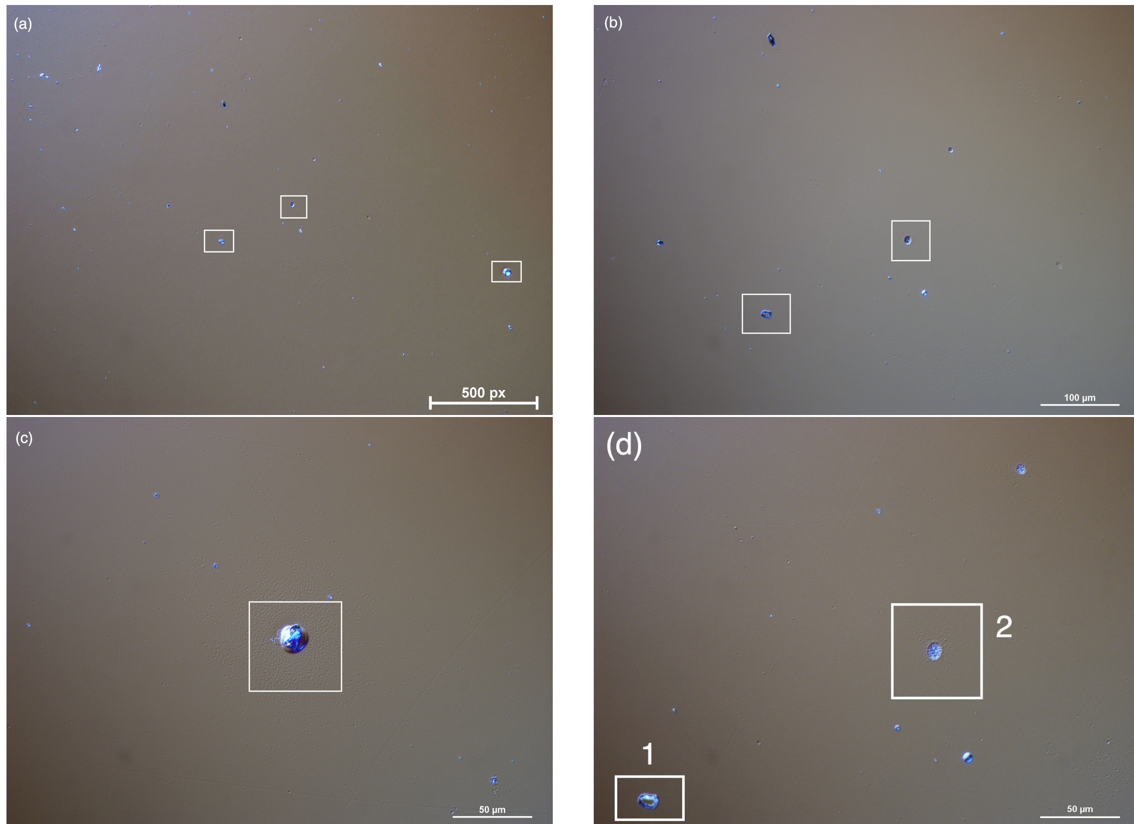

Figure 60: Metallic droplets from 10x to 40x taken with the DIC Microscope.

In figure 60, a low density of metallic droplets, highlighted in white boxes was observed. In figure (a) 500 pixels (px) correspond to a length of 100 μm with an image taken at 10x. Regarding the shape of those defects, a wide range of variations from spherical to hexagonal shapes were noticed. In figure (d), labelled by the number 2, the presence of a spherical defect is surely due to a variation of strain in the material and not a droplet. Indeed the next section will focus on the defects called hillocks which are due to a problem of relaxation in the material during the growth process.

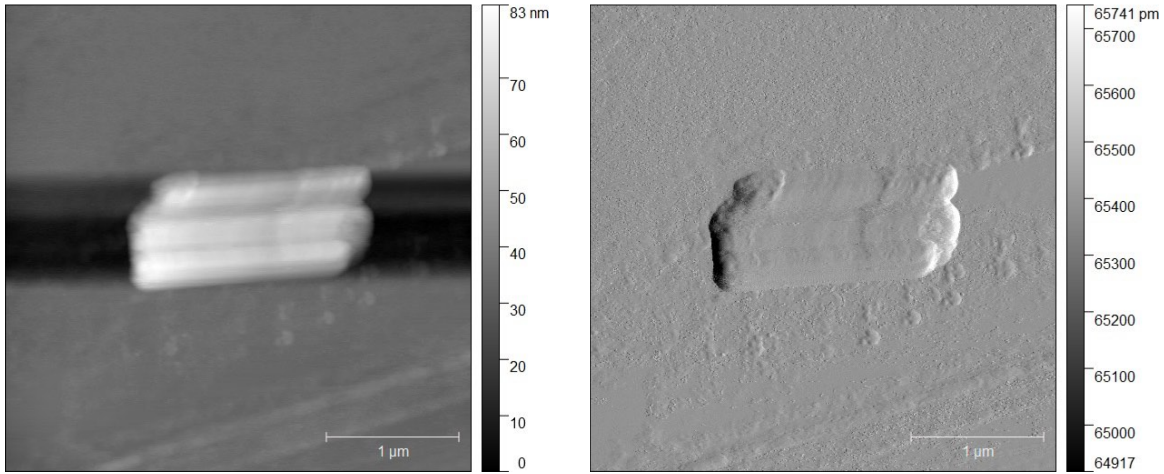

Figure 61: AFM images of an irregularity in M371.

As seen in figure 61, M371 contains a large irregularity. This type of defect is due to a small area that did not grow uniformly during the growth process which formed some irregularities on the surface.

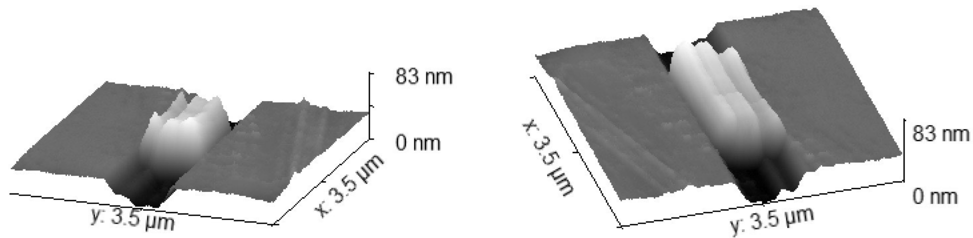

Figure 62: 3D representation of the M371 irregularity present on the surface.

The figure above (fig.62) depicts a 3D representation of this topographical variation. Some shallow areas before and after are lower than the overall background were noted.

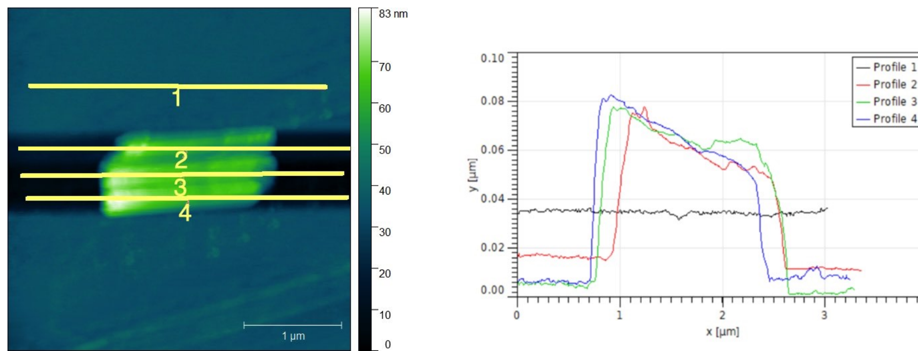

Figure 63: Data analysis of the M371 irregularity.

The overall background in figure 63 is at a height of 40 nm and the maximum height of this topographical variation is 43 nm. When the cantilever is approaching a big defect

on the surface it loses the information of the overall background before and after probing it. It takes some times for the cantilever to adjust its height and therefore produces black areas around the defect. The height of this defect is comparable to ca. 756 layers of atoms which is a non-negligible result. In addition to the previous defects present on the surface of M371, another type of defect called pyramidal defects was detected using the AFM. Studies have reported high densities of mesoscopic defects, often pyramidal in shape [3] [6], at typical densities of 10^4 to 10^5 defects/cm^2. The formation of pyramidal defects in MBE systems has been studied in the past, suggesting their formation is due to morphological instabilities [19]. Indeed the presence of an Ehrlich-Schwoebel barrier, results in an upward adatom current on the island leading to the formation of pyramid defects. The Ehrlich-Schwoebel barrier is an additional diffusion barrier, encountered by a surface atom, when crossing an atomic step.

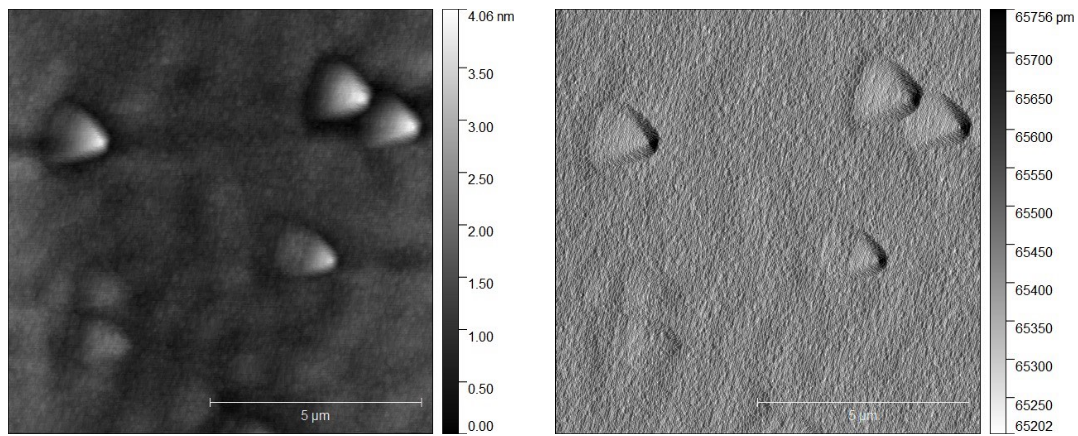

Figure 64: Pyramidal defects observed on the surface of M371 taken with the AFM microscope.

As seen in figure 64, pyramidal defects are omnipresent on the surface of the sample.

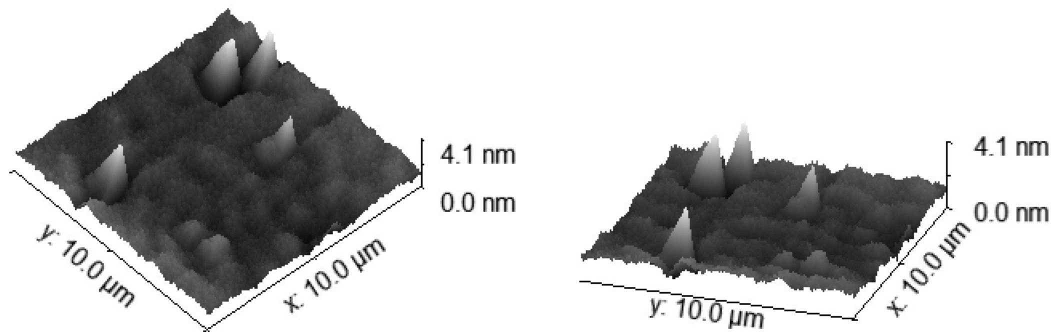

Figure 65: 3D representation of the pyramidal defects on the surface of M371.

As shown in the 3D representation of the pyramidal defects, figure 65, the overall background is not smooth. In sampling various areas of the sample, an astonishing low

average roughness (RMS) of 0.4 nm was noticed.

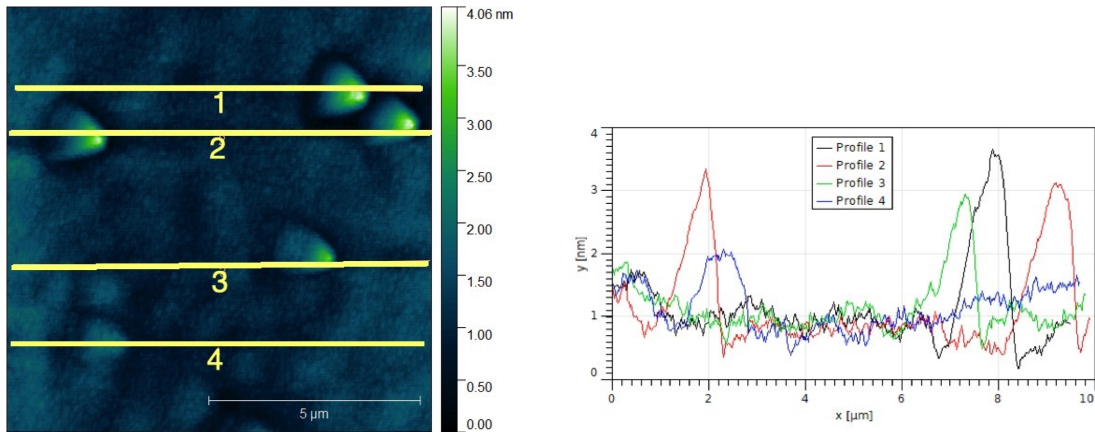

Figure 66: Pyramidal defects observed with the AFM microscope.

By using data analysis (fig.66) in extracting line profiles, the average height of the pyramidal defects on this micrograph is ca. 3.5 nm. Using additional data where similarly encountered defects were scanned, an average height of 4.4nm, which is comparable to 76 layers of atoms was noted. While GaSb homoepitaxy undergoes self-smoothing, the mechanism is slow and requires buffer layers. One study proposes [19] the insertion of a lattice matched AlAsSb ternary layer to temporarily interrupt the step-flow growth. This additional layer results a pyramidal defect-free surface. However in our case, comparing the maximum height of the pyramidal defects of 4.4nm to the actual thickness of GaSb grown on the GaSb substrate, one can conclude that these defects cannot be considered a major issue.

This section will now focus on the second sample of the M series labelled M372.The structure of the sample is similar to the previous one and the growth conditions are almost the same. However, this sample had a surface preparation of the substrate in advance before growing the GaSb layer on the top of it.

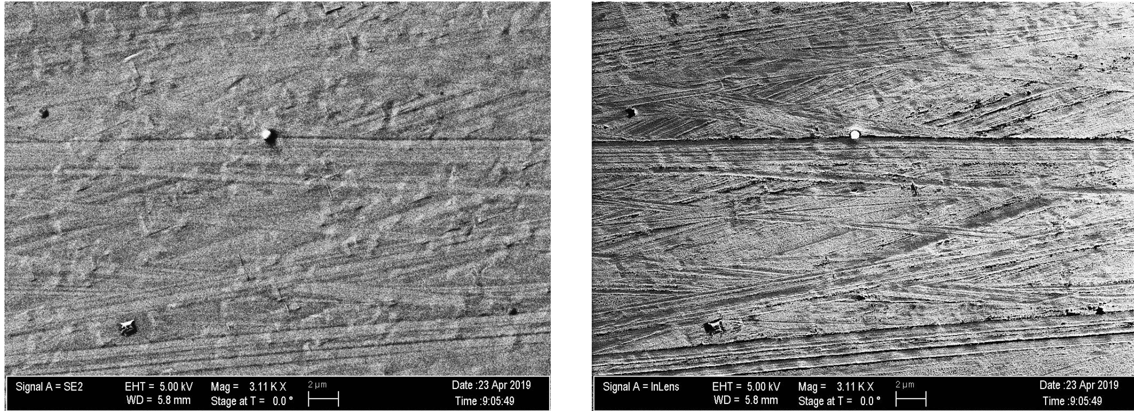

Figure 67: Background of M372 taken with the ZEISS NEON.

The surface condition of the M372 is depicted in figure 67. We can directly notice that the presence of right angles. A higher density of right angle defects on the surface of M372 was observed. Droplets on the other hand are a rare commodity.

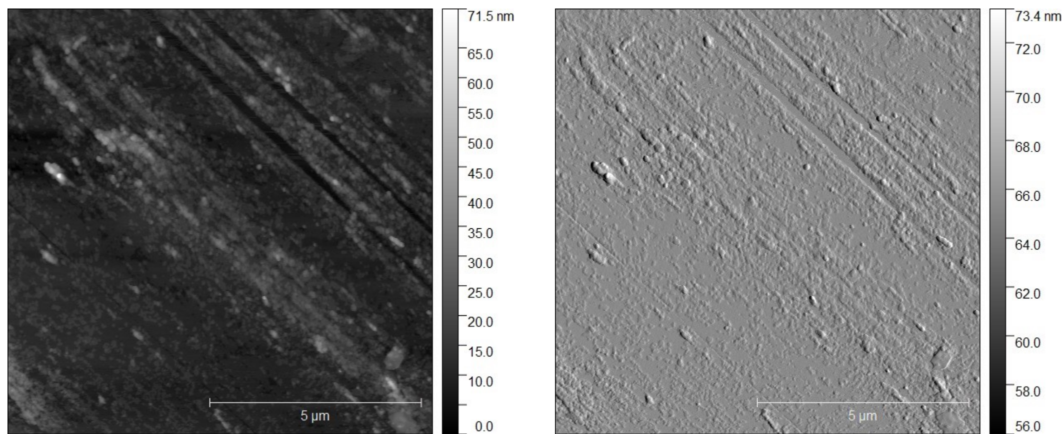

Figure 68: M372 background observed on the AFM.

As seen in figure 68, in addition to the previous SEM micrographs depicted (fig.67), the overall background is not smooth due to numerous topographical variations on the surface. Furthermore, the presence of lines on its surface was also noted.

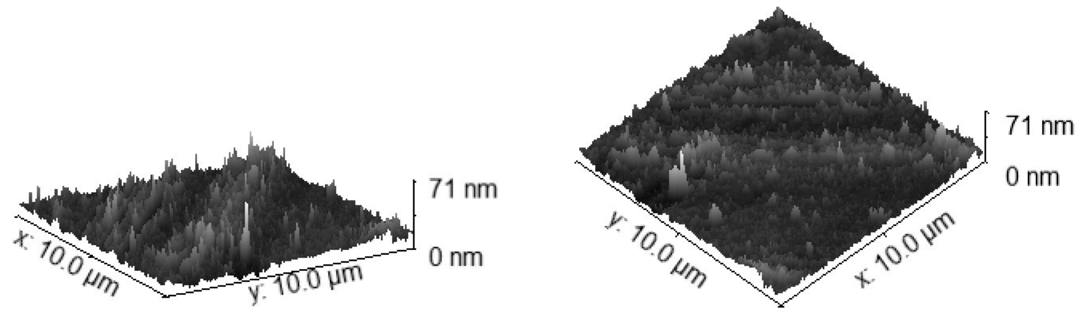

Figure 69: 3D representation of M372 Background.

The 3D representation of the M372 background in figure 69 depicts the surface condition with topographical variations up to 71 nm high.

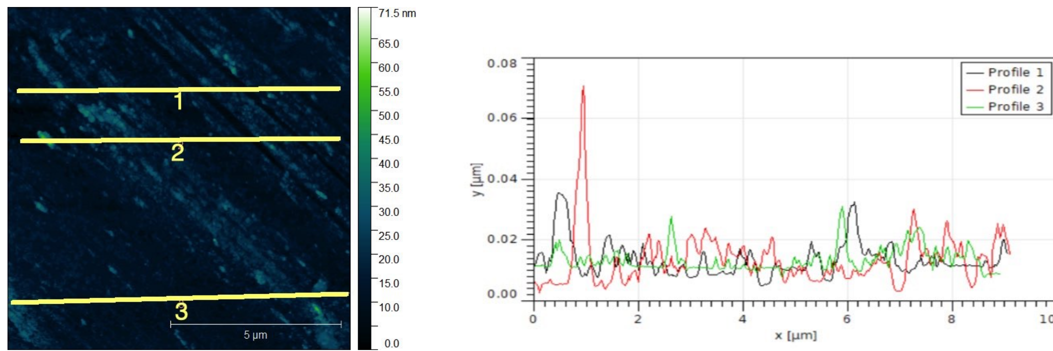

Figure 70: Data analysis of the M372 sample surface.

From the extracted profiles lines in figure 70 topographical variations in this example varying from 0 to 25 nm on average were calculated. Using additional data on different sites an average height of the topographical variations of 26.8 nm and an average roughness (RMS) of 5.3 nm was measured.

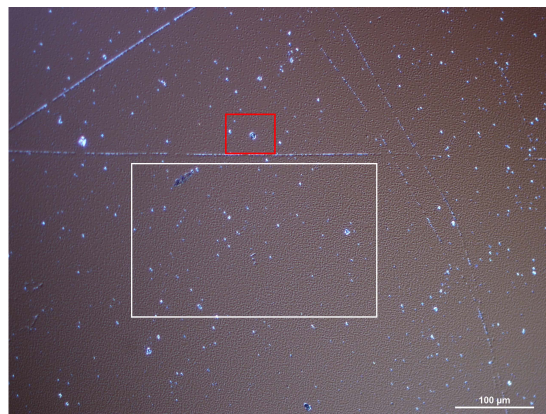

Figure 71: M372 background taken with the DIC Microscope.

As shown in figure 71 using the DIC microscope, some lines on the surface of the sample were observed. However the main feature of interest is the presence of shallow holes, highlighted in the white box, already noticed in the case of M371. Nonetheless, the density of tiny holes is much greater on this sample than on M371. As highlighted in the red box, a hole droplet is also noted. Most of the small blue features seen on the surface are dust contamination which is an inevitable consequence of exposing the sample to atmospheric conditions. By averaging the density of defects on different sites on the sample a defect density of $4.19 \times 10^4\ cm^{-2}$ which is slightly lower than the density of defects of M371 was obtained.

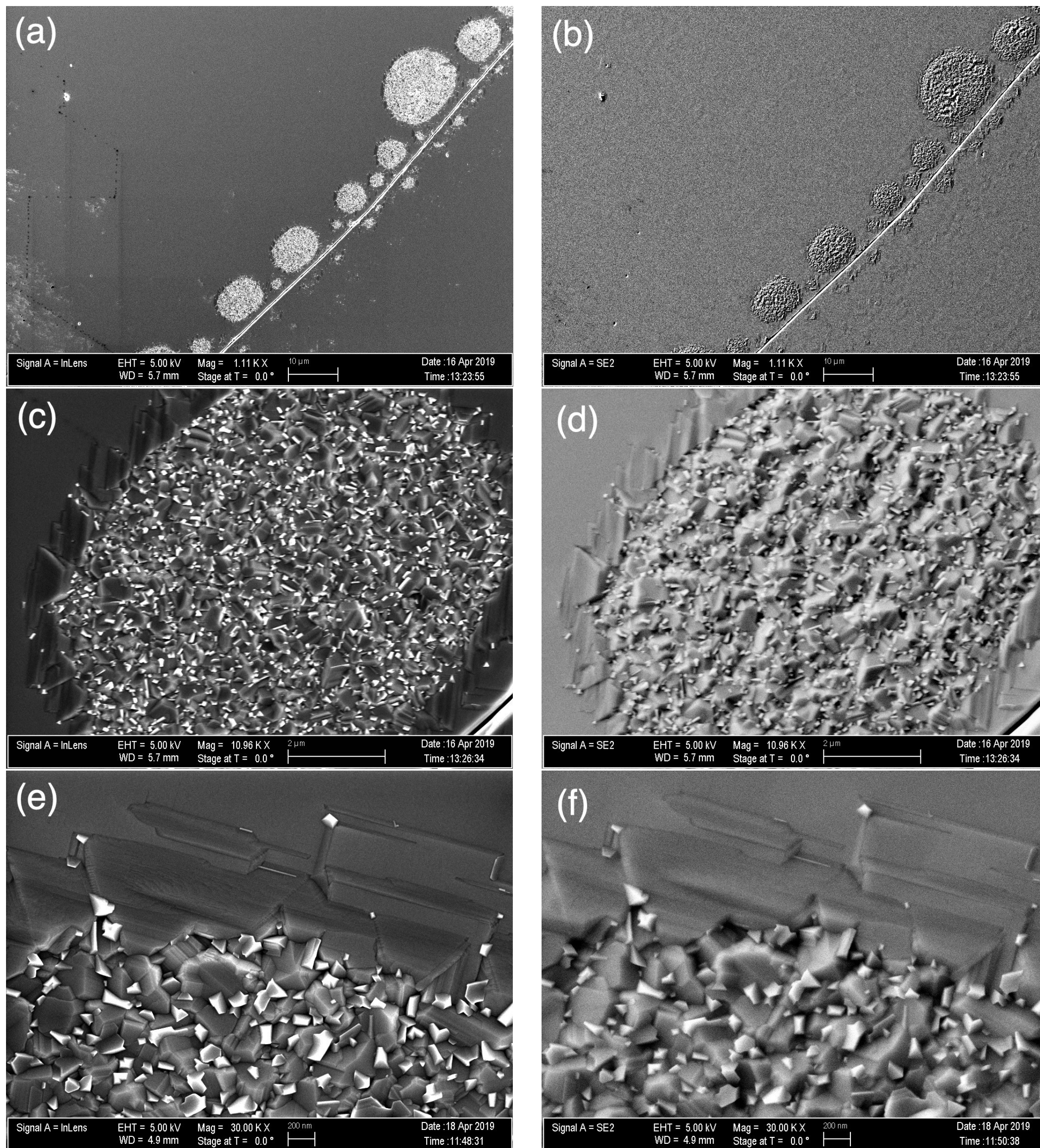

Figure 72: Defect formation along a scratch on the surface of M372 taken with the ZEISS NEON at different magnifications.

In figure 72 the presence of defects along a scratch was observed. Figures (e) and (f), taken at a higher magnification, depict multiple angular defects inside the spheres, which is a consequence of the acid etch to prepare the substrate.

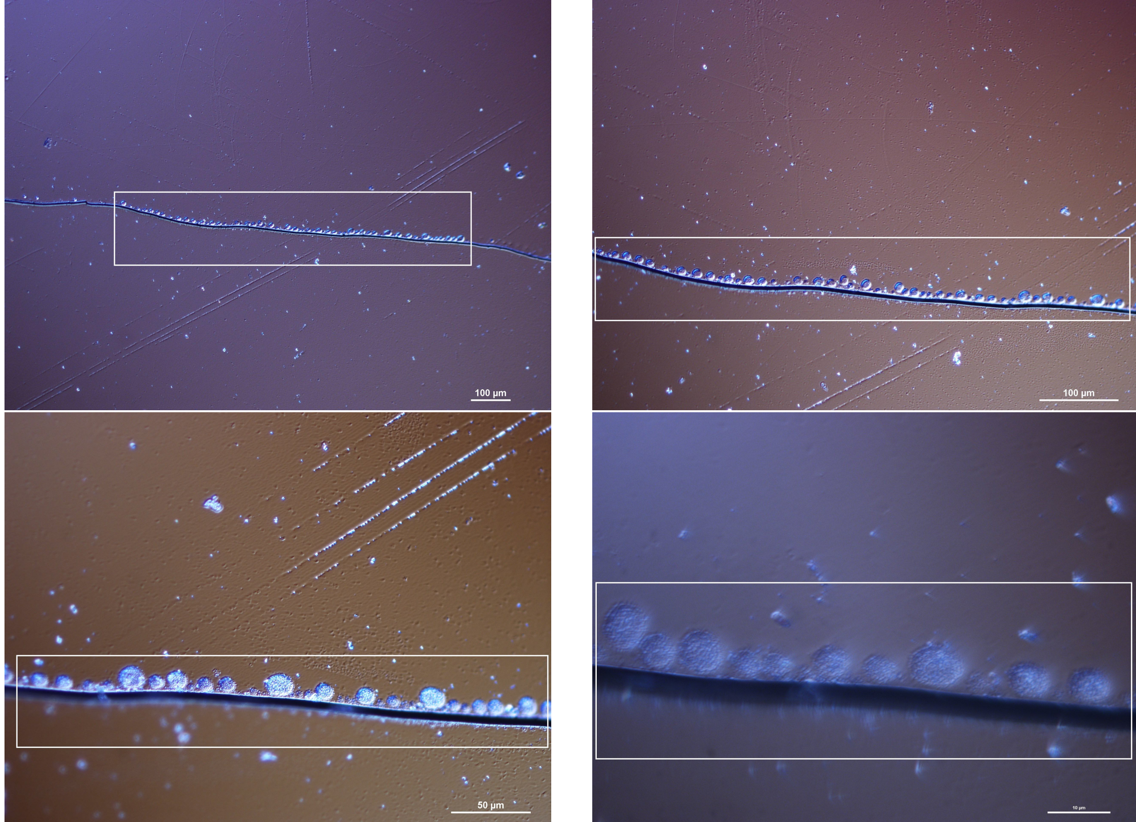

Figure 73: M372 defects along a scratch taken with the DIC Microscope.

In figure 73, highlighted in white boxes, the defects along the scratch at different magnifications using the DIC microscope were observed. However angular shapes present inside the spheres (fig.72), were not noticeable using this microscope due to a lower resolution available. In addition to this specific case of defects along a scratch, further type of defects on the surface of M372 are depicted in the following section.

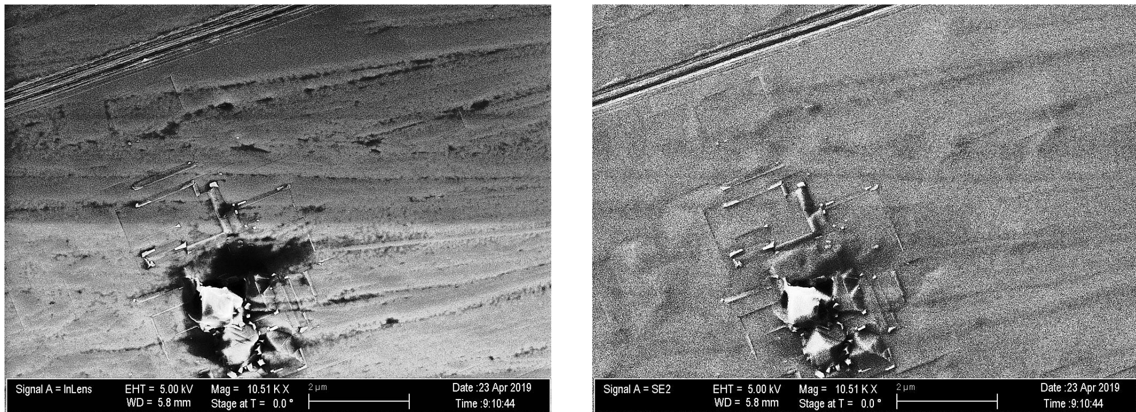

Figure 74: Multiple metallic droplets formation on the surface of M372 taken with the ZEISS NEON.

Figure 74 shows a formation of multiple metallic droplets surrounded by right angle defects previously noticed on the surface of M371. However one can immediately conclude that the density of right angle defects on the surface is much higher on this sample.

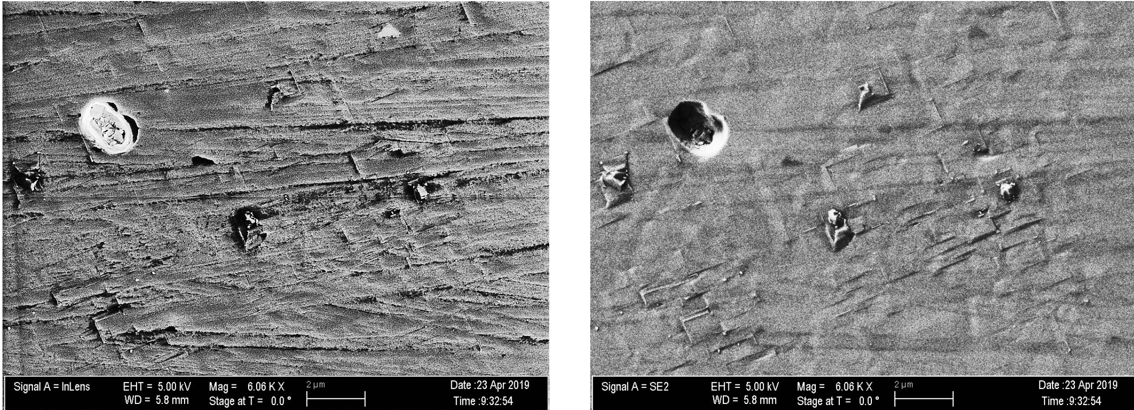

Figure 75: Multiple metallic droplets, holes droplets and right angles line defects on the surface of M372 taken with the ZEISS NEON.

Figure 75 summarizes all the different types of defects encountered on the surface of M372 depicting one hole droplet, a few metallic droplets, and many right angles defects.

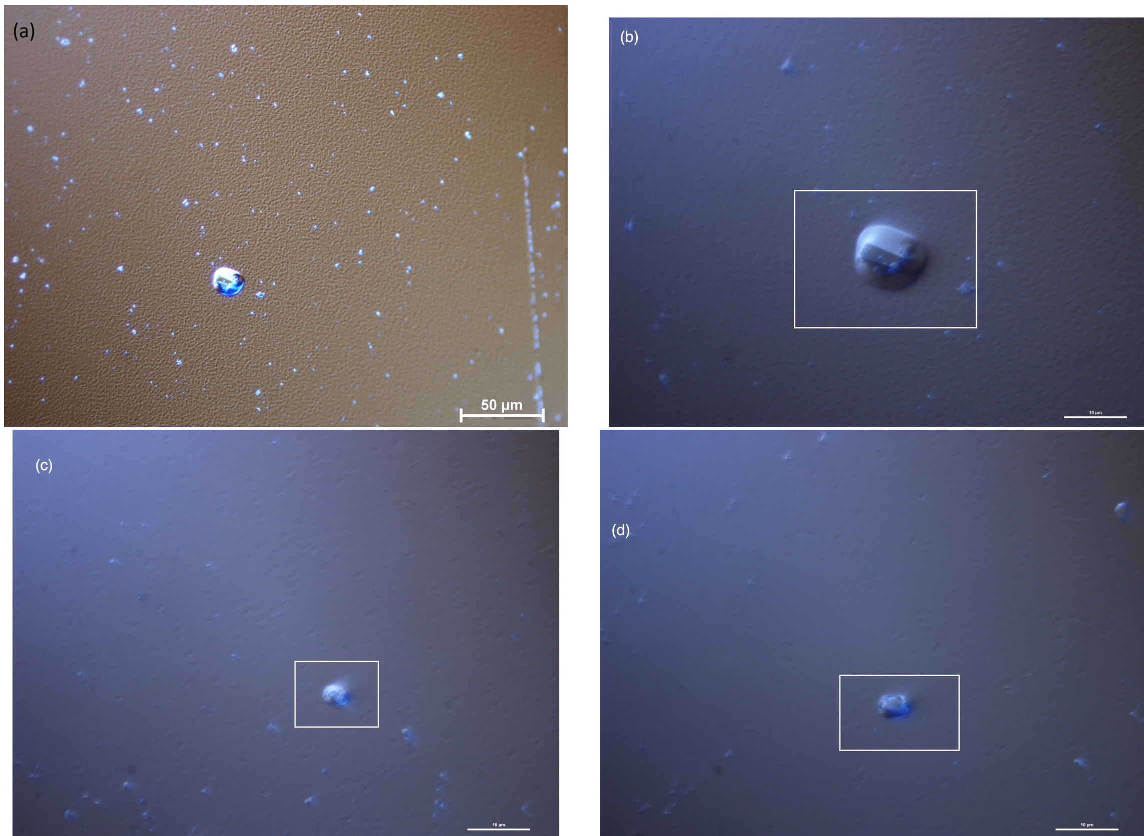

Figure 76: M372 metallic droplets taken with the DIC Microscope.

The different droplets encountered on the surface of M372, in figure 76, have a similar oval shape. In figures (a) and (b) a rectangle shape was noted. The oval shape around the rectangle was probably due to a shock wave when the metallic droplet hit the sample surface during the growth process.From this analysis of M372, a conclusion that the surface roughness of this sample is worse than M371 can be made. The only difference in terms of growth conditions was the acid etch. Consequently, using a surface etching process to prepare the substrate surface is not the appropriate method to grow a sample with a low density of defects.

This section will now focus on the next sample of the M series labelled M373. This sample was grown using different growth conditions. The oxide temperature and the growth temperature were increased by 20°C and 46°C respectively, which is a noticeable difference. Concerning the subsequent cooldown pressure, this value was divided by almost two and the flux ratio V/III was slightly decreased as well.

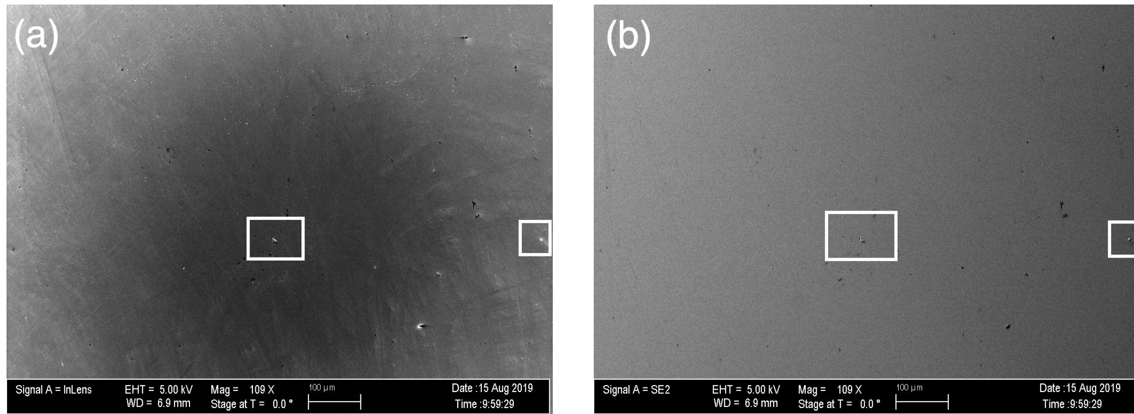

Figure 77: SEM micrographs of M373 background.

Figure 77 (a) was taken with the In-lens detector and figure (b) was taken with the Everhart-Thornley detector. The black spherical shadow in figure (a) depicts the shadow of the electron gun. Indeed because the detector is situated right above the sample it is exposed to this shadowing effect, which is only noticeable at low magnifications and disappears when we increase it. In figure (b) this issue is no longer present due to the fact that the SE2 detector is situated on the side of the sample.The sensitiveness of the In-lens detector to dust contamination was noted with the presence of several white dots in figure (a).Composition wise, droplets on the sample surface, highlighted in white boxes, separated by ca. 400 μm was noted.

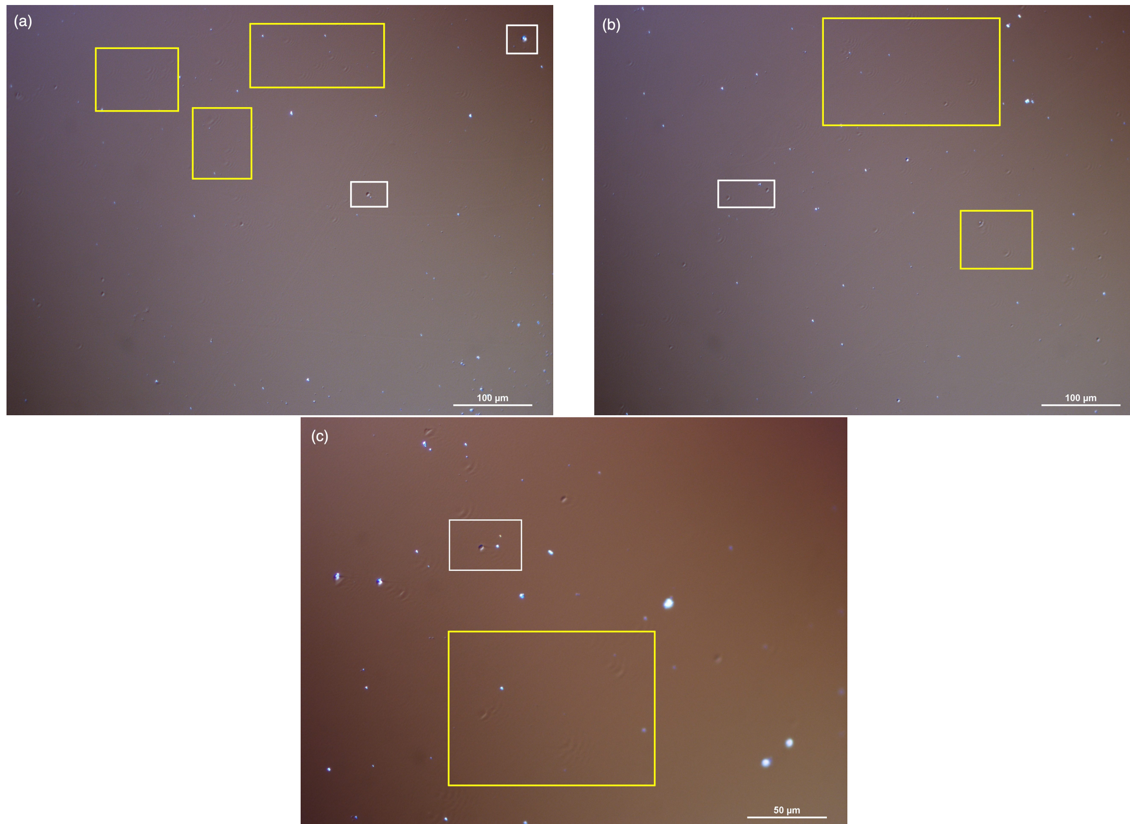

Figure 78: M373 background taken with the DIC Microscope.

As seen in figure 78, tiny holes on the surface of M372 are no longer present on the surface of M373. The overall background is smooth despite some irregularities. Droplets highlighted in white boxes are few in number. By comparing the density of defects with the previous samples analyzed, one can conclude that M373 has a smoother surface. However the ripples highlighted in yellow boxes are interferences with the camrea, as they were not noticeable using the binoculars on the microscope. By averaging the density of defects on different sites on the surface of M373 a defect density of 2.58×10^4 cm^{-2} was obtained.

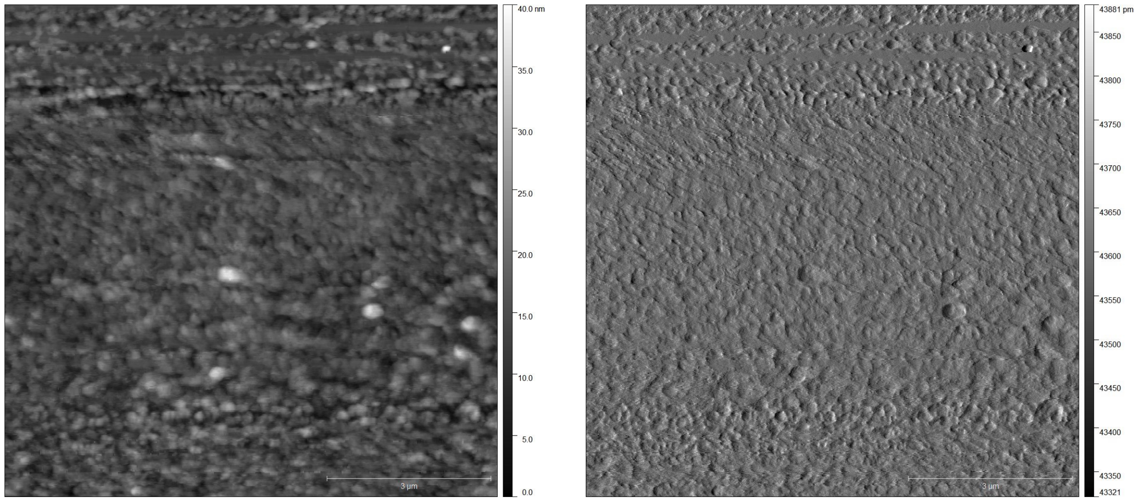

Figure 79: M373 background micrographs taken with the AFM.

Figure 79 shows the uniformity of the M373 surface with no noticeable irregularities. We can notice directly that the surface is much smoother than the previous samples, M371 and M372. Indeed the surface looks uniform with no noticeable irregularities.

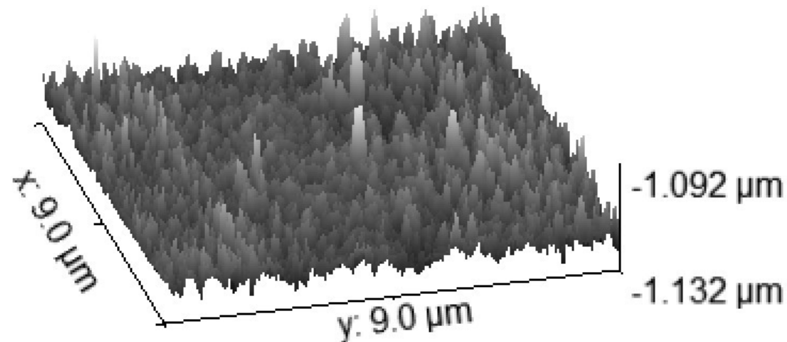

Figure 80: 3D representation of M373 background.

As seen in figure 80, the surface roughness is smoother on this sample. However some shallow topographical variations were noted on the surface.

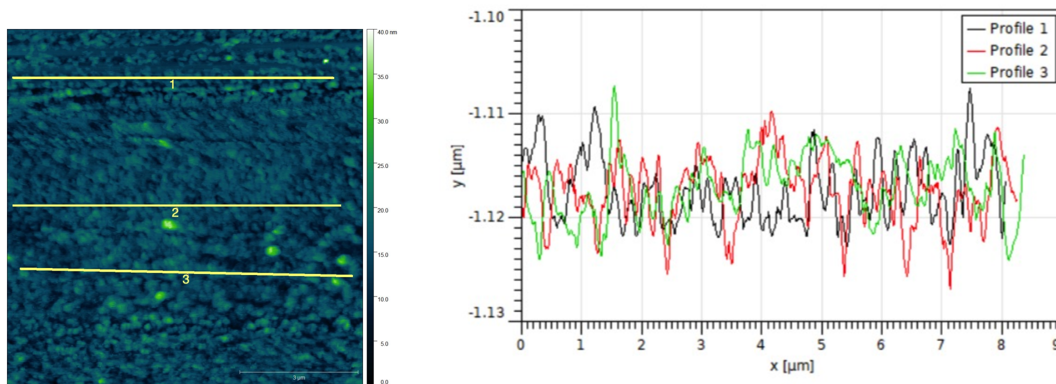

Figure 81: Data analysis of M373.

The extracted profile lines in figure 81 confirmed that the sample is homogenous with few irregularities on its surface. In this example, the roughness was 3.41 nm with irregularities averaging 10 nm high were observed. Using additional data from four different sites on the surface a roughness of 2.2 nm with irregularities averaging 17.5 nm high was calculated.However as noticed in the SEM micrographs of the surface, figure 77, the presence of droplets on the surface is still an issue for this sample.

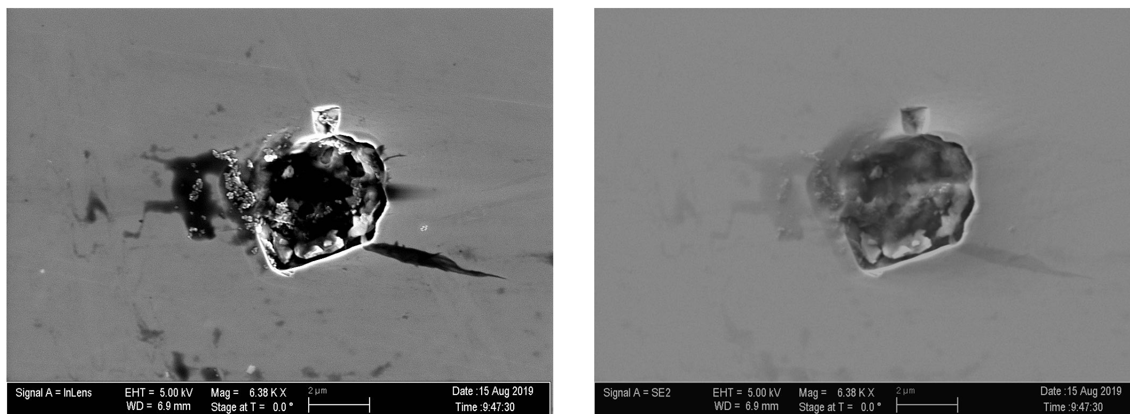

Figure 82: Hole droplet on the surface of M373.

Figure 82 depicts an example of a hole droplet present on the surface of M373. The shape and size of the hole droplet is similar to the one previously analyzed on the surface of M371 and M372. As the crystal continues to grow, some haphazard shapes are formed inside the hole, as already observed in the case of M371. There is also an issue of carbon contamination around the hole, represented by black areas.

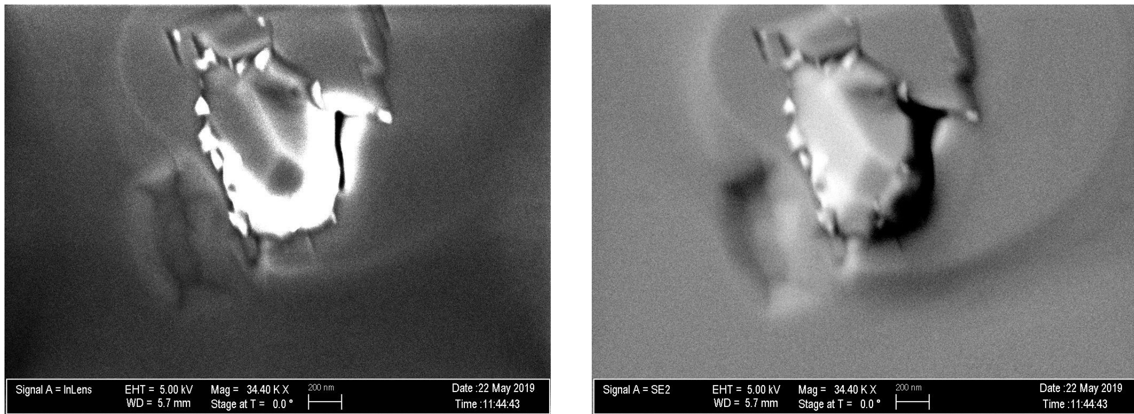

Figure 83: Hole and metallic droplet on the surface of M373.

Figure 83 shows an example of a metallic droplet present on the surface of M373. The length of this droplet is ca. 1 μm which is similar to the one previously determined in the cases of M371 and M372. However, the shape is spherical and differs from the previous metallic droplets analyzed. The impact of the droplet also produces topographical variations around it.

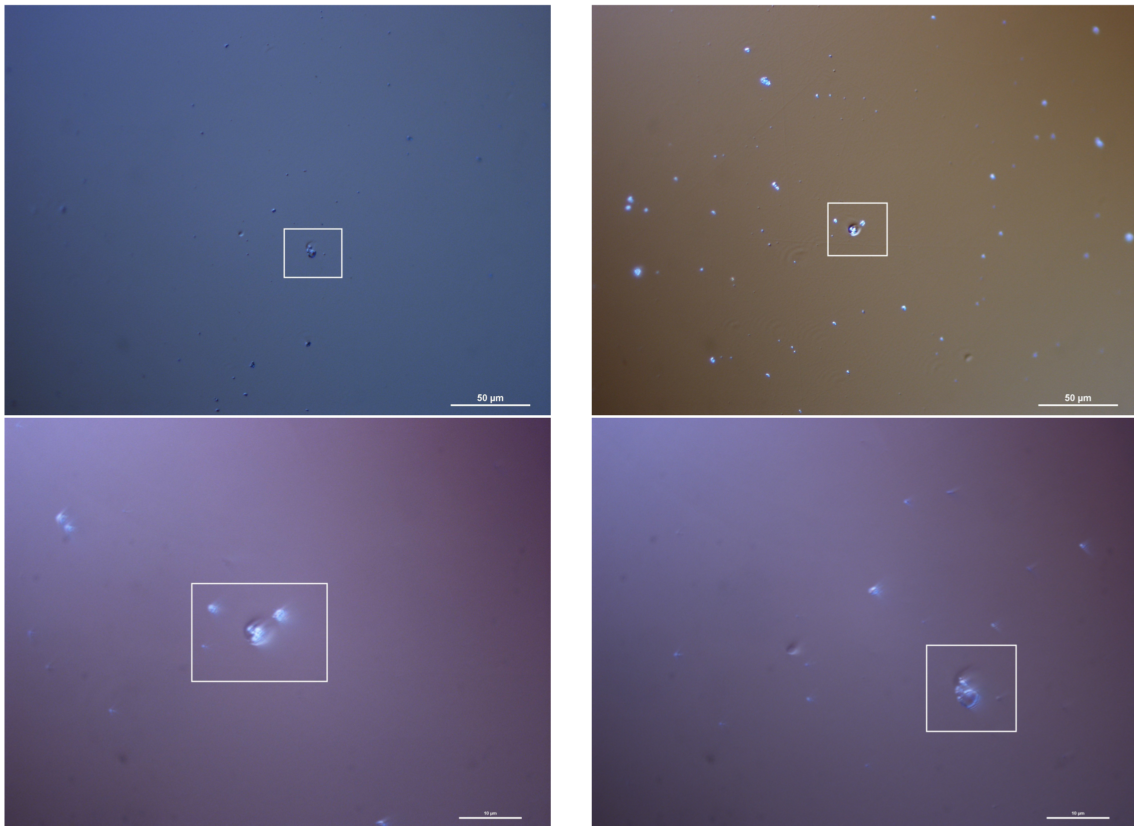

Figure 84: M373 droplets taken with the DIC Microscope.

In figure 84, the defects present on the surface of M373 are also spherical. However, a formation of cavities inside the material was noted. Despite the low magnification and resolution allowed by the DIC microscope, a supposition of hole droplet concerning these defects was made.

This section will now focus on the last sample of M series which is M374. This sample had the same oxide desorption temperature than M373. A slightly lower growth temperature and a slightly higher subsequent cooldown pressure were noted. The flux ratio V/III also decreased from a noticeable amount of 0.3.

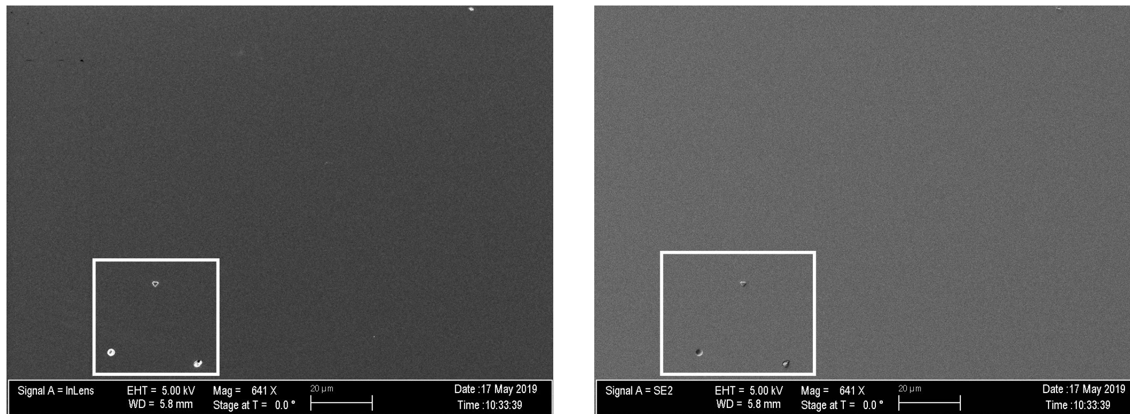

Figure 85: Background of M374 taken with the ZEISS NEON.

In figure 85, a smoother surface was observed despite the presence of droplets highlighted in white box. There are fewer droplets on the surface in comparison to M372 or M371 but slightly more than M373. There were no right angle defects, but metallic droplets are still an issue on this sample.

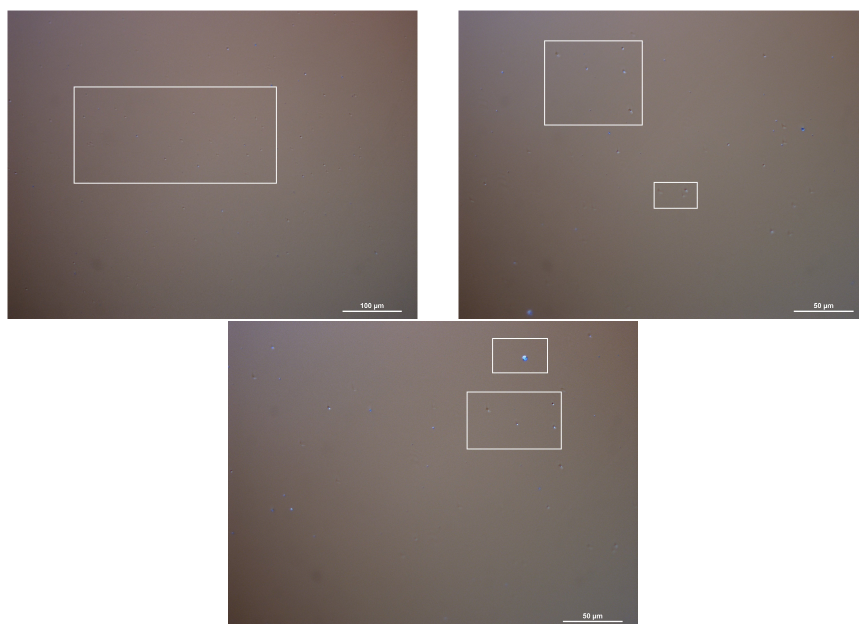

Figure 86: DIC micrograph of the M374 background.

In figure 86, shallow topographical variations, highlighted in white boxes, were noted. They are not metallic droplets due to their size difference. By averaging the density of defects on different sites on the sample a defect density of $2.82 \times 10^4\ cm^{-2}$ was calculated.

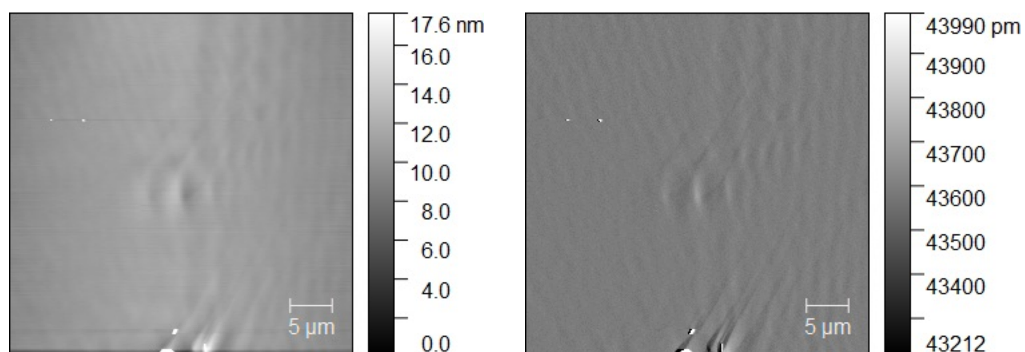

Figure 87: AFM micrograph of the M374 background.

As seen in figure 87, a homogenous surface condition of the background was noted. However, ripples on the surface were observed.

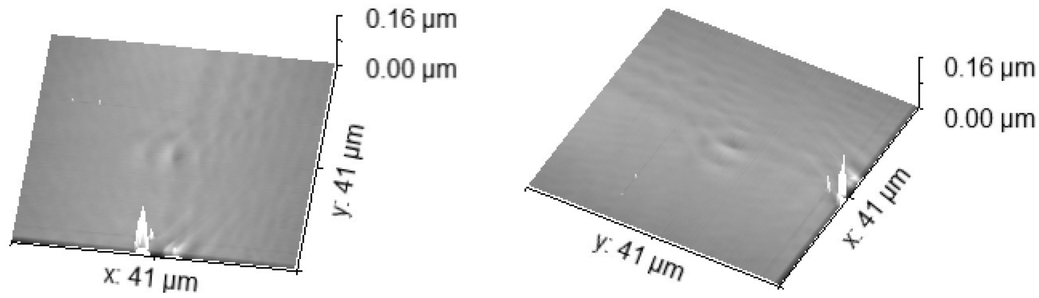

Figure 88: 3D representation of M374 Background.

From this 3D representation of the surface of M374 (fig.88), some shallow ripples on the surface which are attributed to an artifact of scanning, were depicted.

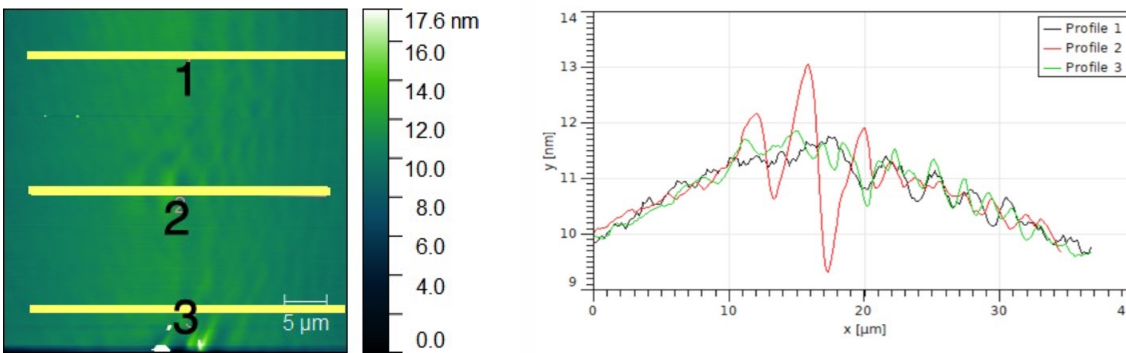

Figure 89: Data analysis of the M374 background.

From the extracted line profiles in figure 89, a bent surface was observed. However regarding the fact that the starting point of every graph is at the same height than the final point, one can conclude that this bending effect is an artifact of scanning. Composition wise, shallow topographical variations of 4nm height with a surface roughness (RMS) of 2.4nm was calculated.

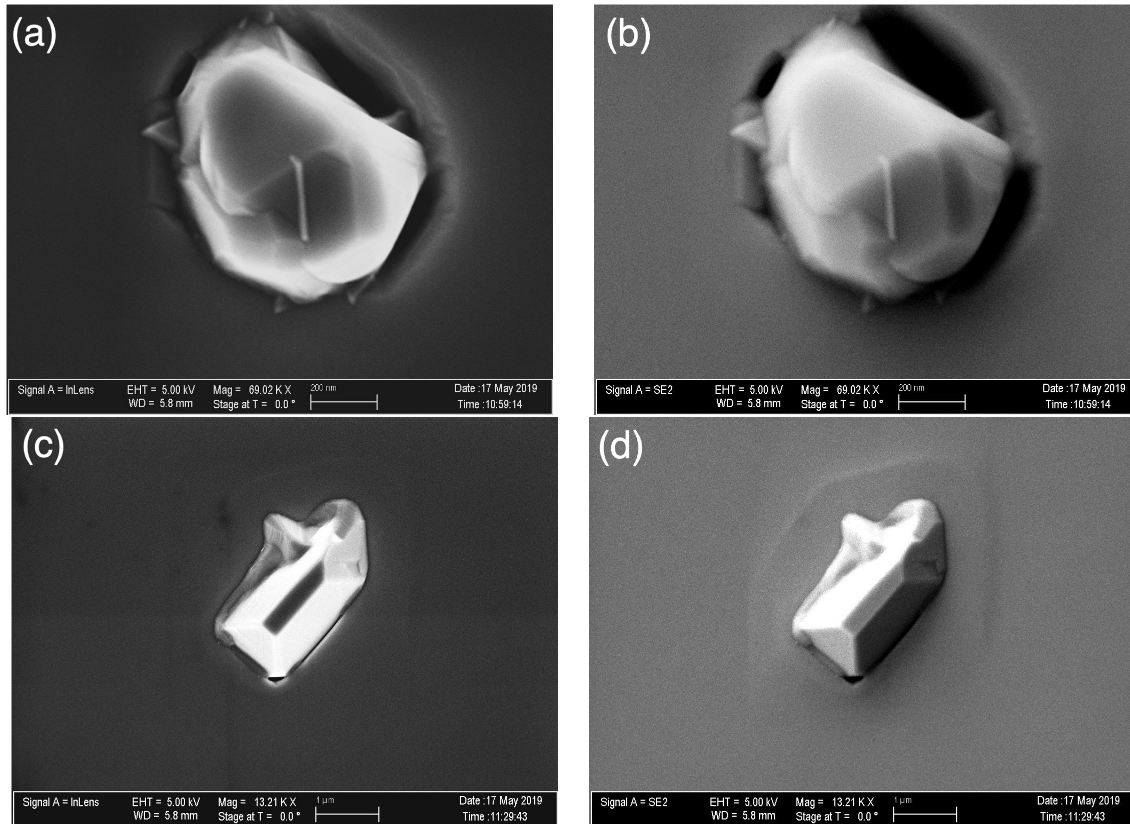

Figure 90: Metallic droplets in M374 taken with the ZEISS NEON.

In figure 90, two examples of metallic droplets encountered on the surface of M374 were depicted. In figure (a) and (b), the size of the metallic droplet is ca. 500 nm. In figure (c) and (d) the length of the droplet is roughly 1 μm. Similar sizes and shapes were observed on the previous samples of the M series. However a lower density of defects was noted in the case of M374.

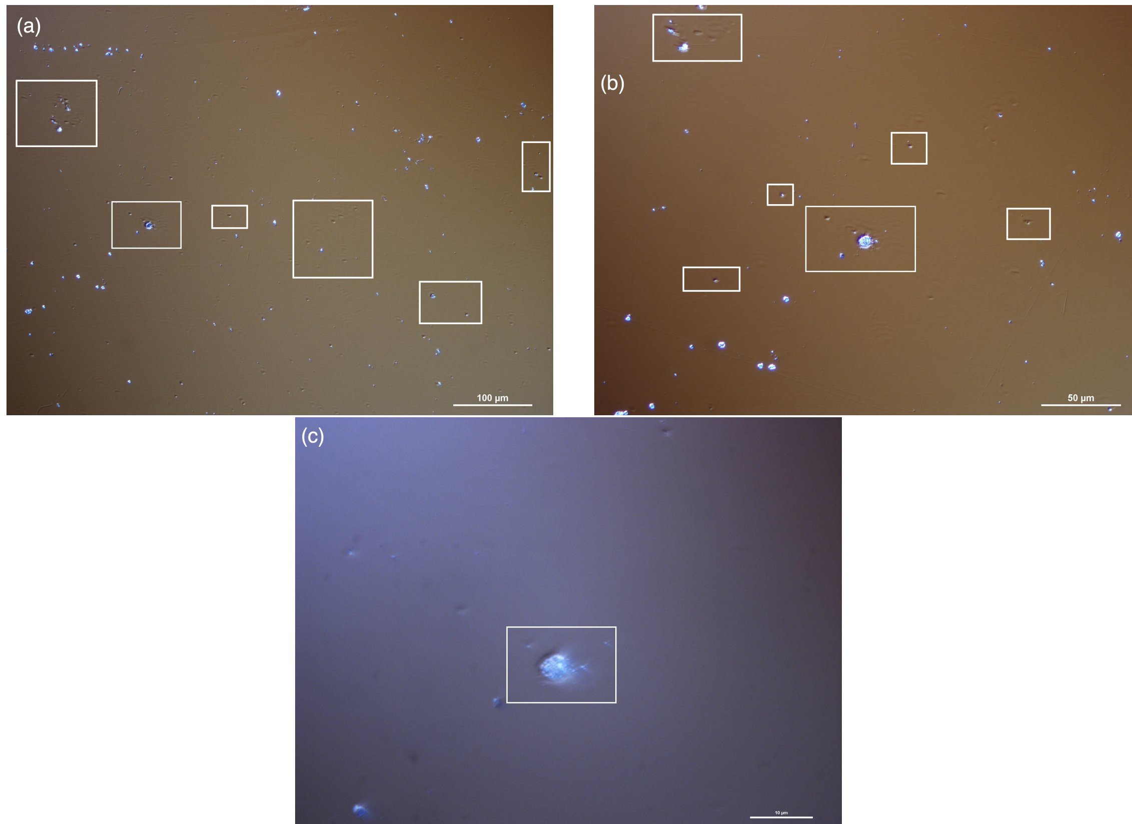

Figure 91: M374 metallic droplets taken with the DIC Microscope.

As seen in figure 91, a higher density of defects on the surface, highlighted in white boxes was observed on the surface of M374. Moreover in figure (c), a clear distinction between the droplet and the substrate was noted. This separation is due to the impact of the droplet when it hits the surface of the sample.

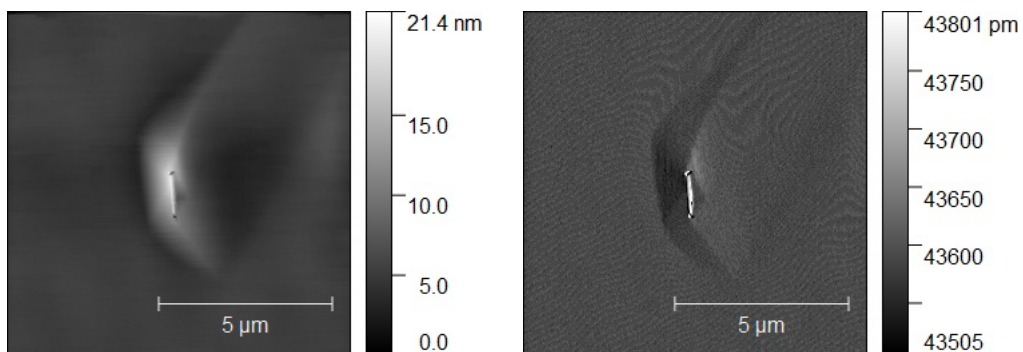

Figure 92: Metallic droplet on the surface of M374 taken with the AFM.

However, as seen in figure 92, the presence of a metallic droplet was noted. Formation of droplets is still a problem for M374. Although these types of defects are recurring on the surface of the sample, a shallow topographical variation was observed.

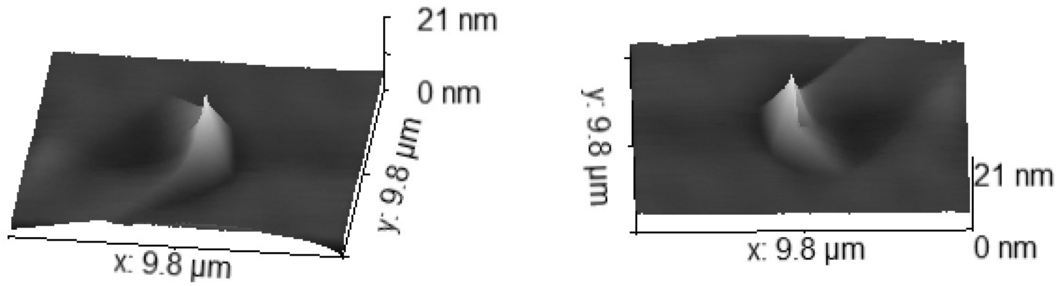

Figure 93: 3D representation of the metallic droplet on the surface of M374 imaged with an AFM.

From the 3D view of the M374 droplet in figure 93, a non significant height of these defects was discovered. The maximum height is 21 nm with a length which does not exceed 2 μm.

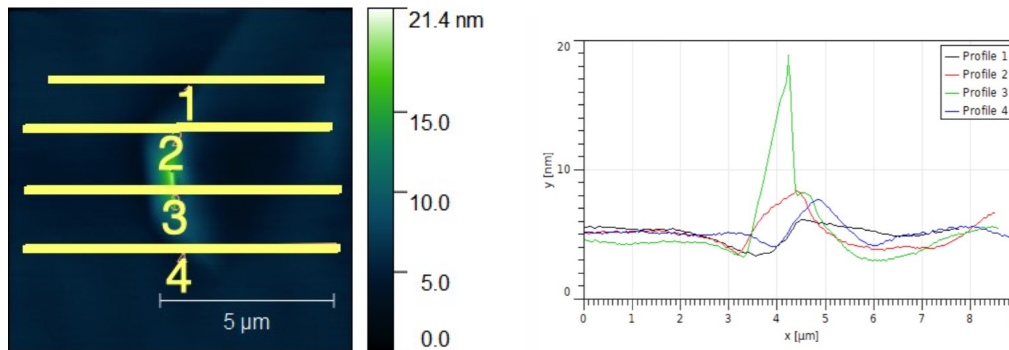

Figure 94: Data analysis of the metallic droplet on the surface of M374.

From the data analysis in figure 94, the maximum height for this droplet is 15 nm, taking into account the height if the overall background was analyzed. Using additional data of four similar defects an average roughness around the defects of 1.5 nm and an average height of the defects of 7 nm were obtained.

3.1 EBSD Analysis M374

The study concerning one of the samples of the M series will be described. Due to a wide variety of defects on the surface of M374, but with growth conditions close to M373, an analysis of M374 instead of M373 was conducted.

3.1.1 Metallic Droplet Analysis

First, the study will focus on case of a metallic droplet present on the surface of M374. Indeed because metallic droplets are still a recurring problem for semiconductors, further investigations about their orientation were conducted.

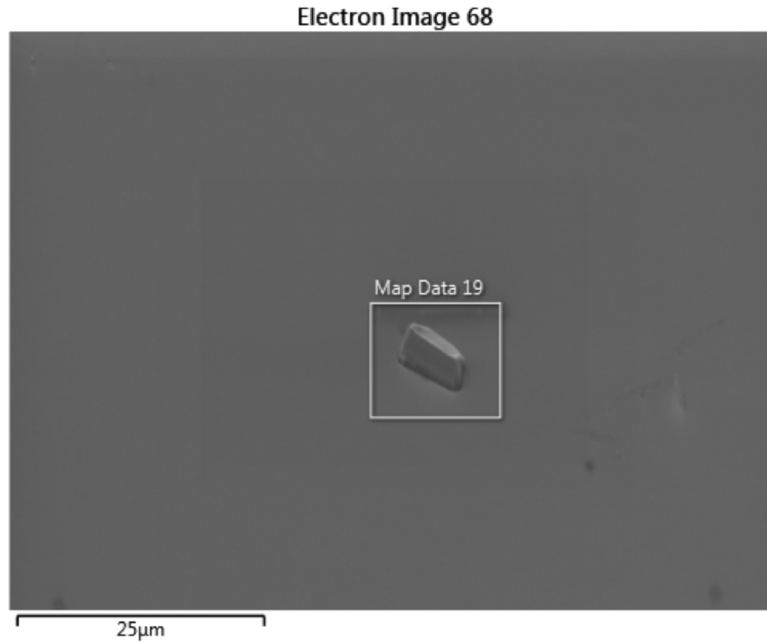

Figure 95: Secondary image of the metallic droplet in M374.

Figure 95 depicts the secondary image of the metallic droplet present on the surface of M374. This droplet was used for the EBSD analysis.

Quality of the scan

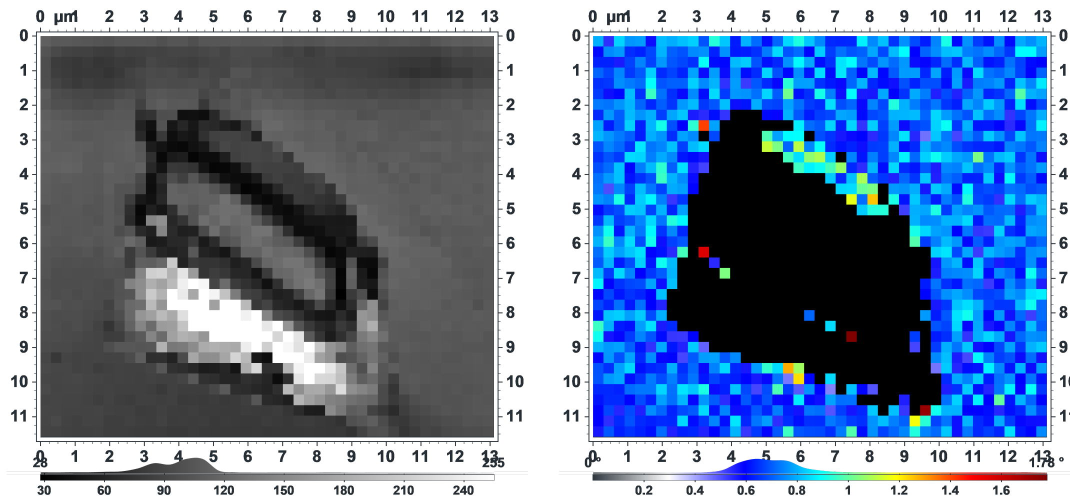

Figure 96: Band contrast map and Mean Angular Deviation (MAD) map of the metallic droplet taken on the surface of M374.

As seen in figure 96 the overall band contrast map is at a greyscale close to roughly

100 according to the horizontal greyscale bar under the band contrast map.This value is under the median greyscale level (122) which means that the scan in overall found more poorer fit spots than a good fit spots. Dark edges on the metallic droplet were noticed, which is due to a phenomenon called the shadow effect, and will be explained more carefully throughout this study. The dark areas on the band contrast map mean that the software did not get any information from the incoming electrons due to the geometry of the droplet. Indeed the incoming electrons on the edge were not reflected on the phosphor screen of the EBSD camera. Consequently, the software marked these areas as poor fit areas. Furthermore, the junction between the edge of the droplet and the background were marked in black and white respectively, also due to a shadow effect. Indeed due to the geometry of the metallic droplet, the incoming electrons hitting the edge of the metallic droplet were reflected and counted as electrons coming from the peripheral background.

Concerning the Mean Angular Deviation (MAD) map, a misfit angle of 0.6-0.7 degrees was deduced. This is reasonable due to the geometry of the metallic droplet scanned. This value is also close to an excellent fit [25], corresponding to a misfit angle of 0.5 degrees. Almost all the droplet is black, depicting the fact that the software did not find any phase to fit the model on these sites.

Orientation Study

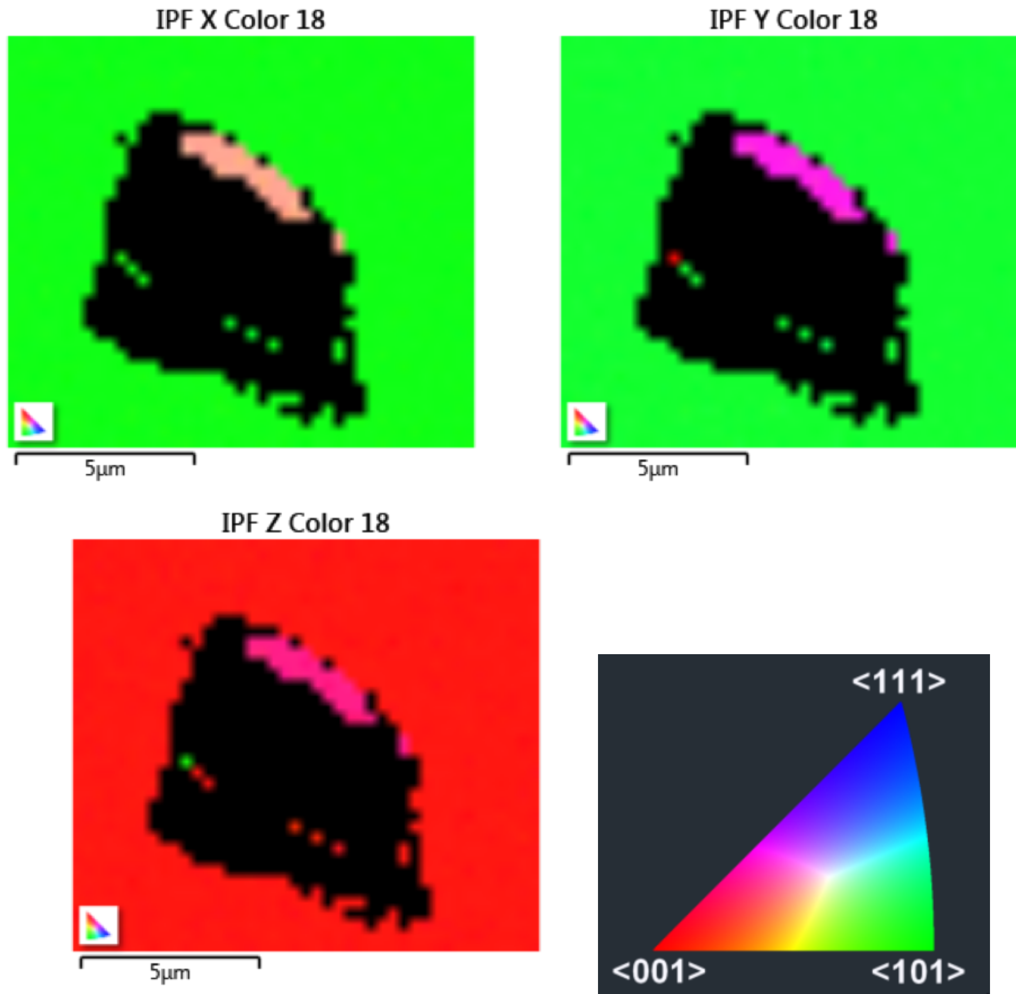

Figure 97: Inversion Pole Figure X,Y,Z map of the metallic droplet taken on the surface of M374.

Figure 97 depicts the inverse pole figure maps related to the three orientations X, Y, Z. On the X and Y inverse pole figure maps, an overall background in both cases pointing in the 101 direction was noticed. On the Y map, the surface of the metallic droplet, labelled in pink corresponds to an orientation in between the 111 and 001 direction. On the X map, the same area appears as light orange, corresponding to an orientation in between the 001 and 101 directions. On the IPF Z Map, the area on the metallic droplet is also pointing in a direction between the 111 and 101 direction, similar to the IPF Y map. However, the overall background is pointing in the 001 direction in this case.

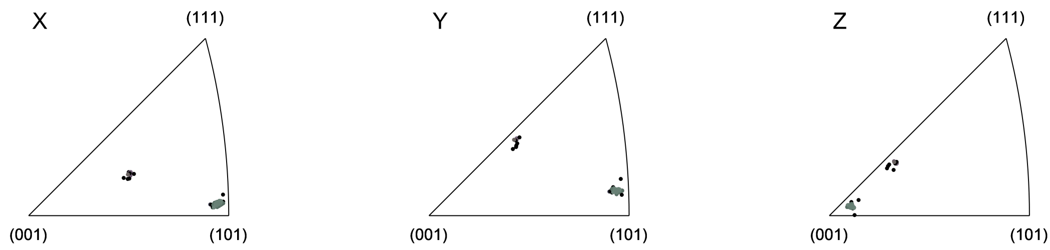

Figure 98: Inversion Pole Figure map with direct projection on the surface of M374.

Figure 98 depicts accurate information of the X,Y and Z orientations of the metallic droplet. From the previous figure, figure 97, an overall background pointing in the 101 direction concerning the X direction was noted. Consequently, in the inversion pole figure map along the X direction above, the group of points near the 101 direction correspond to the background and the other one is the surface of the metallic droplet, pointing in a direction between the 101 and 001, 101 and 001 and 111 and 001 directions.

Using the same reasoning for the Y map, the group of points near the 101 direction corresponds to the background. The other one refers to the surface of the metallic droplet, pointing a direction between the 001 and 111 directions. Finally concerning the Z-map, the group of points near the 001 direction is the background and the other one is the surface of the metallic droplet, which in this case points in a direction slightly off the 001 direction as noted in figure 98.

3.1.2 Electron Backscattered Analysis of a Hole Droplet

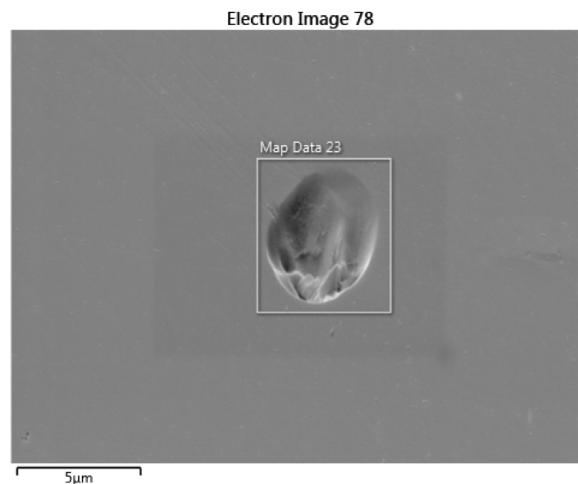

Figure 99: Secondary image of a hole droplet on the surface of M374 used for the EBSD analysis.

Figure 99 depicts an example of a hole droplet present on the surface of M374. As seen inside the hole the matter contains many irregularities. A similar study involving another example of hole droplet can be found in appendix A.

Quality of the scan

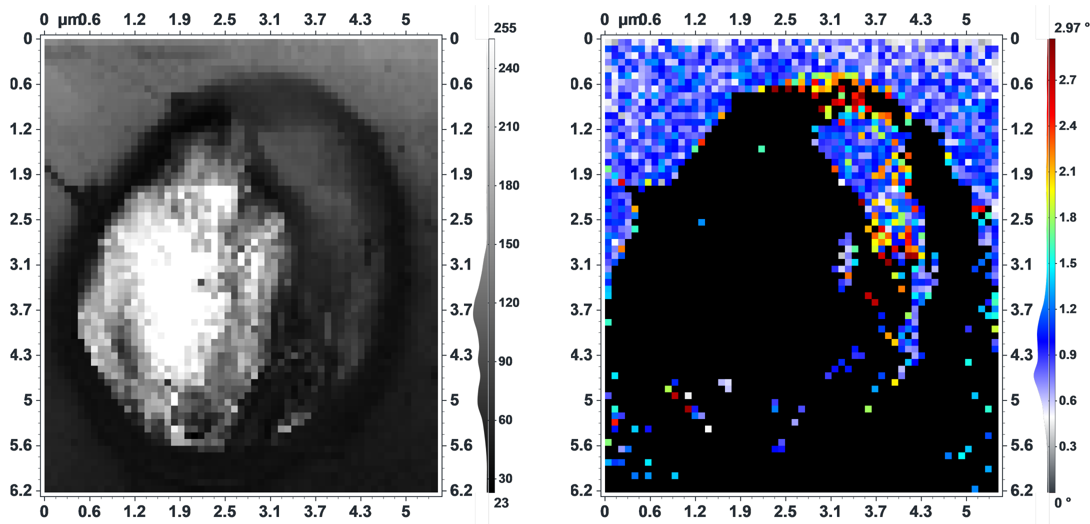

Figure 100: Mean Angular Deviation (MAD) map and band contrast map of the hole droplet taken on the surface of M374.

In figure 100, as seen from the band contrast vertical greyscale bar, two different greyscale values were obtained. One of them, corresponding to the background around the hole droplet, is at a greyscale of 110, which is close to the median greyscale value of 122. The other peak at 60 corresponds to the dark edges around the droplet. Indeed as seen previously from the other example of hole droplets, the edges of the defect suffer from shadow effects. However, the greyscale value corresponding to the background at the bottom of the hole droplet appears as black whereas the top one appears at a reasonable greyscale value. This effect is due to carbon contamination build up because of the duration of the analysis (10 to 15 hours).Concerning the Mean Angular Deviation (MAD) map, an average misfit angle of 0.6-0.7 degrees was obtained, close to the optimum misfit angle of 0.5 degrees [25]. For the same reasons that were noticed for the previous example of a hole droplet, one can conclude that the band contrast and the MAD map confirm that the scan is reliable.

Orientation Study

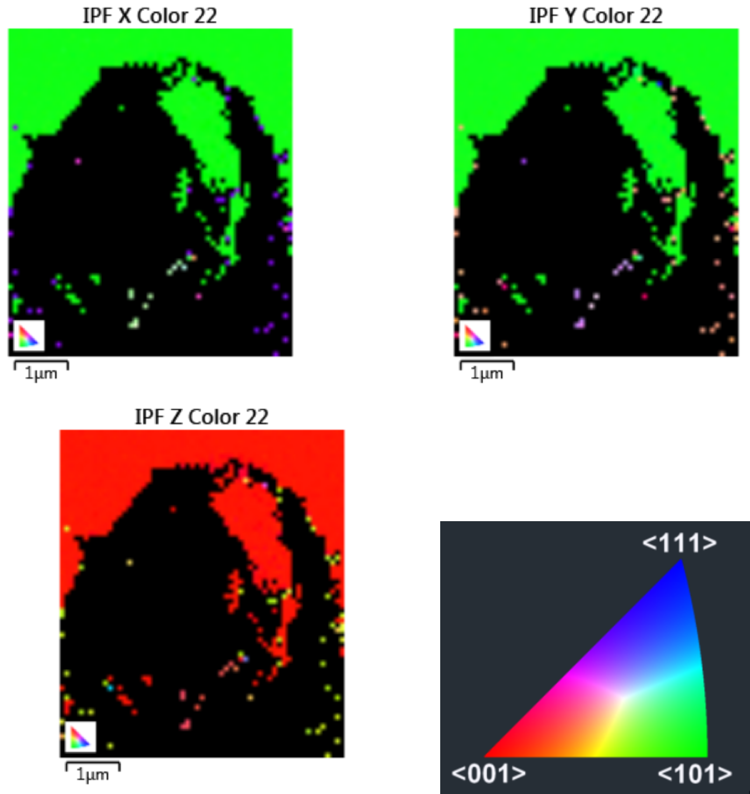

Figure 101: Inversion Pole Figure X,Y,Z of the hole droplet.

Figure 101 presents the inverse pole figure maps related to the three orientations X, Y, Z, which give information about the orientation of the hole droplet present on the surface of M374. On the X and Y Inverse Pole Figure maps, the overall background in both cases is pointing in the 101 direction. Concerning the IPF in the Z direction, it is pointing in the 011 direction.

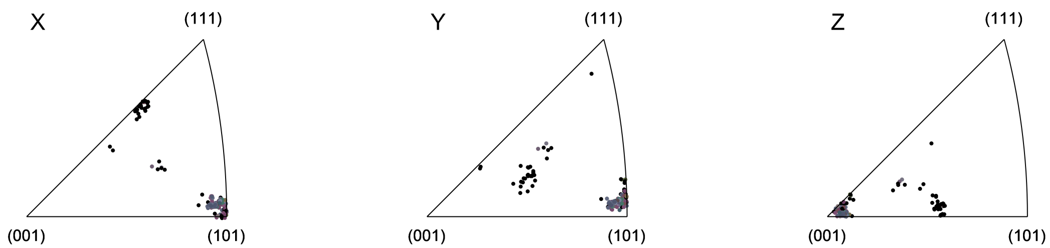

Figure 102: Inversion Pole Figure map with direct projection of the hole droplet analysis.

Figure 102 presents accurate information of the X,Y,Z orientations of the hole droplet.From the previous figure, figure 101, an overall background concerning the X direction pointed in the 101 direction. Consequently in the inversion pole figure map along the X direction,

the group of points near the 101 direction correspond to the background. The points in between the 001 and 111 directions are the irregularities inside the hole. A common direction along the line between the 111 and 001 direction except some exceptions was noted.

Using the same reasoning for the Y map, the group of points near the 101 direction correspond to the background. The other points at the center of the IPF map are the random orientations detected inside the hole. Finally concerning the Z map, the group of points located between the 001 and 101 directions are the irregularities inside the hole. As previously seen, the background is facing in the 001 direction.

3.2 Conclusion

Name	Defect Density (cm^{-2})	RMS(nm)	Height(nm)	Type of defects	Frequency of occurrence
M371	5.00 x 10^4	0.4	4.4	Pyramidal	Often
M371	5.00 x 10^4	X	X	Metallic Droplet	Often
M371	5.00 x 10^4	14.6	116.3	Irregularities	Often
M372	4.19 x 10^4	5.3	26.8	Irregularities	Always
M373	2.58 x 10^4	X	X	Metallic Droplets	Rare
M373	2.58 x 10^4	X	X	Tiny Lines	Often
M373	2.58 x 10^4	2.2	17.5	Irregularities	Often
M374	2.82 x 10^4	X	X	Metallic Droplets	Really Often
M374	2.82 x 10^4	1.5	7	Irregularities	Often

Table 4: M series data table.

The table above summarizes the study concerning the four different samples of the M series. If one had to choose the best sample, one would choose M373 despite M374 also having some interesting advantages. Indeed a lower density of defects with a low amount droplets on the surface of M373 was observed on its surface. However, a slightly higher roughness with a higher average height of defects present on the surface of M373 was calculated in comparison to M374. In order to find the perfect configuration, a study analyzing a sample with growth conditions in between M374 and M373 would be best to obtain a sample with a very low roughness and density of defects.

4 Y series TPV Interband Cascade Devices

The concept of interband cascade devices was proposed by Rui Q. Yang in 1994. It was first developped for a laser application.[36] The main idea is to incorporate a type-II heterostructure similar to those used in interband resonant tunneling diodes to facilitate the possibility of cascade lasers that use interband transitions for photon generation. Interband cascade devices are fabricated from semiconductor heterostructures grown using molecular beam epitaxy (MBE), previously explained in the background section. The materials used in the structure are InAs, GaSb, AlSb, and related alloys. The three binary materials are very closely lattice-matched with lattice parameters close to 6.1 Å. Thus, these materials can be incorporated together in the same heterostructure without introducing a significant amount of strain. The amount of strain present in the semiconductor could result in the formation of oval defects called hillocks. A study of oval defects on AlGaAs/InGaAs/GaAs and InGaAs/GaAs structures was conducted in 1999.[17] Two groups of oval defects were noticed, defects without a core and defects with a core. A link between the gallium effusion cell temperature and the oval defect density was noted.

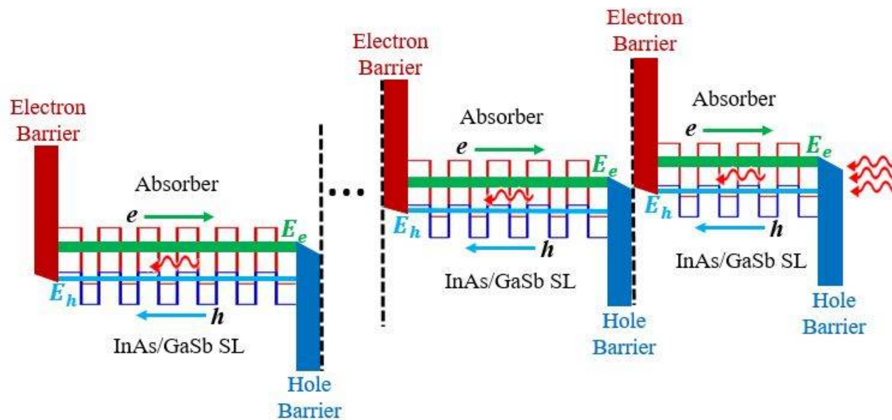

Figure 103: Band diagram of a three stages in a typical interband cascade photovoltaic prototype [31].

In this chapter, several interband cascade photovoltaic devices are studied.As seen in figure 103, the cascade stage is divided into a superlattice absorber, an electron barrier, and a hole barrier. The groups of quantum wells that constitute each region are indicated. The superlattice absorber has a thickness of 130 nm. The electron and hole barrier have a thickness of 25 nm and 47 nm respectively. The advantages of this type of photovoltaic prototype in comparison to conventional ones are :

- Each stage can absorb a different wavelength by changing the thickness of the different quantum wells.
- Due to the high number of absorber layers, more light intensity is collected,

- The wavelength range of the absorbers is in the mid-infrared, which optimizes the device for blackbody sources at a lower temperature (1000 K) in comparison to regular photovoltaic devices that absorb light emitted bythe sun (5800 K).

However, due to the cascading process several photons are needed to create one electron. Indeed the same amount of photons than the number of stages grown on the substrate is required. This characteristic seems to be a disadvantage but regarding the fact that more light intensity is absorbed, due to a thick superlattice absorber of 130 nm per stage, a photovoltaic device with better efficiencies is made using this principle of interband cascade.

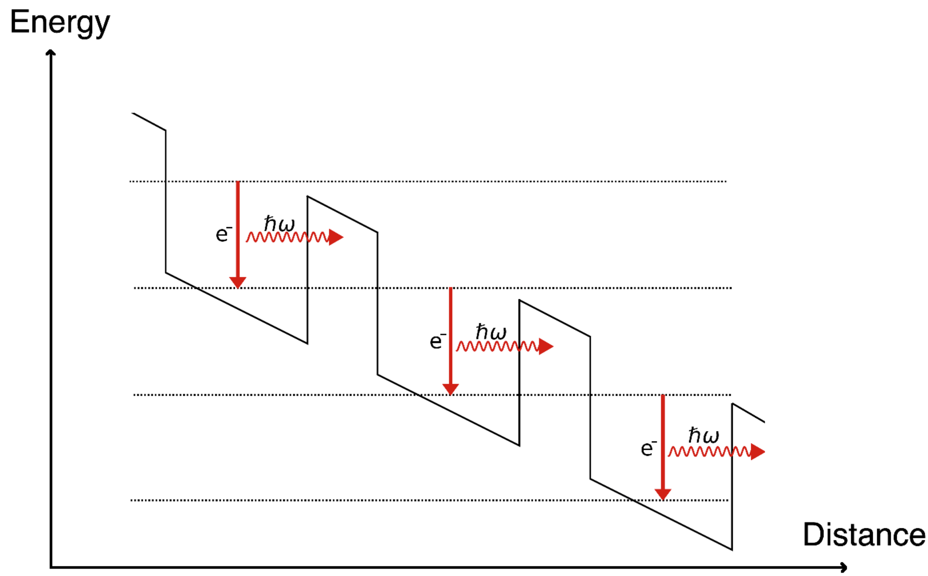

Figure 104: Cascade diagram process in an quantum cascade device.

Figure 104 demonstrates the principle of cascading and why a high number of stages is important to get efficient devices. A quantum well corresponds here to one stage in a quantum cascade device. When an electron makes a transition from a higher band to a lower band, a photon is emitted. Once an electron has undergone an intersubband transition (higher band to lower band) the electron tunnels through the barrier between the two quantum wells, called the tunneling effect. Once it arrives in the next quantum well it is actually on the higher band of this quantum well. Therefore another intersubband transition can occur, creating another photon. This is the reason why this type of device is called a cascade device.

Concerning this study, the behavior of an interband cascade photovoltaic devices will be analyzed. The concept is the same except the fact that it is several photons that produces one electron. Also, the transition is between the conduction band of InAs and the valence band of GaSb in the absorber. To maximize the efficiency of this photovoltaic

device, one needs to make sure that the growth conditions are optimal to minimize the defect density. This section will focus on three interband cascade photovoltaic prototypes. Two of them Y064V and Y067V are 8-stages interband cascade devices and the last one Y074V is a 15-stages interband cascade device.

This study will focus on the major growth variations :

- The effect of an Antimony soak during interrupts in the growth process
- Increasing the number of stages and the consequences on the defect density

4.1 Y064V, 8 Stages without Antimony Soak

First the study of Y064V, an 8-stage Interband Cascade Device without an Antimony soak will be conducted.

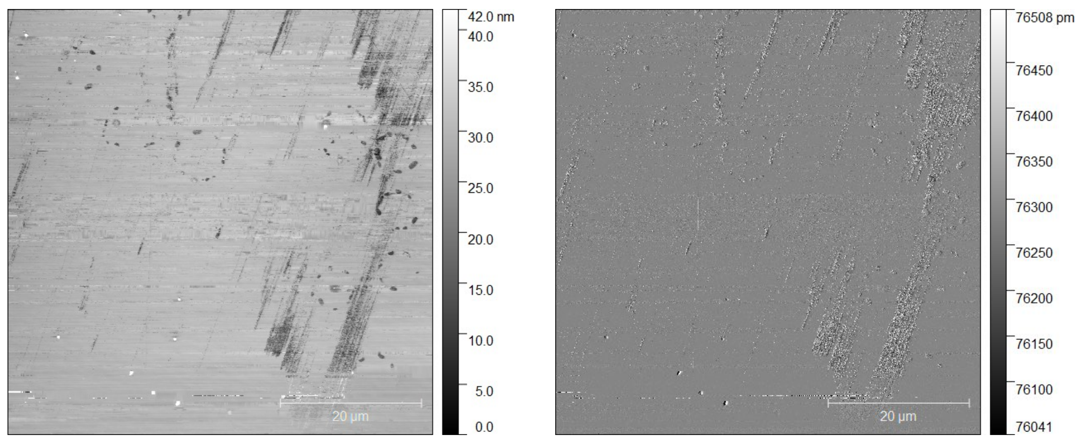

Figure 105: AFM height channel image and amplitude image of the background of Y064V.

Figure 105 shows the AFM micrographs of the background of Y064V. A scanning area of 60 μm by 60 μm was chosen here. The overall background was considered smooth with black marks on the surface due to contamination.

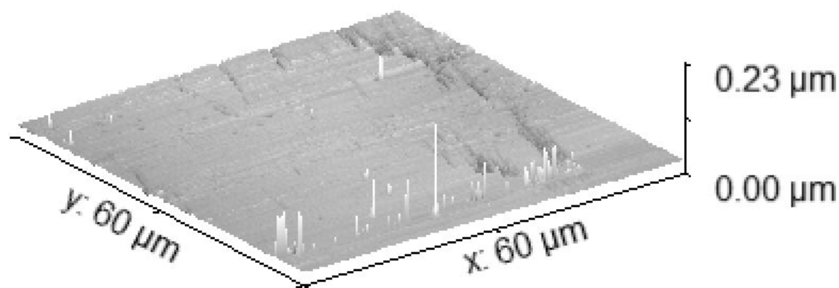

Figure 106: 3D representation of the background of Y064V.

Figure 106 displays the 3D representation of the surface of Y064V. A smooth surface condition with very little topographical variations was noted.

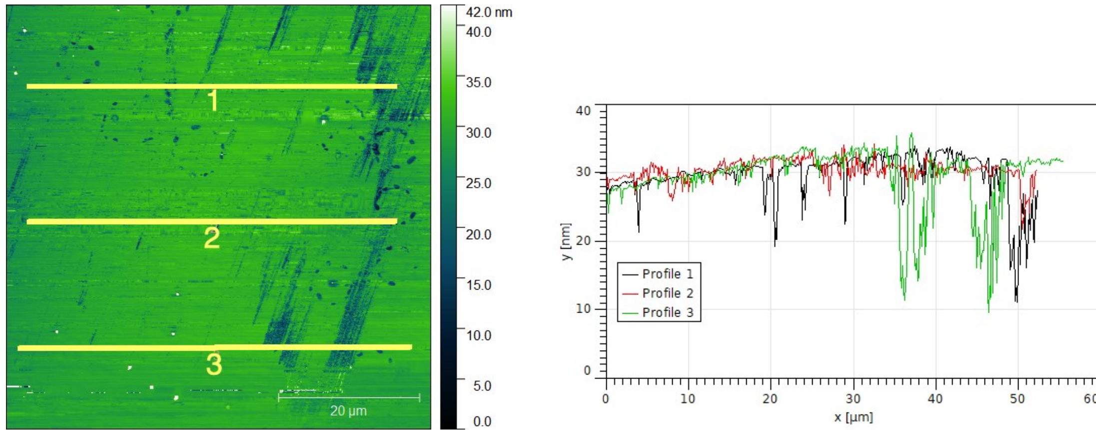

Figure 107: Data Analysis of the Background of Y064V.

As seen in figure 107, the data analysis of the background of Y064V is presented. The surface is smooth with topographical variations which are the carbon contamination marks of 20 nm height. Composition wise, using additional data from different sites on the surface an average RMS roughness of 2.7 nm was obtained with topographical irregularities on the surface that have a height of 9 nm.

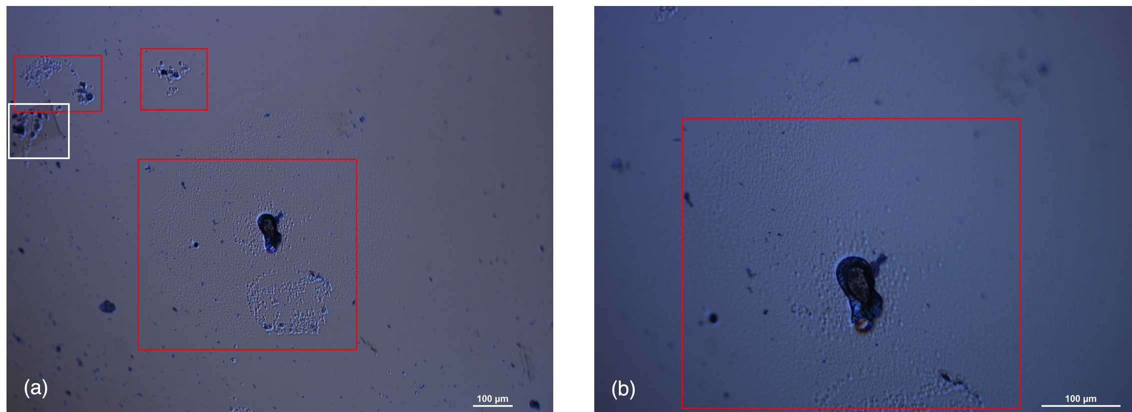

Figure 108: DIC images at 10x in figure (a) and at 20x in figure (b) of the background of Y064V

As displayed in figure 108, a smooth background with irregularities on the surface highlighted in red boxes were noted. Those defects are called hillocks and are a recurring type of defects encountered on the surface of interband cascade devices. The rectangle in figure (a), highlighted in white box is carbon contamination due to an EBSD analysis on the surface of Y064V.

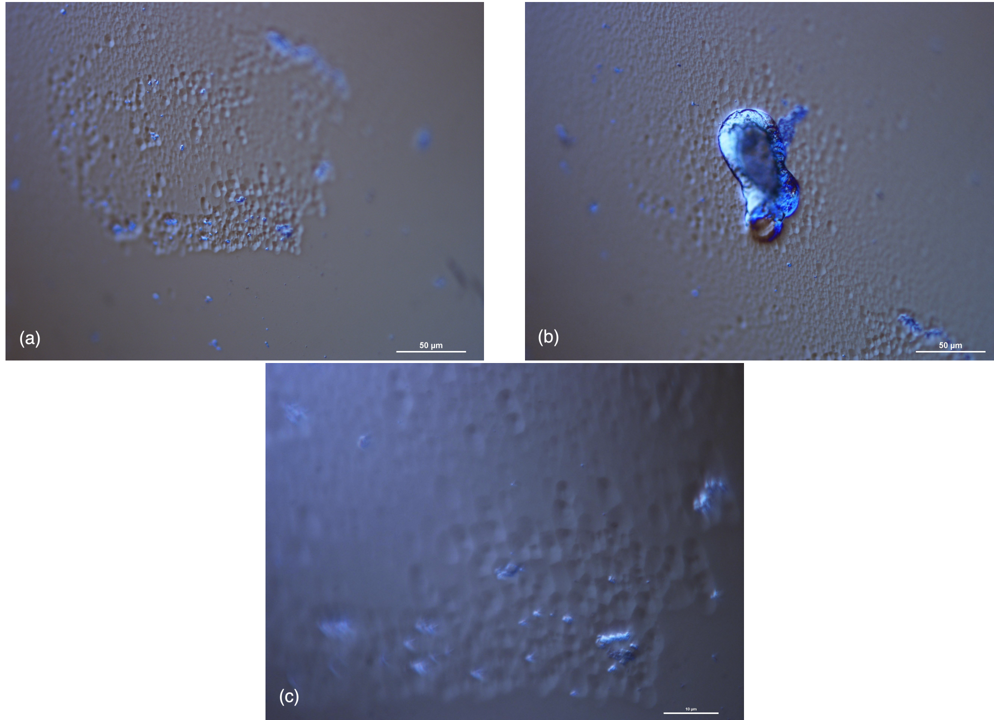

Figure 109: DIC micrographs (a,b) and (c) at 100x of the hillocks that we can encounter on the surface of Y064V.

Using high magnification in figure 109, a high concentration of hillocks on the surface of Y064V was observed. By calculating the density of defects on various sites including only hillocks we obtain a density of defects of $118 \times 10^4\ cm^{-2}$. However, this value is not always representative of the surface condition because this calculation was done under an area with a high concentration of hillocks. Indeed the formation of hillocks on the surface of Y064V is not homogenous, but found in big groups in certain sites. However, as noticed in figure 109, some wide areas containing no hillocks were also noted.

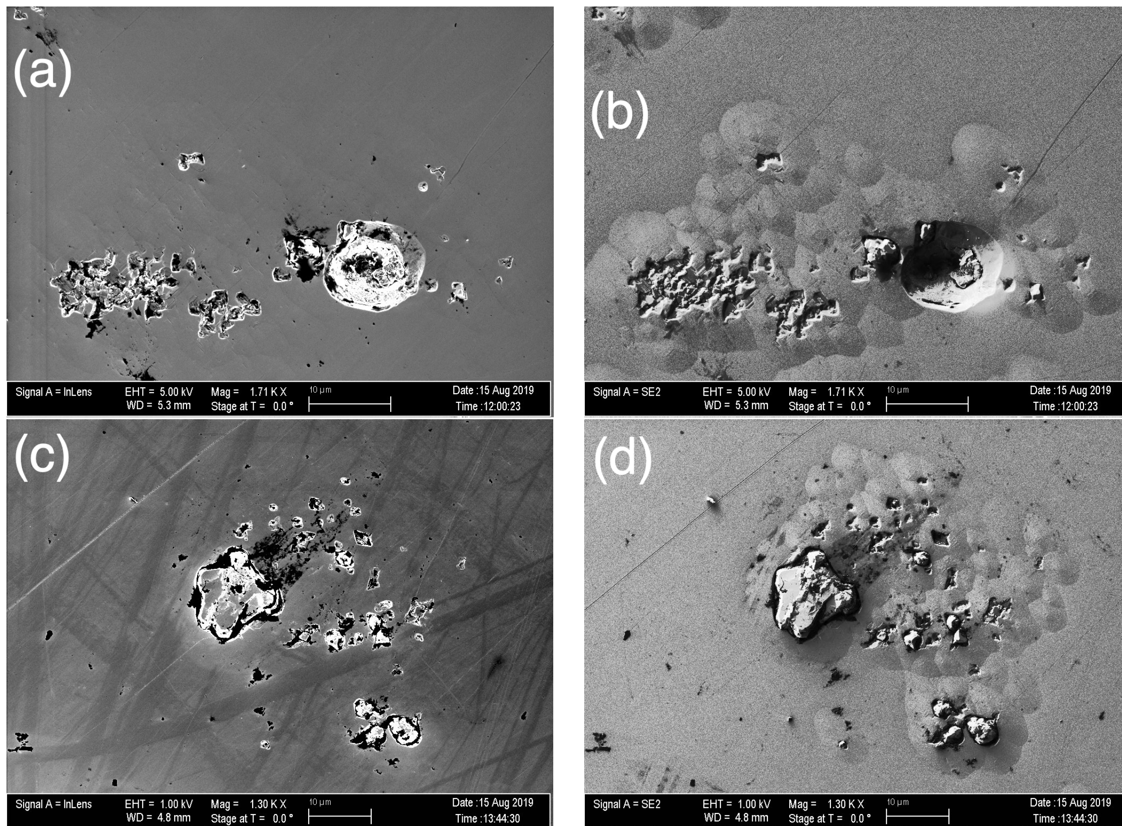

Figure 110: SEM hillock images that we encounter on the surface of Y064V, taken with the ZEISS Neon 40 EsB at low magnification (1kX).

Figure 110 depicts two examples of hillocks images taken with the SEM. The presence of metallic droplets or hole droplets on the surface of the hillocks was noted. Figure (a) and (b) show the presence of a hole droplet surrounded by hillocks whereas figure (c) and (d) display the presence of a metallic droplet surrounded by hillocks. These two examples depict how hillocks are formed in island shapes.

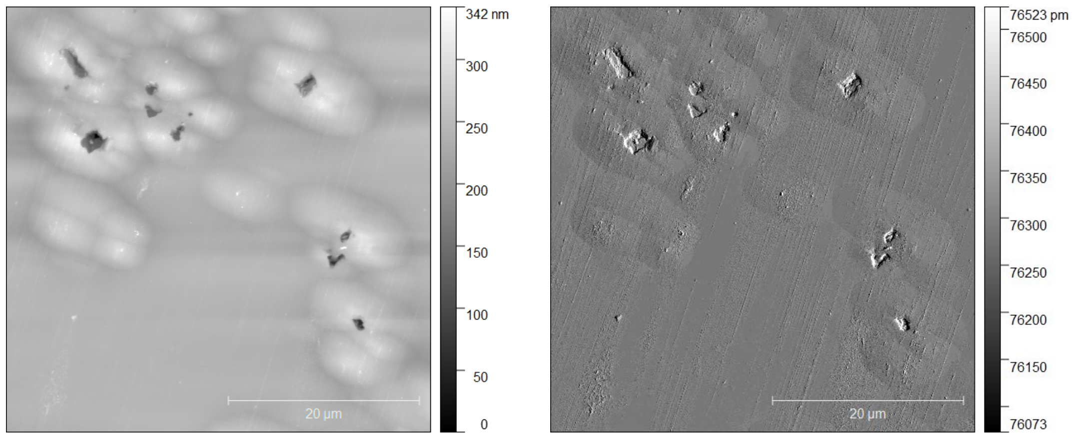

Figure 111: AFM height channel image and amplitude image on a massive hillock area on the surface of Y064V.

Figure 111 shows an example of hillocks under the AFM microscope.

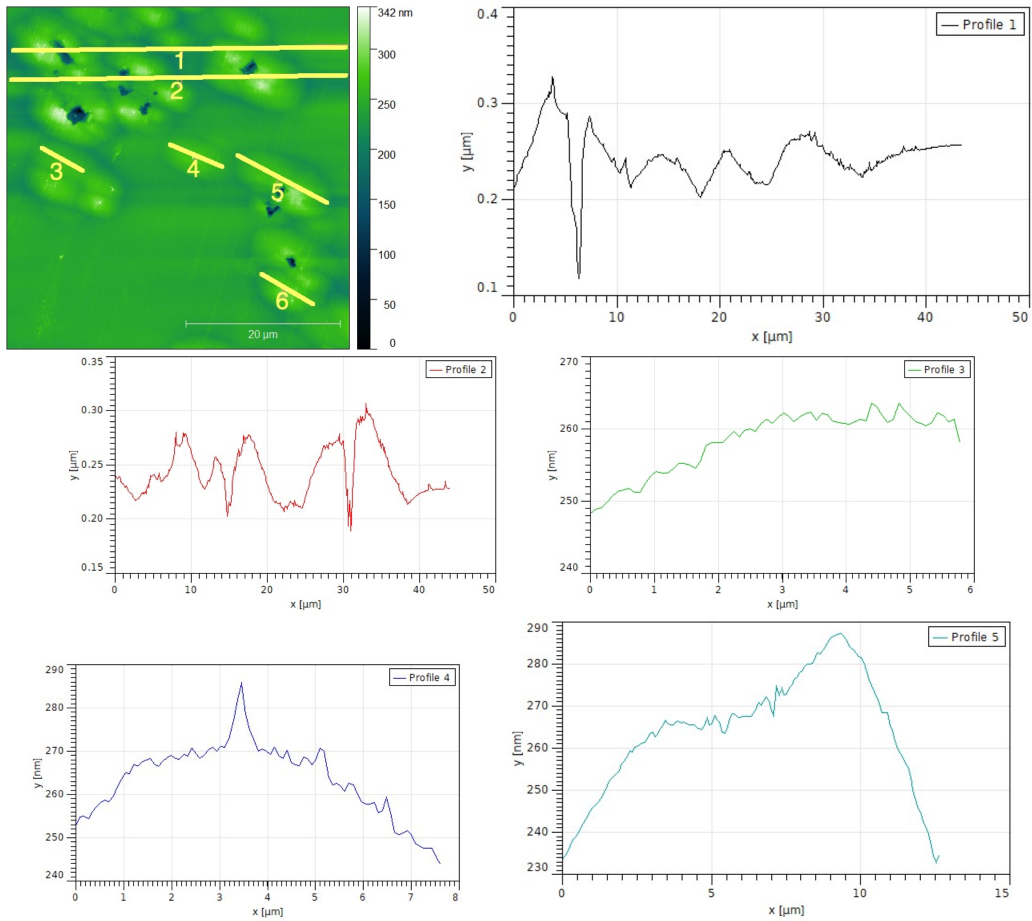

Figure 112: Data analysis of AFM height on a massive hillock area on the surface of Y064V.

In the different line profiles extracted from the hillocks in figure 112, a hillock height oscillating between 50 to 100 nm was calculated. However, drawing any conclusion for now is difficult because the magnification used is too low.

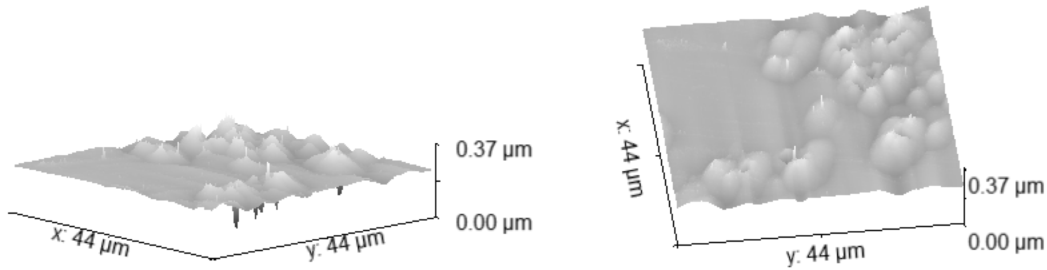

Figure 113: 3D representation on a massive Hillock area on the surface of Y064V

Figure 113 diplays a 3D representation of the hillocks present on the surface of Y064V. Using this representation, a high topographical variation was observed.

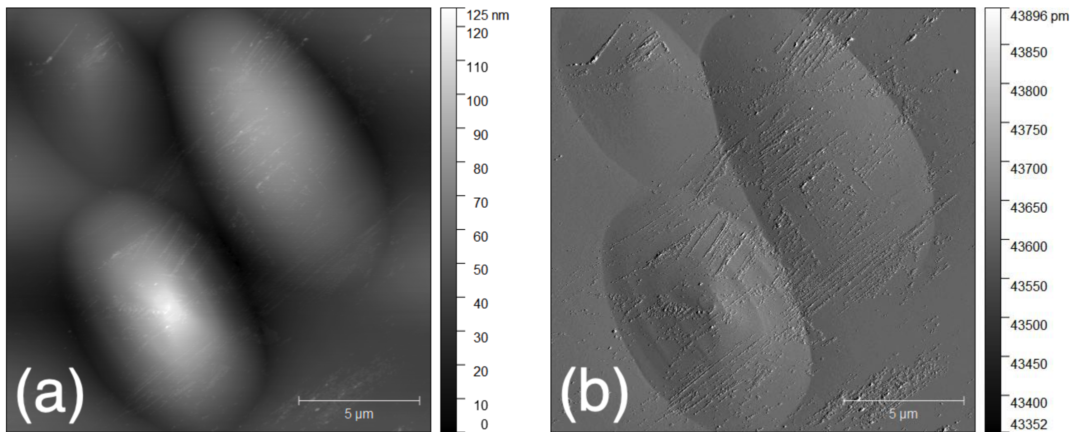

Figure 114: Figure (a) AFM height channel and Figure (b) amplitude channel of a zoomed hillock area on the surface of Y064V at high magnification.

As seen in figure 114, in figure (b) a surface of the hillocks containing irregularities was observed. These irregularities are due to contamination and not features on the surface of the hillocks.

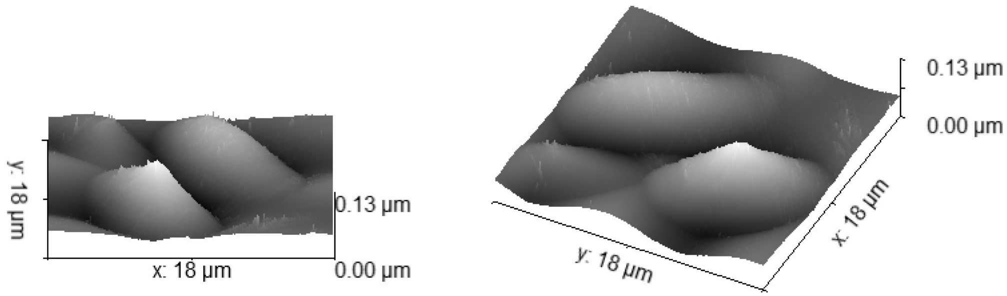

Figure 115: 3D representation of a zoomed hillock area on the surface of Y064V.

Figure 115 depicts the 3D representation of hillocks present on the surface of Y064V. One hillock has a triangular shape along the Z-axis which is not the case for the two other hillocks.

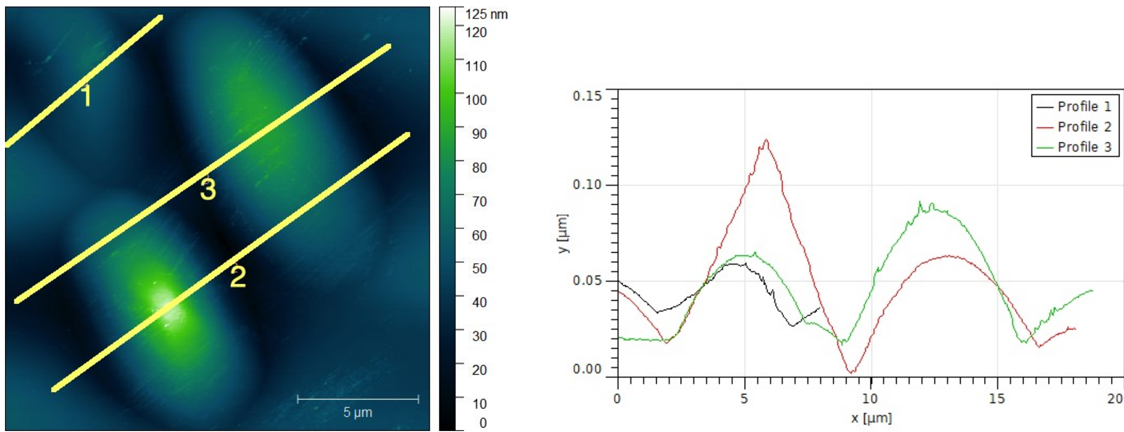

Figure 116: Data analysis of a zoomed hillock area on the surface of Y064V.

The hillock with a triangular shape, corresponding to profile 1, in figure 116 has a maximum height of 130 nm. The second one, corresponding to profile 2, has a maximum height of 60 nm and the last one, corresponding to profile 3, is shallow and has a maximum height of 20 nm. By comparing these values with those of 38 other hillocks, an average height of 65.8 nm and an overall roughness around the hillock of 18 nm was obtained.

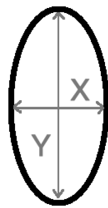

Figure 117: Schematic to define the X-axis and the Y-axis in the hillock measurement.

The X-axis is the horizontal axis, in figure 117, or the smallest diameter of the oval and the Y-axis is the vertical axis or the biggest diameter of the oval. By measuring both distances on 24 Hillock images an average X length of 5.5 μm and an average Y length of 9.5 μm was obtained.

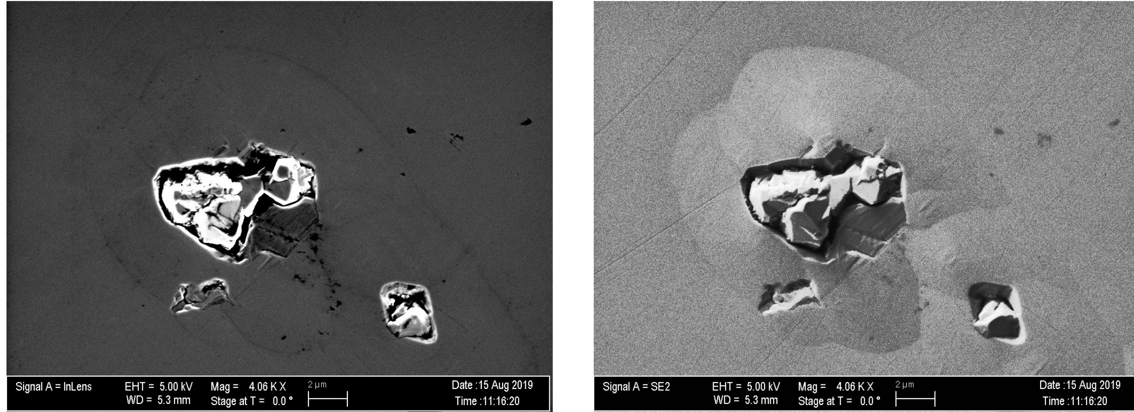

Figure 118: SEM hillock images that we encounter on the surface of Y064V, taken with the ZEISS Neon 40 EsB at higher magnification (4kX).

In figure 118 an example of a metallic droplet is seen at 4 kX with the presence of hillocks around it was depicted. A smooth surface condition on the hillock was noticed except at the summit where ripples were located.

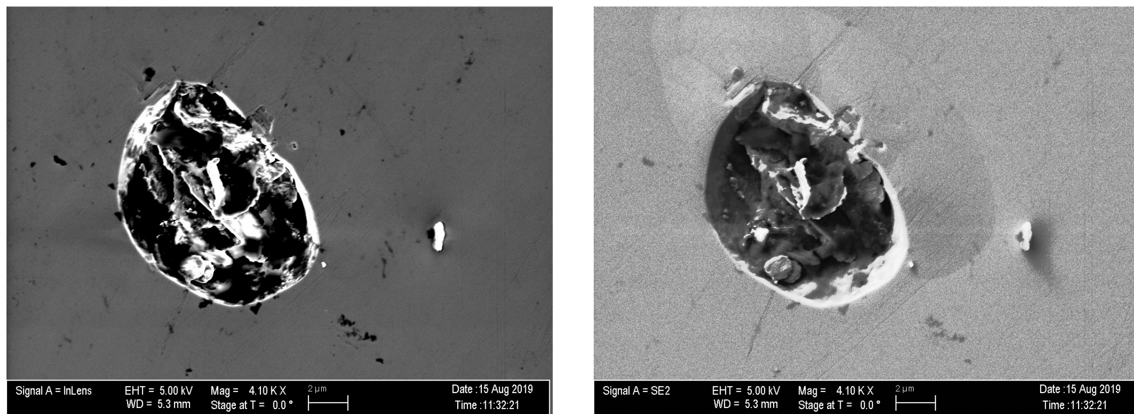

Figure 119: Hole droplet images that we encounter on the surface of Y064V taken with the ZEISS Neon 40 EsB.

Figure 119 shows the presence of a hole droplet on the surface of a hillock. Some ripples around the edge if the hole droplets were observed. The size of the hillock in figure 119 and 118 are similar to the average length determined using the AFM.

4.2 Y067V, 8 Stages with Antimony Soaks

This section will now focus on another sample similar to Y064V. This sample is also an 8-stages interband cascade device.However, this Y067V was grown under modified conditions. This sample had an antimony soak during growth of the InAs/GaSb absorber layers. After the growth of an InAs layer, the surface was exposed to a flux of Sb atoms for 4 seconds before continuing with the growth of a subsequent GaSb layer. These Antimony soaks are thought to improve the abruptness of the InAs/GaSb interfaces.

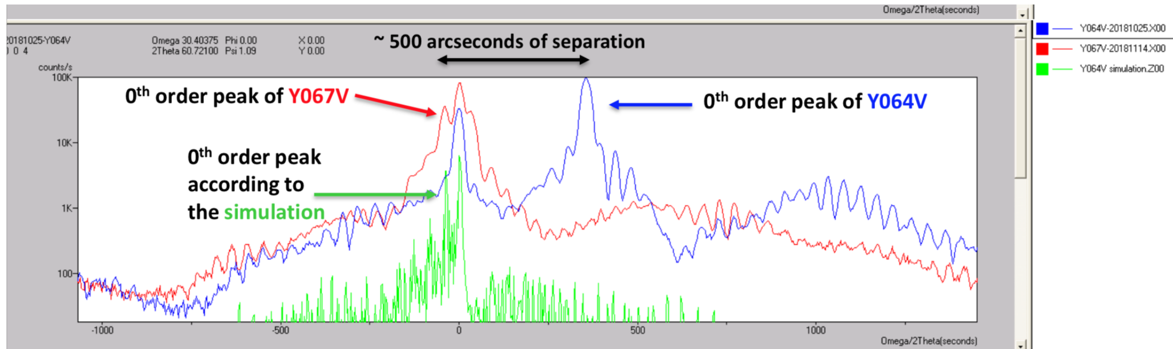

Figure 120: X-ray diffraction (XRD) scans of Y064V and Y067V.

In comparing Y064V to Y067V, there are clear indications of superior material quality in the latter, which includes tighter substrate/0th peak separation, more visible higher order satellite peaks, and better agreement with the zero stress design. Indeed as compared to the simulation one can notice that the zeroth peak is shifted in the case of Y064V due to the remaining Arsenic in the chamber, which is solved in the case of Y067V, using an Antimony soak step during the growth of the absorbers.Consequently, by giving the chamber a few seconds to pump out the excess of Arsenide, as well as flooding the chamber with Antimony (the soak) we are attempting to minimize this effect. A comparison study between the surface condition of Y064V and Y067V will be conducted below.

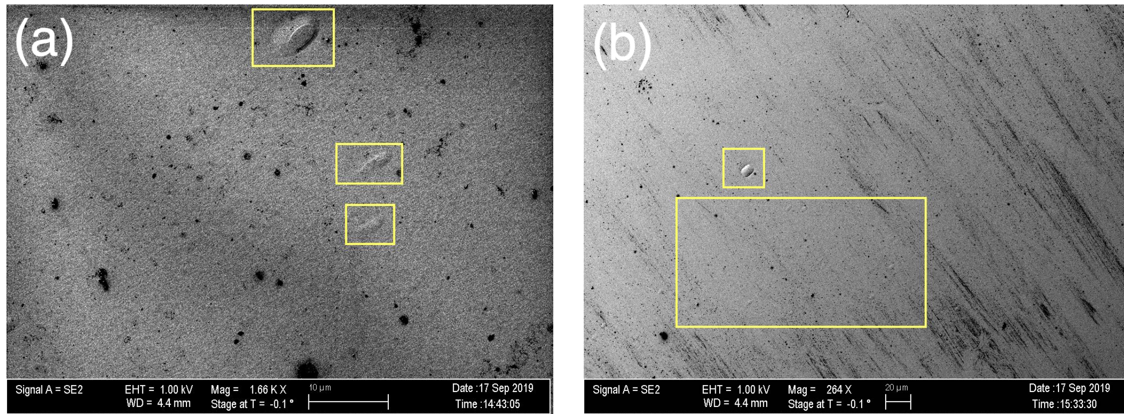

Figure 121: SEM micrographs of the background of Y067V taken with the ZEISS Neon 40 EsB. Both images were taken using the Everhart-Thornley detector but at different magnifications.

Figure 121 shows two examples of the background of Y067V. Figure (a) was taken at a fairly low magnification (1kX) whereas figure (b) was taken at a lower magnification (264 X). A low density of hillocks, highlighted in yellow boxes, was observed. Indeed the hillocks are spread throughout all the samples but are isolated from each other most of the time. The black lines or spots that are noticeable on the surface are due to contamination. However, in figure (a) only three hillocks including two that are shallow were detected. Indeed the detector we used for taking these images are not the conventional or most appropriate detector for this type of work. The information collected by this detector is roughly 90 % of secondary electrons, which is great to analyze the surface structure but only 10 % of backscattered electrons that give complementary data about topographical contrast. In our case, using a dedicated backscattered detector will be more suitable to be more topographically sensitive.

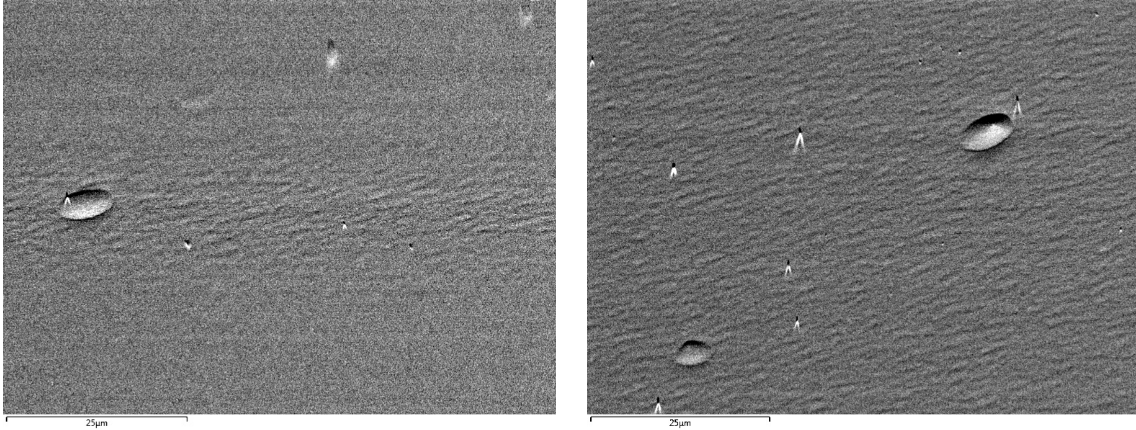

Figure 122: SEM micrographs of the background of Y067V taken with the ZEISS Neon 40 EsB. Both images were taken using the backscattered detector present on the EBSD camera. The sample was tilted by 70 degrees with respect to the beam using the appropriate EBSD sample holder.

A difference between the surface condition using this detector was noticed in figure 122. Small topographical variations throughout the surface of the sample were noted. However an equal density of hillocks in both figure 122 and 121 was observed.

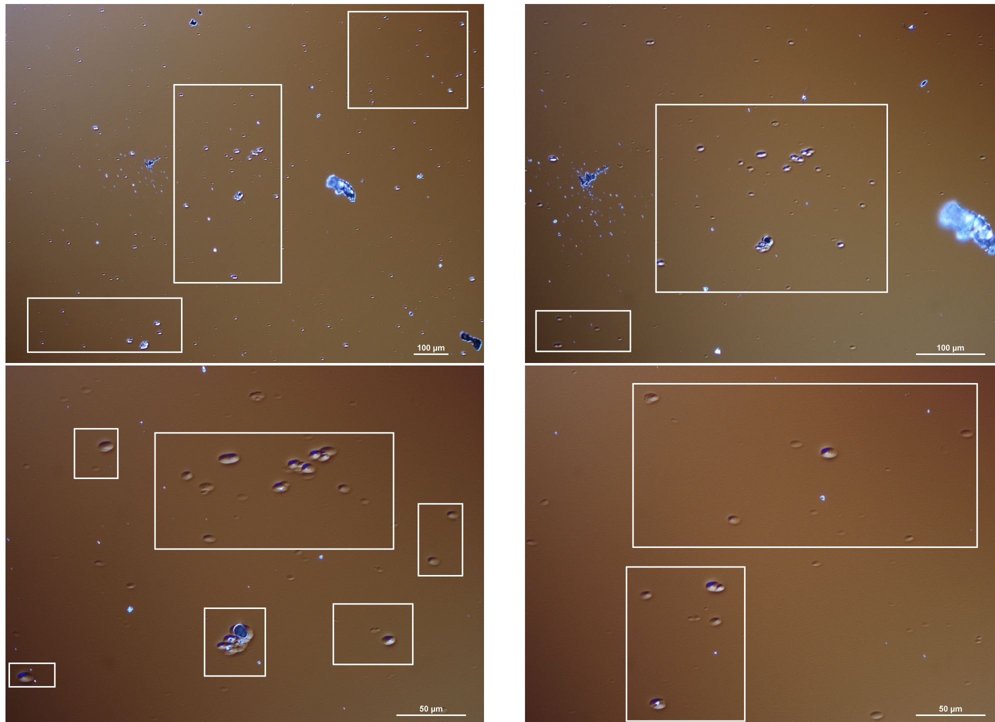

Figure 123: Background micrographs of the surface of Y067V taken with the DIC Microscope. The top images were taken at 10x and 20x whereas the bottom ones were taken at 40x.

Figure 123 depicts the hillocks present on the surface of Y067V, highlighted in white boxes. Small formation sites of hillocks throughout the surface were noted. By averaging the density of defects on several sites, a density of defects of $2.8 \times 10^4\ cm^{-2}$ was measured, which is 50 times smaller than the previous density of defects calculated for Y064V.

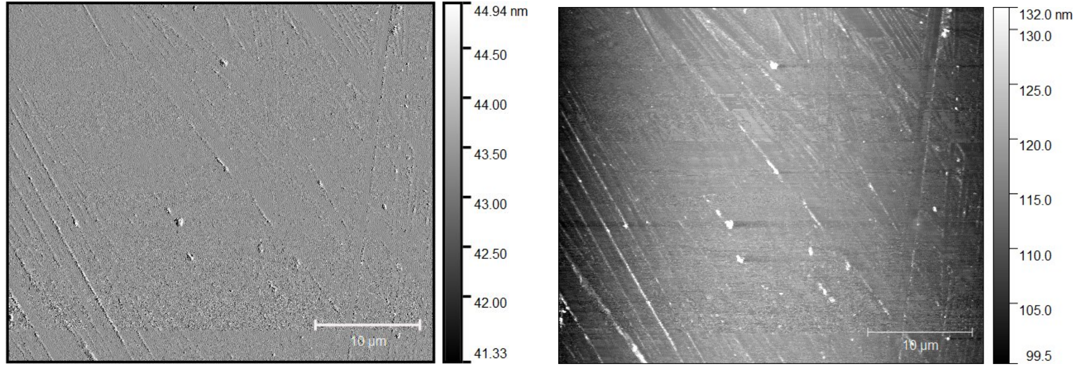

Figure 124: AFM height channel image and amplitude image of the background of Y067V.

The surface condition of the background in figure 124 is smooth. However, many lines on the surface of the sample due to dust contamination were observed.

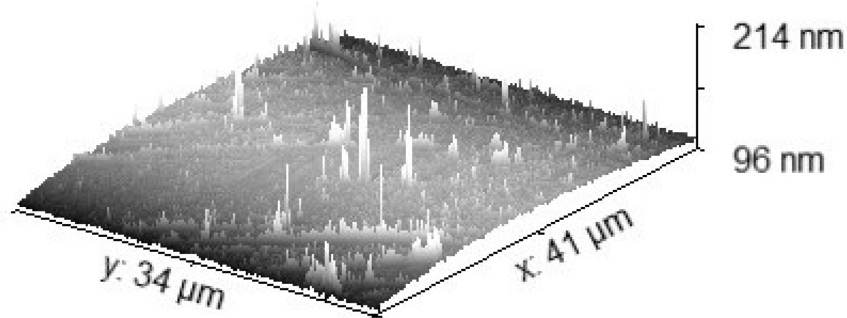

Figure 125: 3D representation of the background of Y067V.

In figure 125, the 3D representation of the background shows that the surface of the sample seems bent.

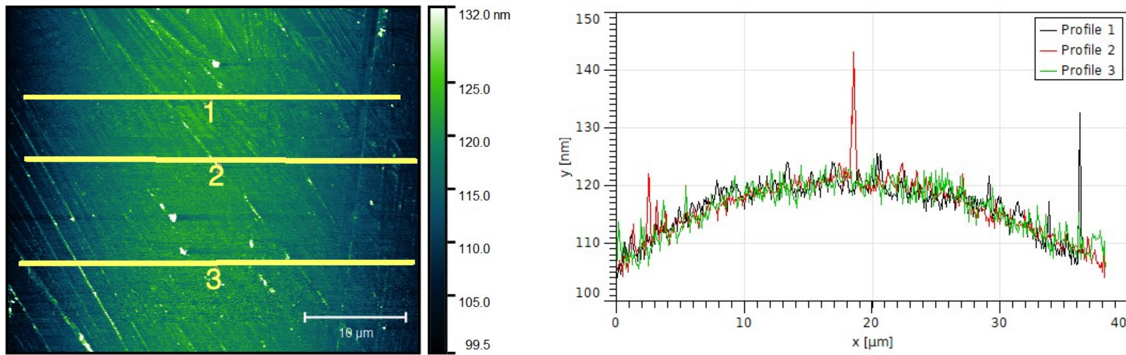

Figure 126: Data analysis of the background of Y067V.

As seen from the different line profiles extracted from the height micrograph (fig.126), the surface is bent. However, it is more likely to be an artifact of scanning because the first and final point of the line profiles has the same height. Concerning the topographical variation on the surface, they are oscillating from ± 5 nm which is negligible in comparison to the sample thickness. By averaging the roughness (RMS) using additional data, an average roughness of 5.8 nm with features on the surface that have a maximum height of 11.5 nm was determined. A higher RMS roughness in this case was noted, mainly due to a problem of dust contamination on this sample which exaggerates the actual RMS roughness.

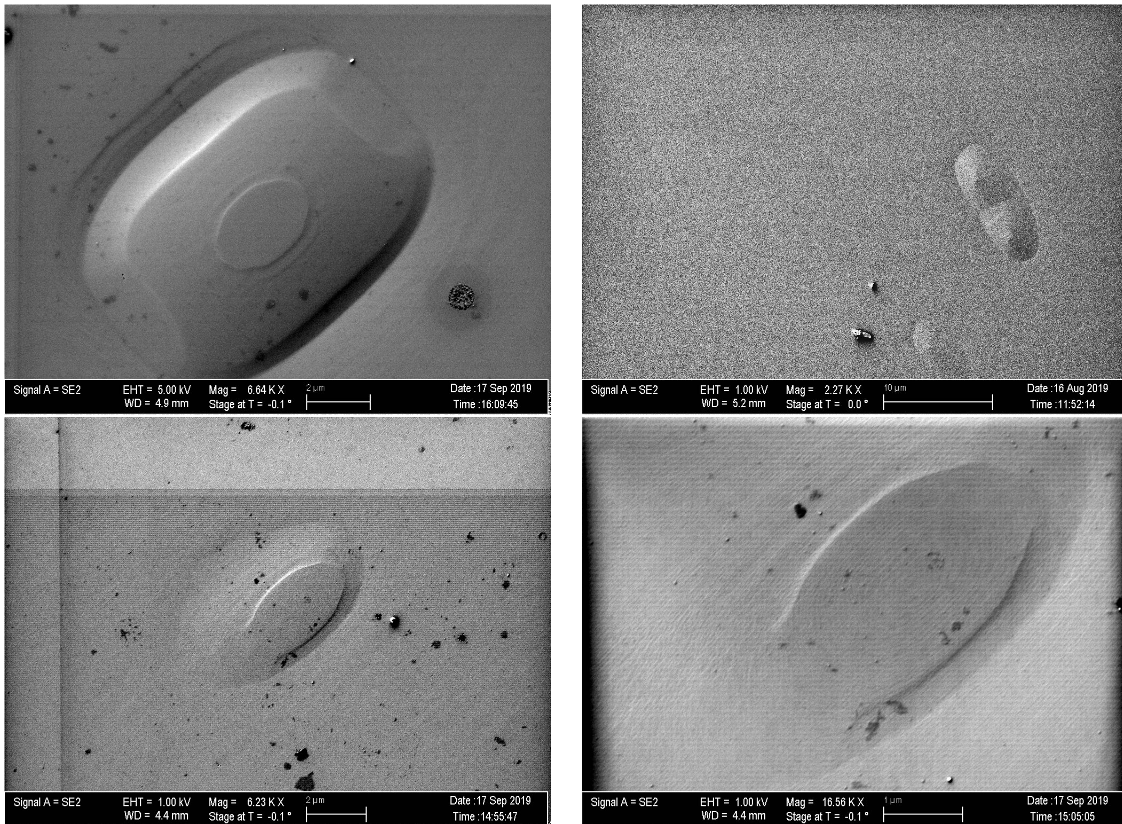

Figure 127: SEM hillock images on the surface of Y067V taken with the ZEISS Neon 40 EsB. Every image was taken with the Everhart-Thornley detector.

Figure 127 depicts a variety of different hillocks on the surface of Y067V. A smooth surface of the hillock with different layers on their surface like a stair shape was observed.

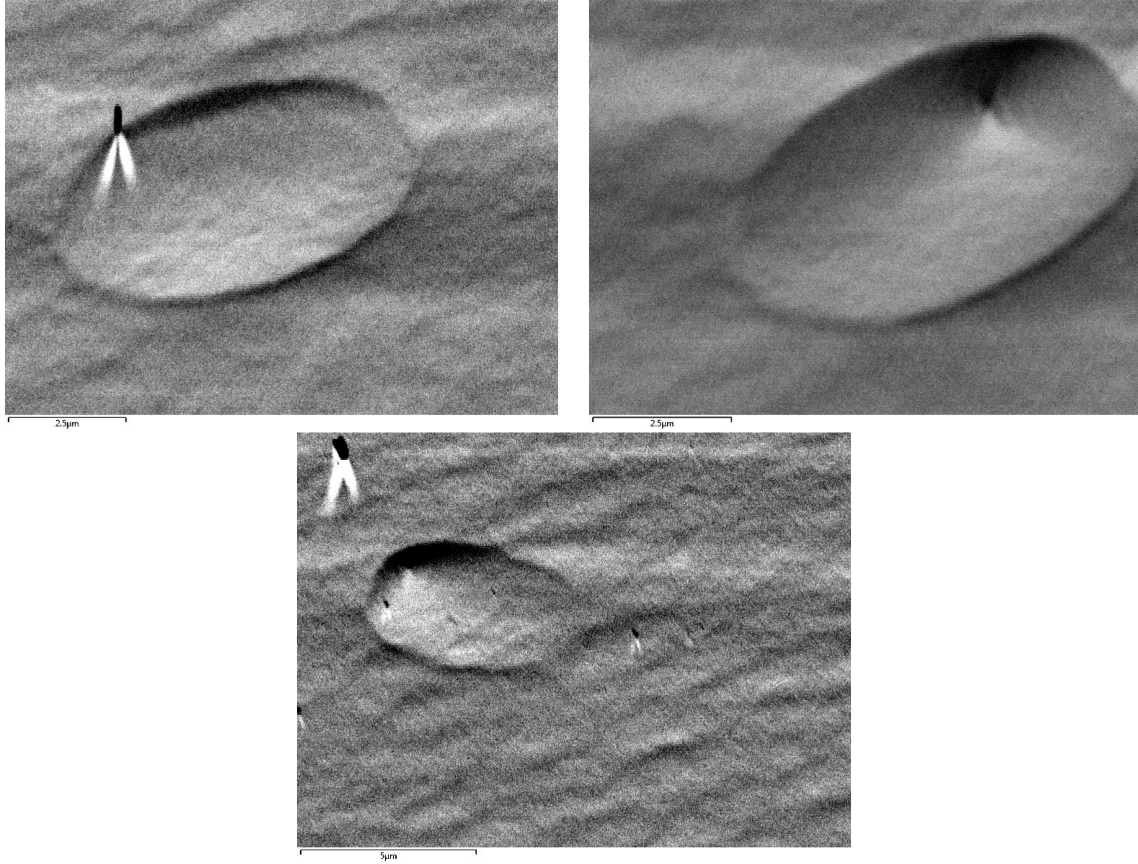

Figure 128: SEM images of the hillock present on the surface of Y067V taken with the ZEISS Neon 40 EsB. Every images was taken using backscattered detector present on the EBSD camera. The sample was tilted by 70 degrees using the appropriate EBSD sample holder.

The shape of the hillock in figure 128 is close to the one noticed for Y064V. An oval shape with a ripple at the summit was observed. The background also contains some irregularities.

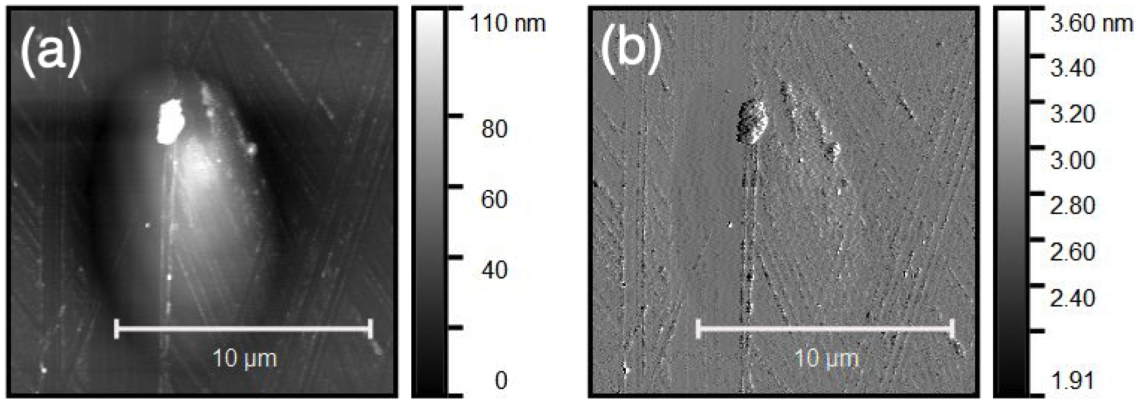

Figure 129: AFM height channel image and amplitude image of another hillock present on the surface of Y067V.

In figure 129, an example of a hillock under the AFM is depicted. In figure (b), the hillock appears as shallow which is due to the geometry of it. Indeed the amplitude channel is equivalent to a map of the slope of the sample; therefore if the slope is not abrupt the hillocks appears shallow. Furthermore, lines on the surface due to dust contamination were noticed.

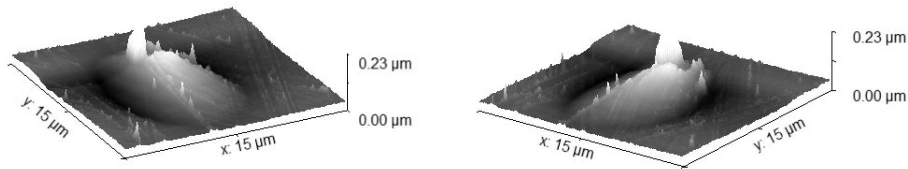

Figure 130: 3D representation of another hillock present on the surface of Y067V.

The hillock in figure 130 has an oval shape regarding to the X and Y-axis but it is slightly conical in the Z-axis direction. However the high peak that we see on the surface of the hillock is due to dust contamination once again.

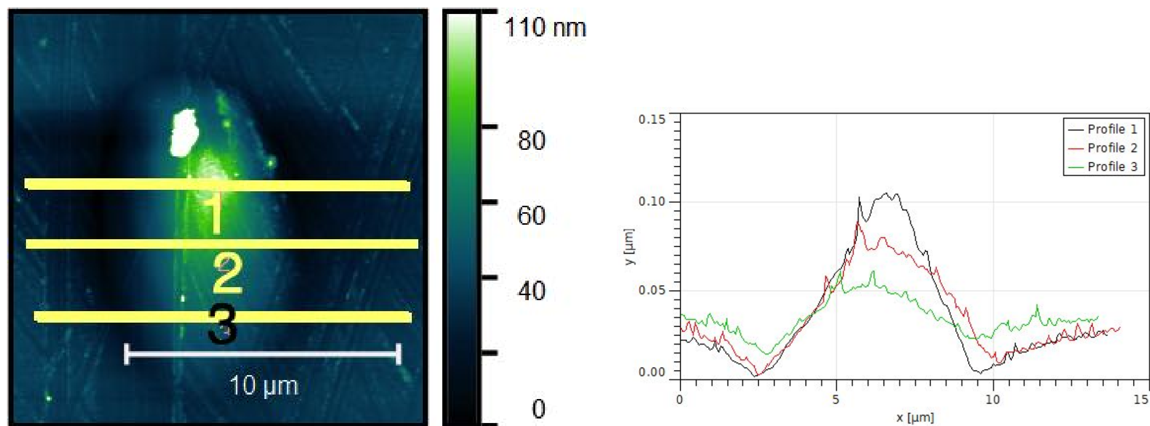

Figure 131: Data analysis of another hillock present on the surface of Y067V.

In figure 131, a hillock which has a maximum height of 100 nm is depicted. By averaging 8 other hillocks scanned, a hillock height of 55 nm with an average roughness (RMS) around them of 13.5 nm was calculated. Concerning the X and Y-axis, an X length of 6.2 μm and a Y length of 11.2 μm were measured. Those hillocks are slightly bigger than the one previously analyzed for the case of Y064V (fig.117).

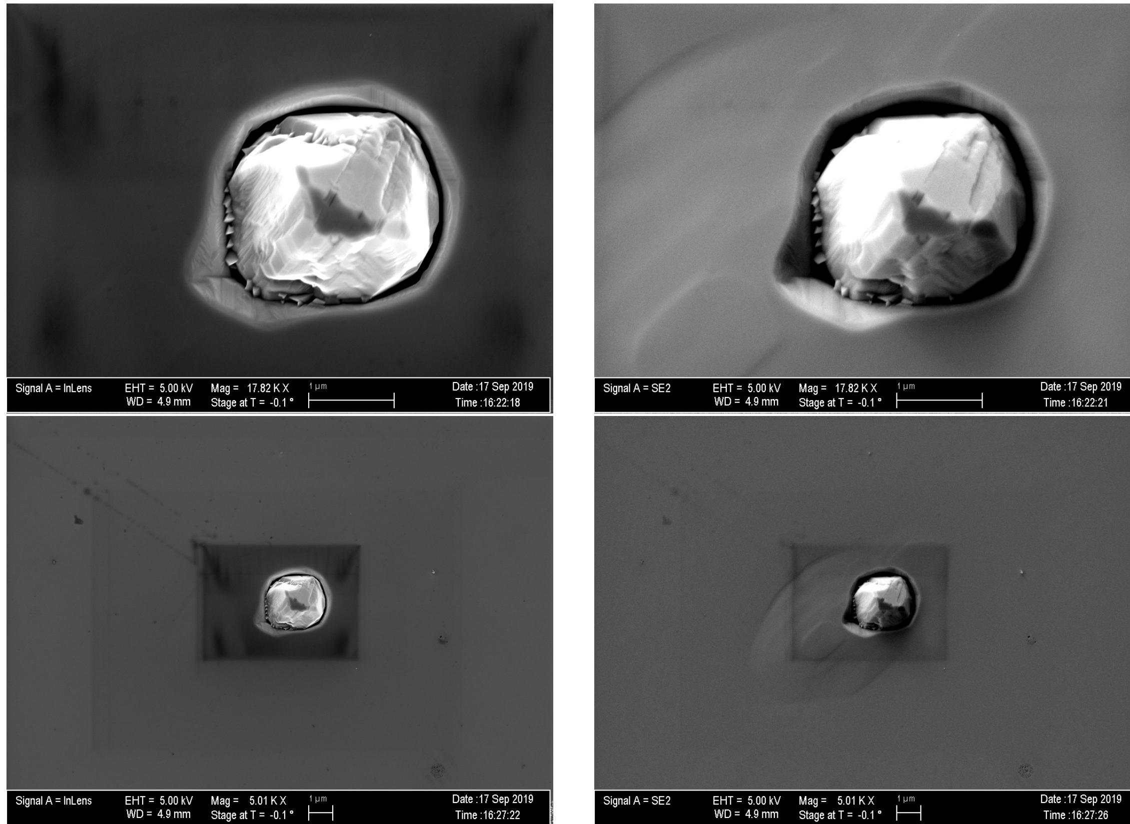

Figure 132: Metallic droplet on the surface of Y067V taken with the ZEISS Neon 40 EsB at high magnification (17 kX).

As seen in the example above in figure 132, the droplet created a cavity around it on the surface of the sample. It has a pyramidal shape but its size is smaller than the previous metallic droplets analyzed, with a size of ca. 1.5 μm. However, due to the shallow height of the hillocks it is hard to find them since the height of the hillock, ca. 50 nm is close to the ultimate height that the SEM can resolve.

4.3 Y074V 15 Stages with Antimony Soaks

The study will now focus on the last sample of the Interband cascade devices: Y074V. This sample is a 15-stages interband cascade photovoltaic device, with almost 2 times the number of stages in Y067V that was analyzed previously. Therefore it will be more likely to find defects on its surface due to the thickness of the material. Y064V/67V have

a targeted cutoff wavelength of 4.3 μm while Y074V has a targeted cutoff wavelength of 4.6 μm. To adjust the wavelength of the device, the thickness/composition of the superlattices were adjusted.

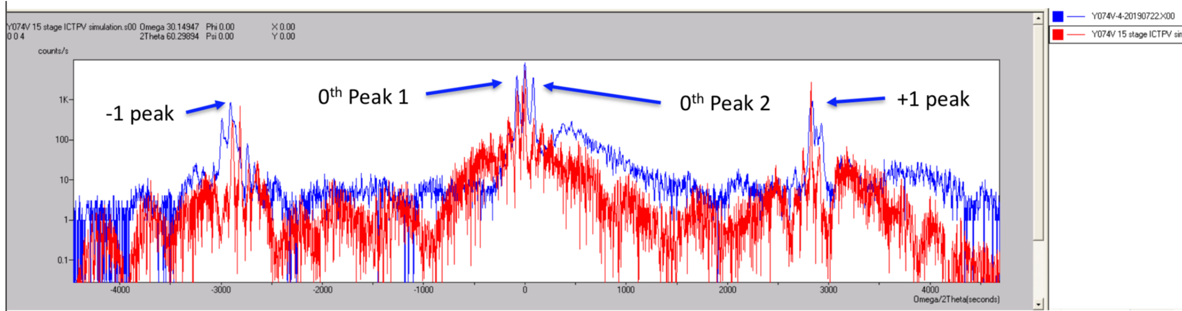

Figure 133: X-ray diffraction (XRD) scan of Y074V.

As seen in figure 133, one peak is due to the substrate (the central one), generally with the greatest intensity. The second is due to the zeroth order diffraction peak of the doped absorber. Here two zeroth peaks are detected. The first one (Oth peak 1) is the doped absorber and the second one (Oth peak 2) is due to the interaction of the Electron Barrier and Hole Barrier layers with the doped absorber. Indeed a recombination of the electrons and holes inside the material instead of moving to the extremity of the materials was supposed. However as seen the substrate peak of the simulation is almost at the same position than the calculated one. Consequently, it confirms that the materials grown meet the expectations.

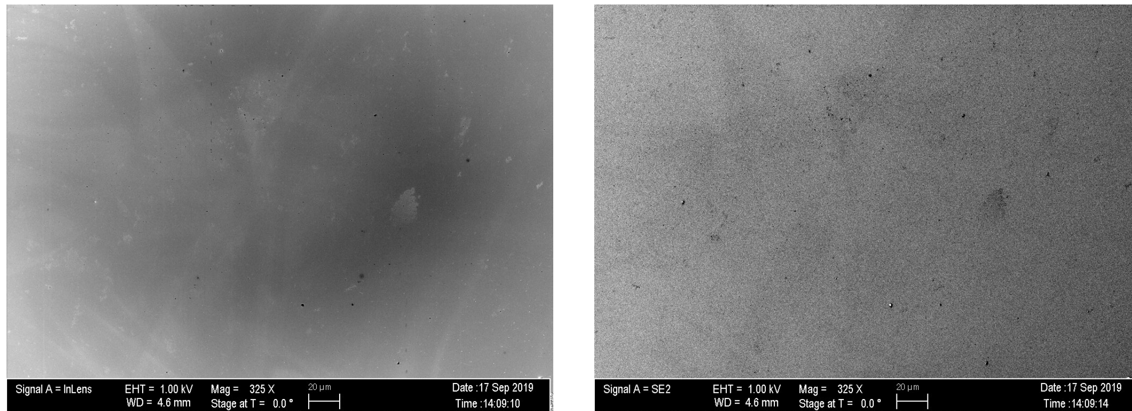

Figure 134: Background of Y074V taken with the ZEISS Neon 40 EsB. The left-hand side image was taken with the Inlens detector and the right-hand side with the Everhart-Thornley detector.

As seen in figure 134, both micrographs bring very little information about the surface of the sample or the presence of defects. A smooth sample with almost no contamination is depicted.

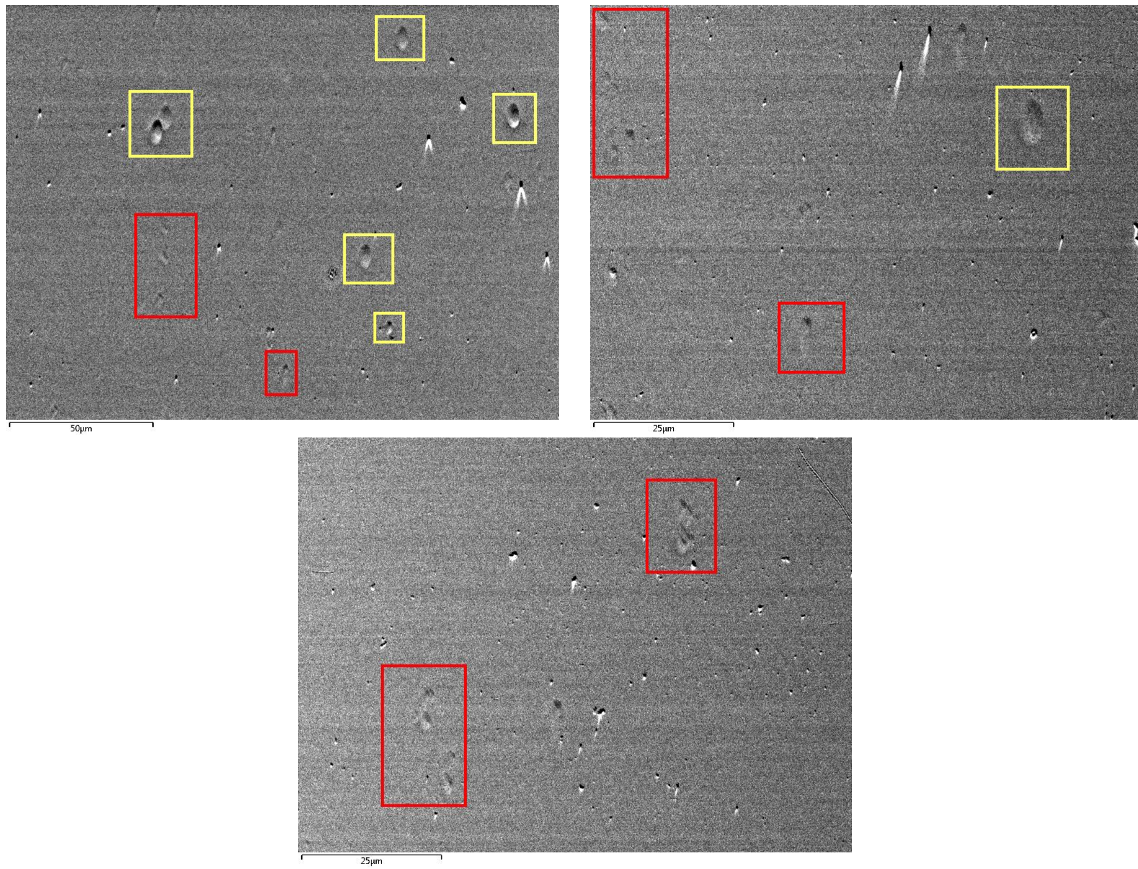

Figure 135: SEM micrographs of background of Y074V, taken with the ZEISS Neon 40 EsB. Every images was taken using the backscattered detector present on the EBSD camera. The sample was tilted by 70 degrees with respect to the primary beam using the appropriate EBSD sample holder.

In figure 135, using the backscattered detector present on the EBSD camera, some defects are noticeable on the surface of Y074V. The defects highlighted in red boxes are new defects and the one present in the yellow boxes are hillocks. Comparing to the previous sample Y067V one can immediately conclude that the density of defects is higher on this sample. Some horizontal lines throughout the surface of the sample were also noticed.

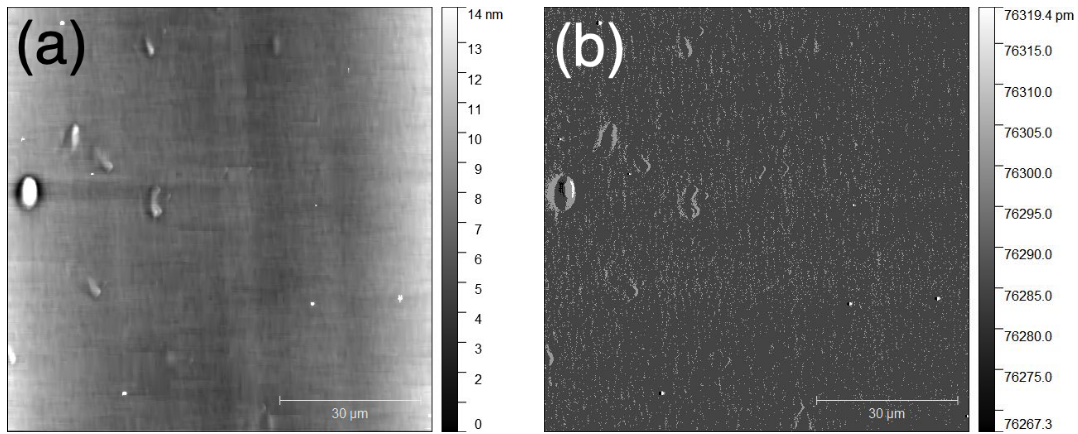

Figure 136: AFM height channel image and amplitude channel image of the background of Y074V.

In figure 136, the height channel in figure (a) and the amplitude channel in figure (b) of the background of Y074V are depicted. The presence of hillocks or new defects with different shapes, already noticed in the previous figure (fig.135) were observed.

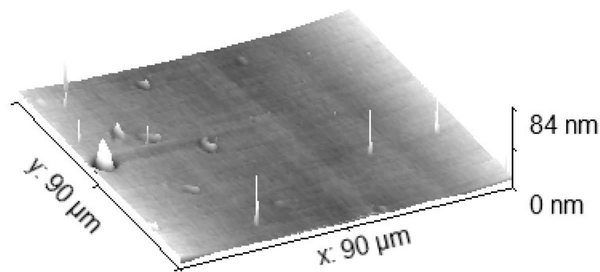

Figure 137: 3D representation of the background of Y074V.

The 3D representation of the background of Y074V (fig.137) illustrates that the hillocks on the surface are much bigger than the other defects on the surface.

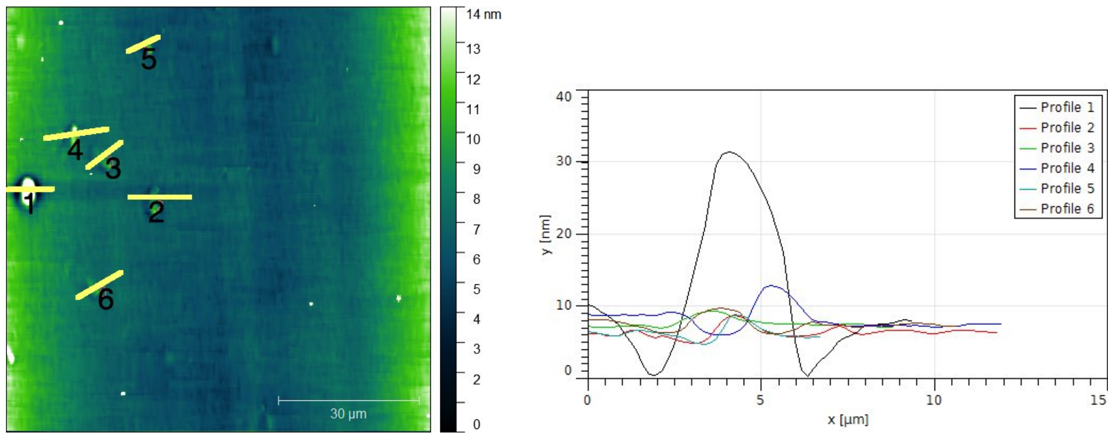

Figure 138: Data analysis of the background of Y074V.

From the data analysis in figure 138, one can compare the actual size of the different defects present on the surface of Y074V. A hillock height of ca. 32 nm, half of the previous hillock heights analyzed, was measured. However, the height of the new defects encountered on the surface is 5nm. By comparing the first SEM micrographs (fig.135) of the surface of Y074V with the actual size of the defects present on its surface it makes sense that the surface appears as smooth. Indeed with defects that have a height of 30 nm they cannot be detected using conventional SEM imaging technique (Secondary electrons detector) because the ultimate resolution along the Z-axis for this detector is 45 nm.By determining the roughness (RMS) and the maximum height of the defects present in the sample that does not have an oval shape hillocks, using 43 different defects an average roughness of 10.4 nm with features on the surface that have a maximum height of 4.8 nm was calculated.

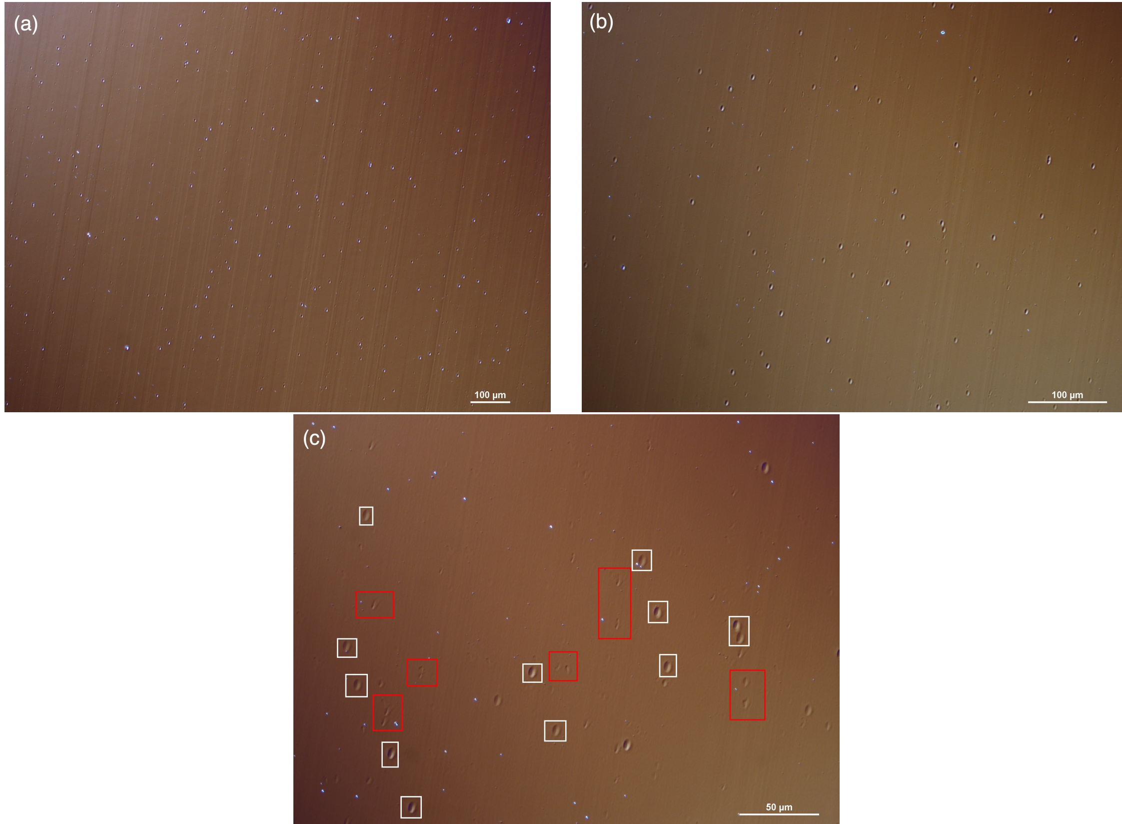

Figure 139: Background of Y074V taken with the DIC Microscope at different magnifications. Figure (a) was taken at 10x, Figure (b) was taken at 20x and Figure (c) was taken at 40x.

Figure 139 depicts the surface condition of Y074V using the DIC microscope. The hillocks are spread throughout the surface of the sample. Parallel lines that we already saw in (fig.135) were noticed. In Figure (c), the new defects are highlighted in red and the hillocks are highlighted in white. By counting the defects present on the surface for a given area several times, a density of defects of 9.5×10^4 cm^{-2} was calculated.

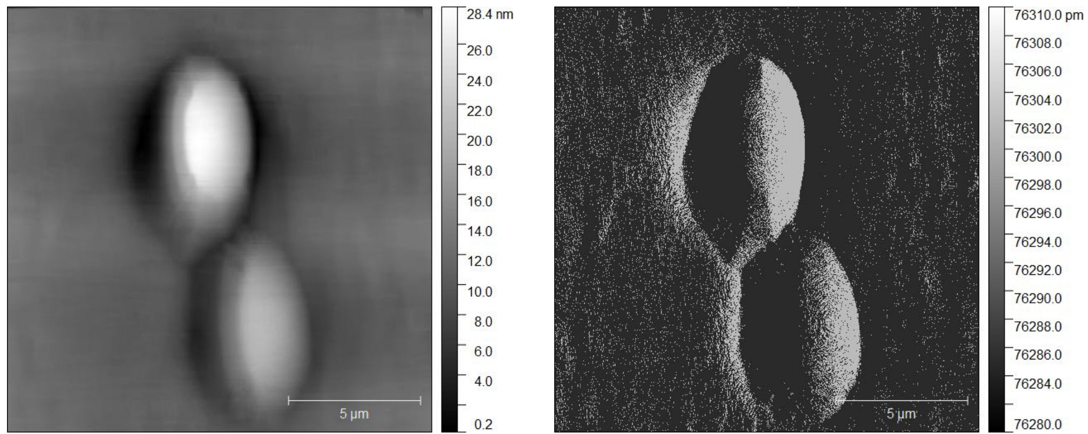

Figure 140: AFM height channel image and amplitude channel image of hillocks present on the surface of Y074V.

As seen in figure 140, hillocks with no irregularities on their surface were obtained.

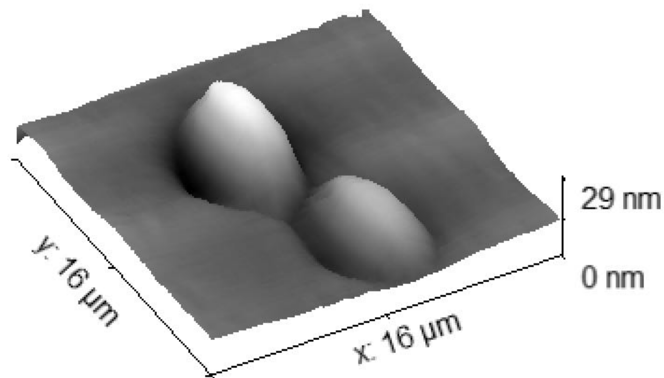

Figure 141: 3D representation of Hillocks present on the surface of Y074V.

From the 3D representation of the hillock in figure 141, one can immediately notice that the hillocks have a smooth oval shape, even along the Z-axis where their shapes are oval and not conical like the two previous samples analyzed.

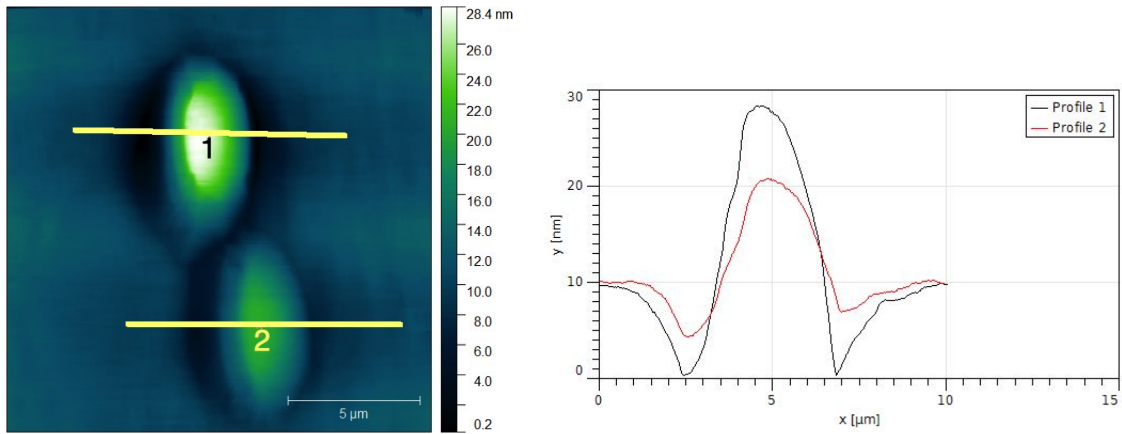

Figure 142: Data analysis of hillocks present on the surface of Y074V.

As displayed in figure 142, hillock heights of 30 nm and 17 nm were measured. From additional data from 15 hillocks present on the surface of Y074V an average roughness of 17.8 nm around the hillocks with a maximum height of 23.7 nm was calculated. Concerning the X and Y-axes, an average length of 4.1 μm and 7.2 μm respectively was obtained.

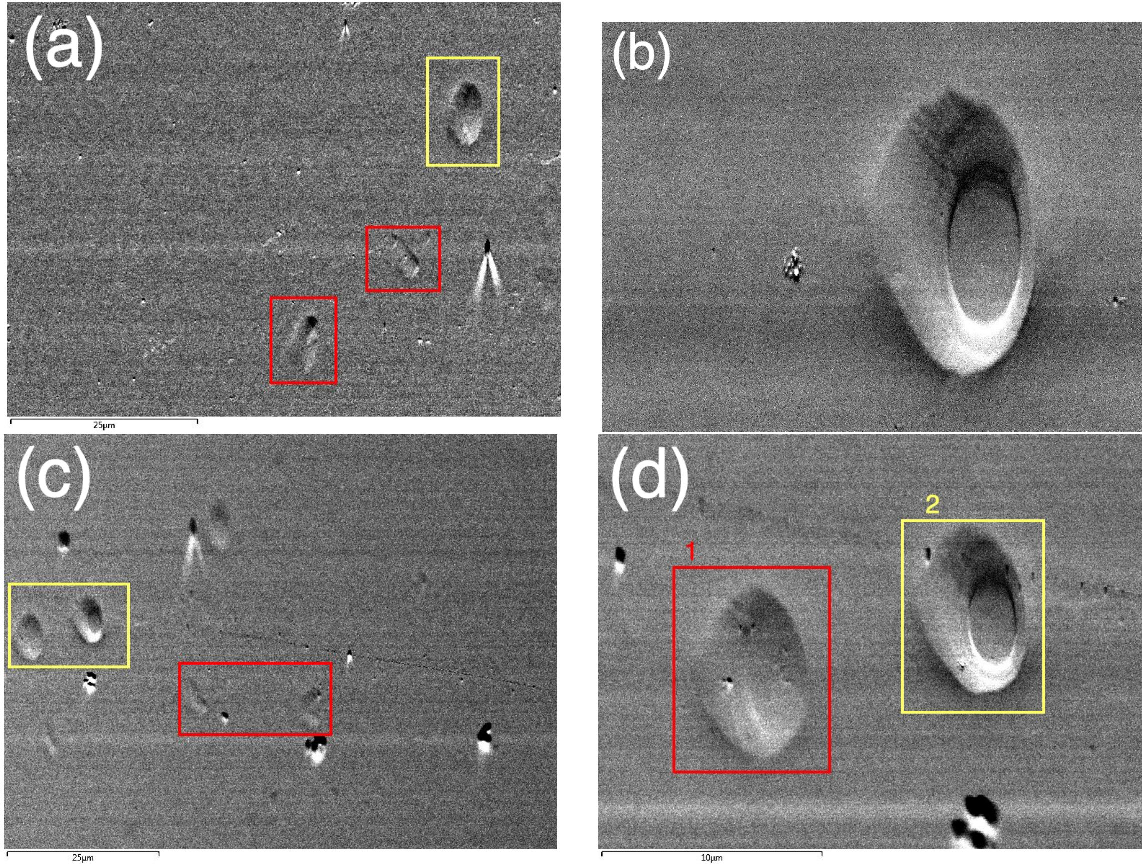

Figure 143: SEM micrographs of hillocks and new defects present on the surface of of Y074V taken with the ZEISS Neon 40 EsB. Every micrograph was taken using the backscattered detector present on the EBSD camera. The sample was tilted by 70 degrees with respect to the primary beam using the appropriate EBSD sample holder.

Figure 143 shows the shape of the hillocks present on the surface of Y074V. They do not have the same shape, varying from very little topographical variations on their surface, highlighted in the red labelled 1 in figure (d) to a flatter appearance with different layers on the surface of the hillock, highlighted in the yellow box labelled 2.

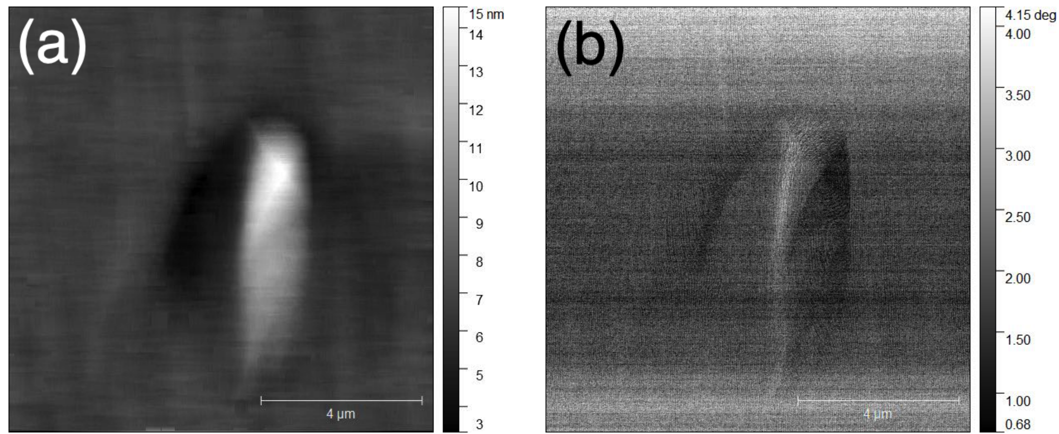

Figure 144: AFM height channel image and phase channel image of a new type of defect present on the surface of Y074V.

In figure 144, an example of new defects present on the surface of Y074V is depicted. Figure (a) is the height channel of the new defect and figure (b) is the phase channel. The amplitude image was not relevant because the scan did not encountered any abrupt variations.

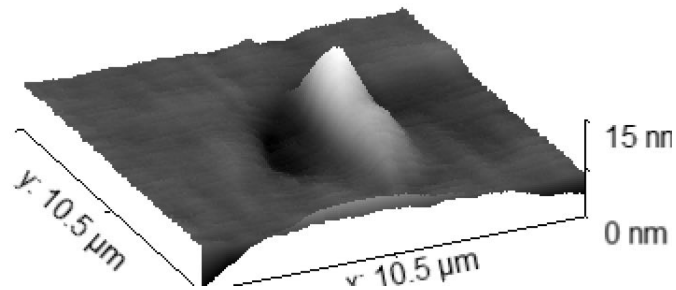

Figure 145: 3D representation of a new type of defect present on the surface of Y074V.

As seen from the 3D representation of the defect in figure 145, the shape of this defect is close to that of the hillock. However, there are some differences :

- A lower area on the left side of the defect
- Different altitudes along the Z-axis
- A non-centered mountain shape

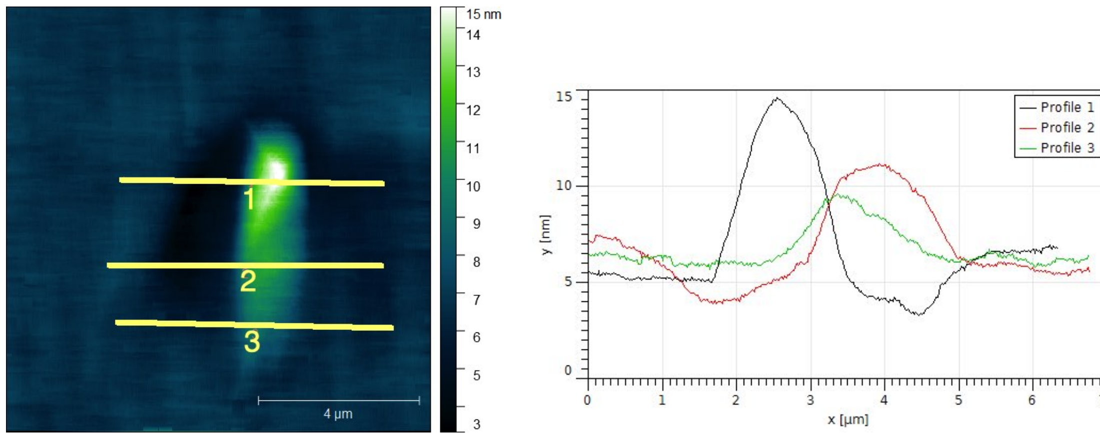

Figure 146: Data analysis of a new type of defect present on the surface of Y074V.

As shown in figure 146, the maximum height of the defects is 10 nm with another level at ca. 6 nm. The shape of these defects and the asymmetrical shape along the Z-axis imply that this defect was a hillock created in an inner layer of the semiconductor during the growth process. This shape may be caused by atoms filling out some part of the hillock. It grows unevenly on this surface, which creates a mountain-like shape.

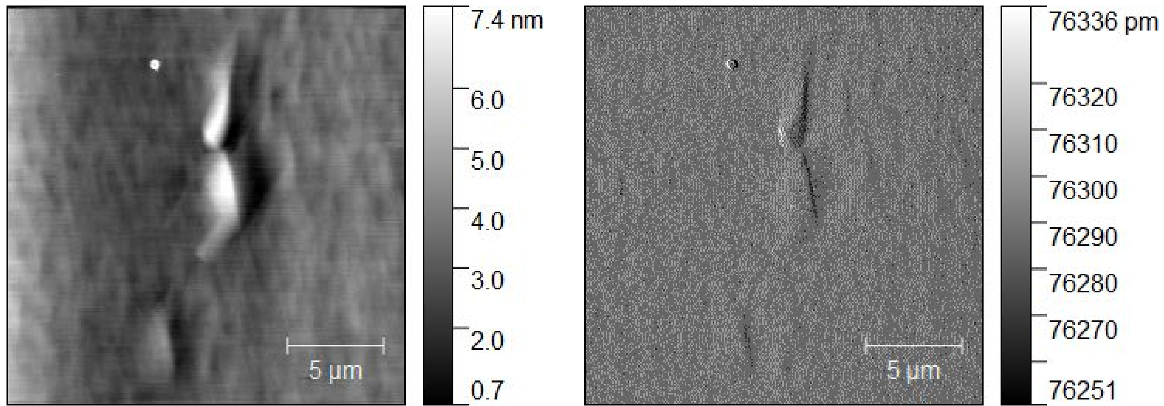

Figure 147: AFM height channel image and amplitude channel image of another type of new defect present on the surface of Y074V.

In figure 147, another type of defect is apparent on the surface of Y074V. By the shape of these defects, one can suppose that they are similar to hillocks that were created in an inner layer of the material. This would explain their shallow height because the growing layer grew faster around them.

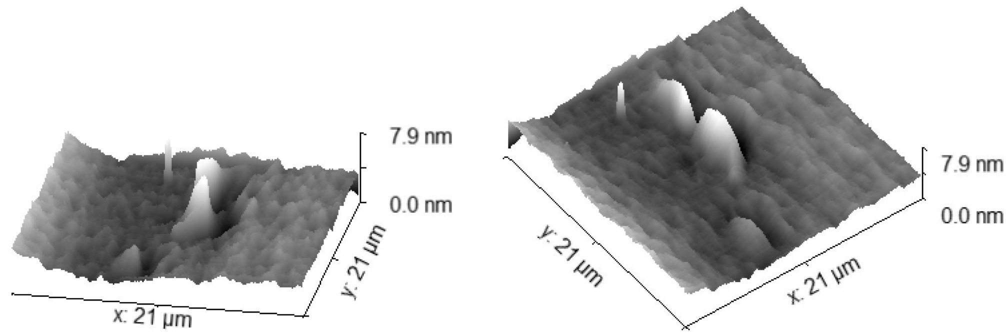

Figure 148: 3D representation of another type of new defect present on the surface of Y074V.

Figure 148 depicts the new type of defects in 3 dimensions. A mountain shape with a steep slope stretched along the Y-axis was noted for this type of new defects.

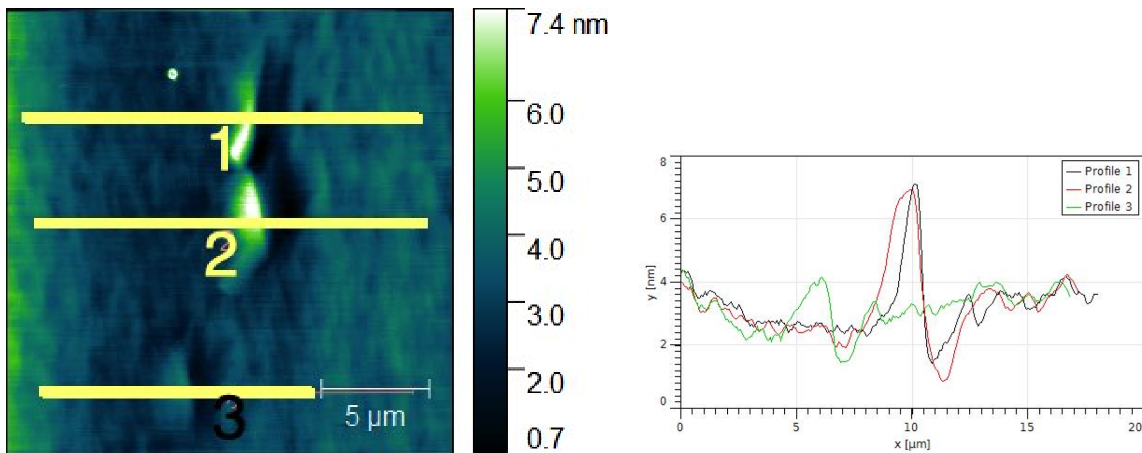

Figure 149: Data analysis of another type of new defect present on the surface of Y074V.

From the extracted line profiles at strategic points (fig.149) a maximum height of these defects of ca. 4 nm was measured. From the 3D representation of these defects (fig.148) and the actual height of these defects, one can suppose that these defects were hillocks created during the growth process in an inner layer of the material. However, regarding the size of these defects, one can presume that they were created in a deeper layer of the material than the previous one analyzed, (fig.144) which was almost created at the surface of the specimen.

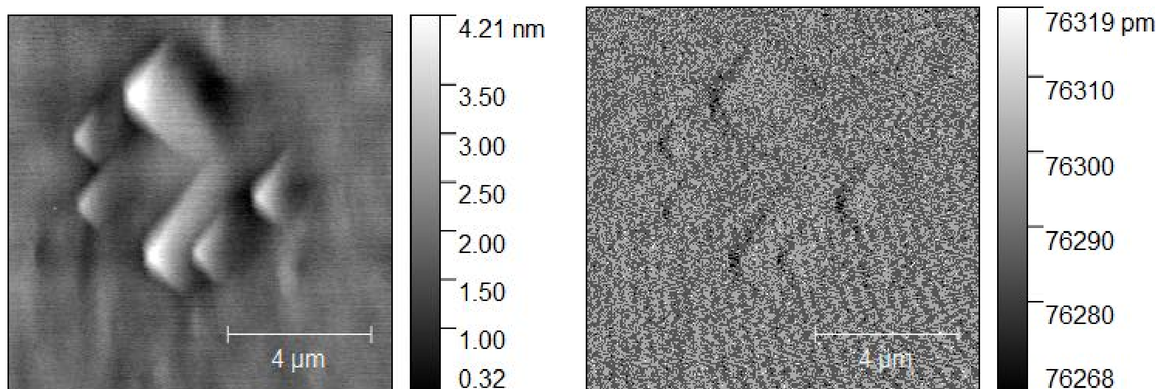

Figure 150: AFM height channel image and amplitude channel image of pyramidal defects present on the surface of Y074V.

As seen in figure 150, there are some pyramidal defects on the surface of Y074V.

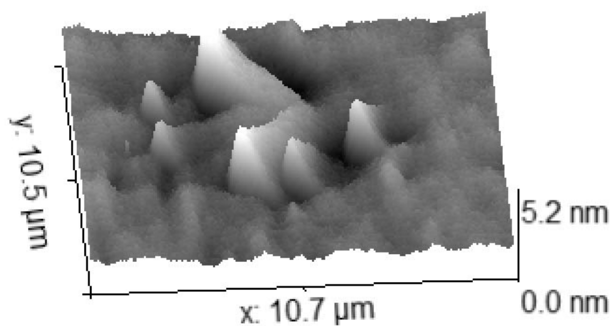

Figure 151: 3D representation of pyramidal defects present on the surface of Y074V

Figure 151 depicts the 3D representation of the pyramidal defects present on the surface of Y074V. Further investigation is needed to determine the height of the pyramidal defect accurately.

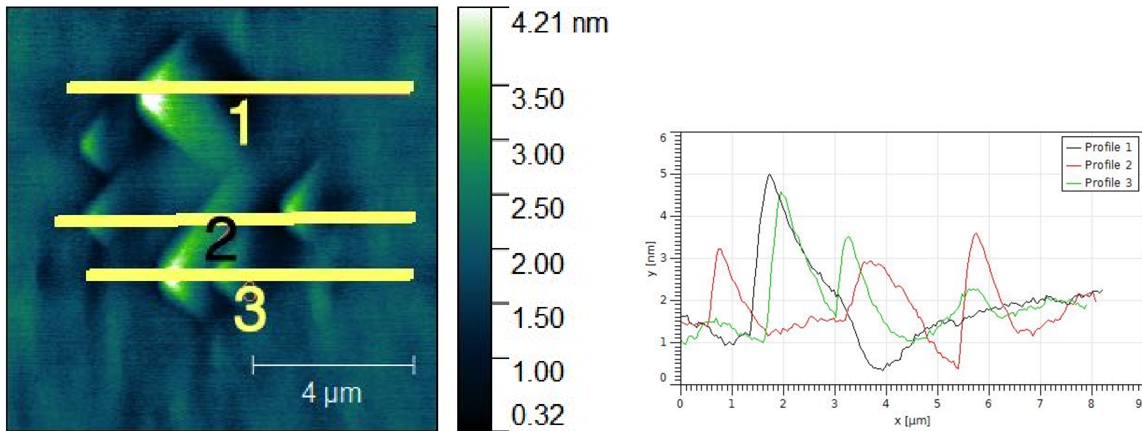

Figure 152: Data analysis of pyramidal defects present on the surface of Y074V.

As seen from the extracted profile lines in figure 152, a maximum height of the pyramidal defects of 4 nm was measured. This height is shallow in comparison to the thickness of the material, which is ca. 5 μm. The origin of these defects is unknown for now. Further experiment comparing different samples will be needed to determine when these defects are created.

4.4 Y064V Analysis on the Same Area using Different Microscopy Imaging

This study will focus furthermore on Y064V due to the highest density of hillocks on its surface which makes it easier to find features of interest.

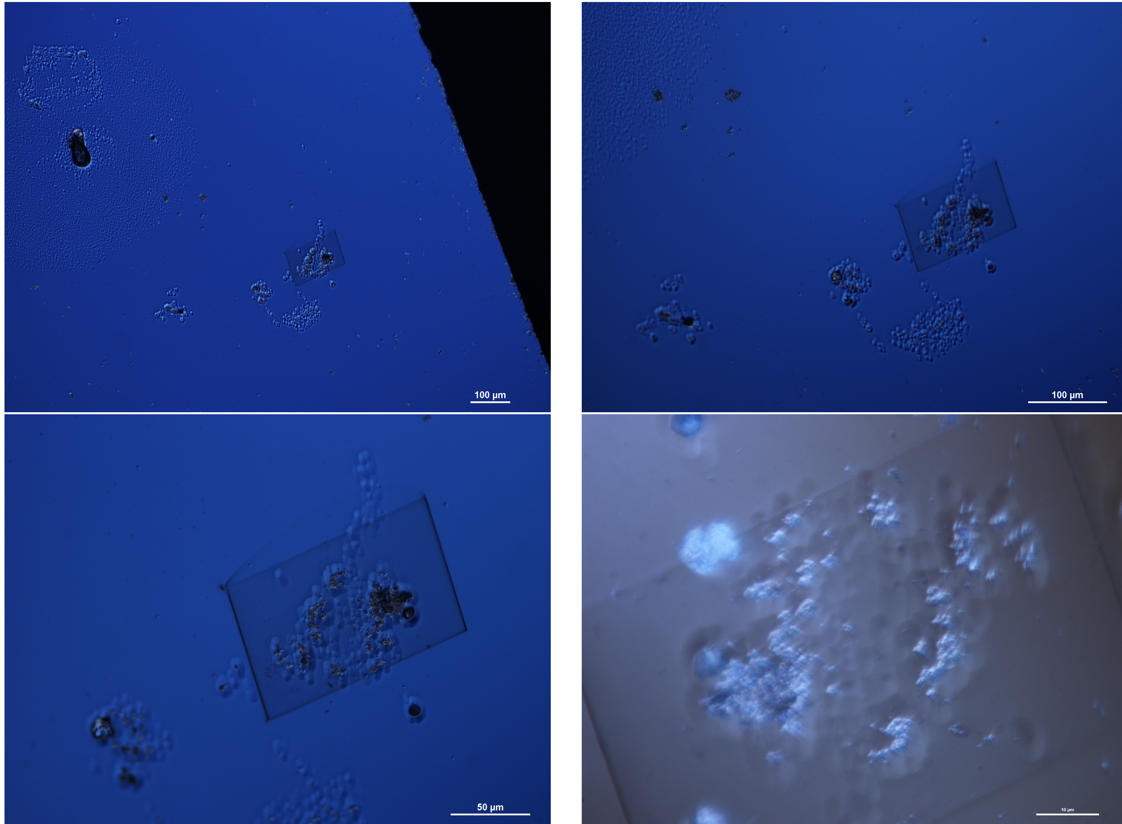

Figure 153: DIC images of the hillocks present on Y064V used for an analysis using different microscopes. The images were taken at different magnifications (10x to 100x).

As shown in figure 153, the area chosen has a high density of hillocks with some scratches/holes at the top of some of them. The rectangle area that is noticeable in the background is due to carbon contamination after the EBSD analysis. This was also used as a reference to find the same spot under different microscopes. Blue features that are seen on the highest magnification image at 100x (bottom right-hand corner) are not dust contamination but the inner layers of the semiconductor structure.

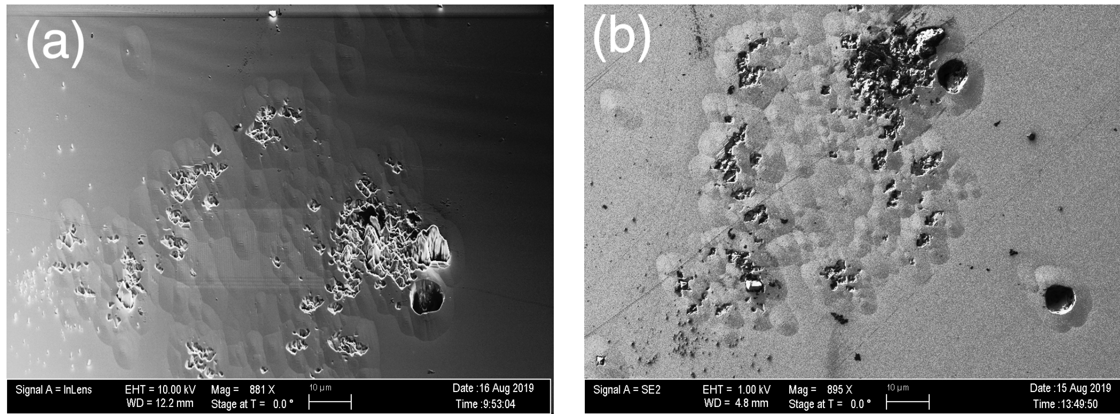

Figure 154: SEM micrographs of the hillocks present on Y064V used for an analysis using different microscopes taken with the ZEISS Neon 40 EsB in two different configurations.

The two SEM micrographs (fig.154) were taken in two different configurations. Figure (a) was taken using the Inlens detector in the EBSD configuration, with the sample mounted on the EBSD sample holder (tilted by 70 degrees) with a high accelerating voltage (10 kV) and a large aperture size of 60 μm. Figure (b) was taken with the traditional SEM configuration, using a sample holder not tilted, a low accelerating voltage (1kV) to be more surface sensitive and the smallest aperture size to have a higher resolution image. The difference of grey color that occurred in figure (a) are due to carbon contamination lines. Indeed the Inlens detector is more sensitive to carbon contamination whereas the Everhart-Thornley detector filters out more the contamination features. However, now we have a better representation of the surface of the sample under the SEM in comparison to the DIC images that we saw previously. Using the EBSD camera that provides a backscattered detector, the SEM micrographs in the next figure will be more surface sensitive.

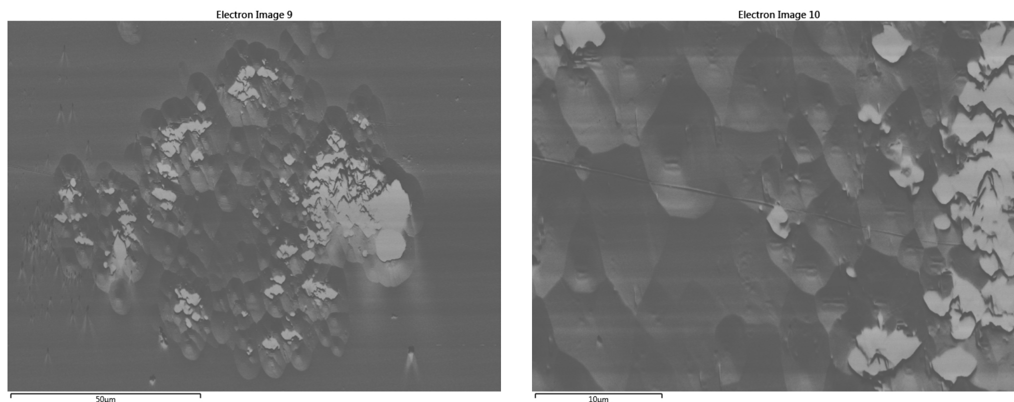

Figure 155: SEM micrographs of the hillocks present on Y064V used for a analysis using different microscopes taken with the ZEISS Neon 40 EsB. The image was taken at different magnifications in the EBSD configuration (sample titled by 70 degrees) with the BSE detector present on the EBSD camera.

In comparison to the previous figure (fig.154), this case (fig.155) has more information about the hillocks and the background. However, the area with high topographical contrasts appearing as blue under the DIC and that was clear using secondary electron images are now appearing as white and blurry. Figure 155 was taken in the same area but at different magnification. When compared the shape of the hillock under the SE2 images (Everhart-Thornley detector) the hillocks seem smooth whereas on the true BSE images (fig.155) one can notice that they is some ripple on the top of the hillocks. Now that there is an understanding about how the hillocks appear using 3 different types of microscopy images, the height of the hillocks will be determined using the Atomic Force Microscope for this area.

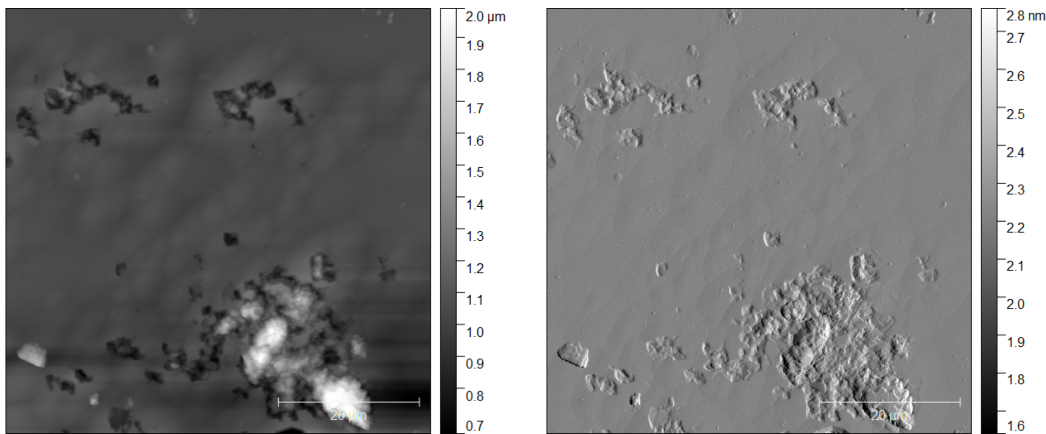

Figure 156: Height channel image and amplitude image of the hillock present on Y064V used for a analysis using different microscopes, taken with the Atomic Force Microscope.

The topographical contrast in figure 154 that was already observed under the SEM with the Inlens detector around the hillock is indeed very high, 2 μm. However, the hillock on the surface seems shallow. This is probably a consequence of the high topographical areas around them that minimize the height of the hillock.

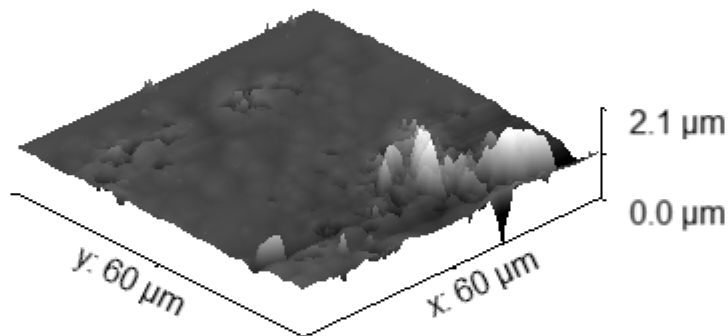

Figure 157: 3D representation of the hillock present on Y064V used for an analysis using different microscopes taken with the Atomic Force Microscope.

Figure 157 highlights the high topographical contrast areas around the hillock which flattened the hillocks.

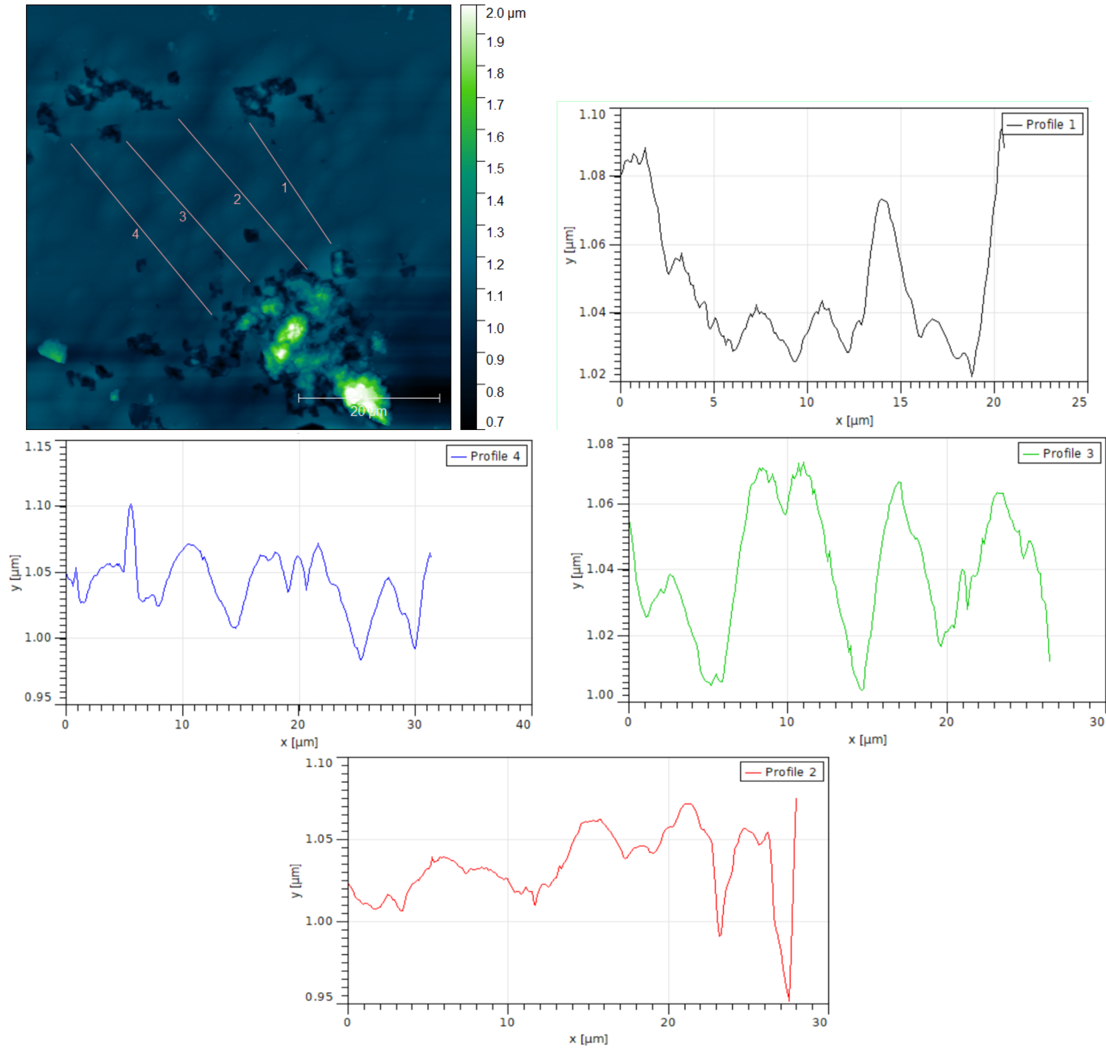

Figure 158: Data analysis of the hillocks present on Y064V used for an analysis using different microscopes taken with the Atomic Force Microscope.

From the extracted line profiles in figure 158, an average height of the hillocks analyzed of 61 nm was obtained.

4.4.1 Y064V EBSD Analysis

Now that the heights of the hillocks have been determined and a clear idea of the shape of them has been made, one can do further analysis on the hillocks using EBSD to determine the orientation of the hillocks. The process of this technique was explained in the background section 1.4.

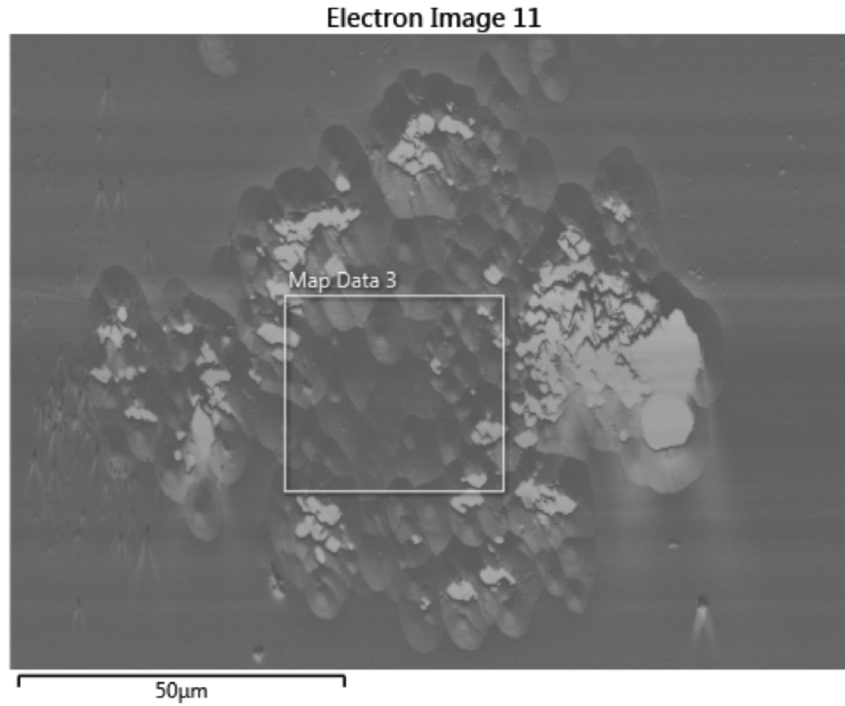

Figure 159: Backscattered image used for the EBSD analysis of hillocks present on the surface of Y064V.

Figure 159 depicts the area that was scanned for the study. The figure used is the same as the one previously seen (fig.155) except this analysis will focus only on the hillock part of the image.

4.4.2 Quality of the scan

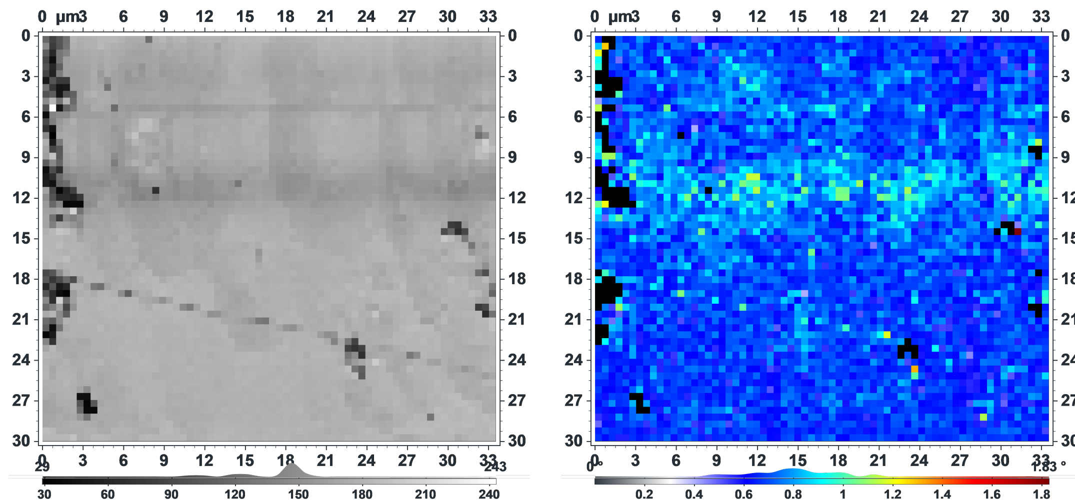

Figure 160: Mean Angular Deviation (MAD) and band contrast map of the EBSD analysis of hillocks present on the surface of Y064V

Figure 160 displays the band contrast map and the MAD map. The overall band contrast map is at a greyscale close to roughly 150 as seen on the horizontal greyscale bar below the band contrast map. This value is superior to the median greyscale level (122) which means that the scan is in an overall good scan. Indeed knowing that for each point a greyscale value will be determined, then if this value is closer to white (255) it means that the scan error will be smaller. The only poor fit spots (black spots) seen on the band contrast map are the high topographical areas with a height close to 2 μm. They appear as black either because they are due to a scratch on the surface and no relating phase was found during the scan or because we are suffering from a shadow effect once again. Concerning the Mean Angular Deviation (MAD) Map, a misfit angle of 0.8 degrees, not so far from the 0.5 degrees which is considered as an excellent fit [25], was obtained. Considering the complexity of the semiconductor structure, composed of a high number of stages with different concentrations of InSb, AlSb and GaSb, this value can be considered as a good result. Moreover from the Aztech Data Base, the exact concentration of InSb, GaAs, and AlSb composing the sample was not found. Consequently, by just adding those three phases separately one is committing an error which probably results in a higher misfit angle.Nevertheless, this angle is not that far from the suitable angle used for an EBSD pattern so we can conclude that the data obtained are reliable.

4.4.3 Orientation Study

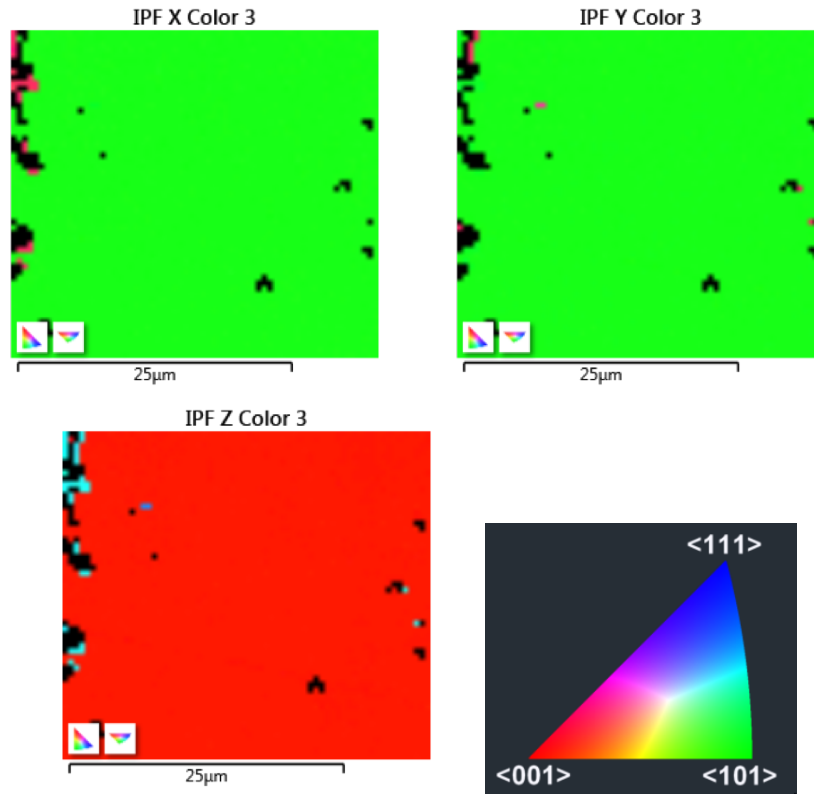

Figure 161: Inversion Pole Figure X,Y,Z map of the EBSD analysis of hillocks present on the surface of Y064V.

Figure 161 displays the inverse pole figure maps related to the three orientations X, Y, Z.On the X and Y Inverse Pole figure maps, both of them are facing in the 101 direction. However, on the Z direction, the 001 direction was observed, which is the orientation of the substrate. From these maps, one does not have more information about the orientation of the hillock in itself and investigation using the grain study to determine local misorientations needs to be conducted.

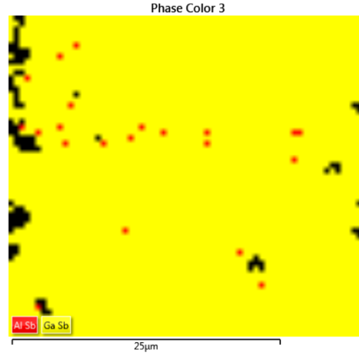

Figure 162: Phase map of the EBSD analysis of hillocks present on the surface of Y064V.

Figure 162 depicts the phase map of the EBSD analysis of the surface of Y064V on the hillock area. Almost only the GaSb phases were found throughout the surface, corresponding to the cap layer, which is probably due to the thickness of this layer in comparison to the other epilayers. However, from the few solutions that the software found as AlSb, it is hard to say whether or not those points are indeed AlSb or if the MAD value and the band contrast greyscale value was smaller by choosing AlSb instead of GaSb.

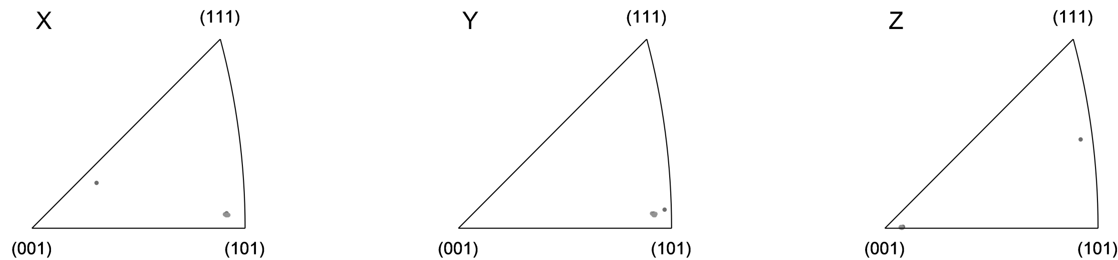

Figure 163: Inversion Pole Figure map with direct projection of the Hillock present on the surface of Y064V.

Figure 163 gives another representation of the inverse pole figure map, involving the direct projection of each orientation detected. In an inverse pole figure map, sample directions in the crystallographic coordinate system are plotted because the axes of the projection sphere are aligned with crystal directions. As noticed before in figure 161 in the X and Y axis, a background pointing in the 101 direction was observed. However, this representation gives more information. Indeed one can notice that according to the X and Y inverse pole figure maps, the background are slightly off the 101 direction. Furthermore, concerning the X direction, we detected a point between the 111 direction and the 001 direction. Concerning the Z direction, it confirms the information previously obtained from the background facing the 001 direction with once again another point was detected between the 111 and 101 directions.

4.4.4 Grain Determination Study

Now that the orientation of the area scanned was determined, another analysis was conducted to try to know whether or not there is some localize misorientation on the surface of Y064V around the hillocks.

In the grain determination process, the misorientation of each pixel with its four (north, south, east and west) neighbors is examined. When the misorientation exceeds the "grain tolerance angle", a boundary is defined. Once all the pixel boundaries are defined, they are regrouped to form grains.

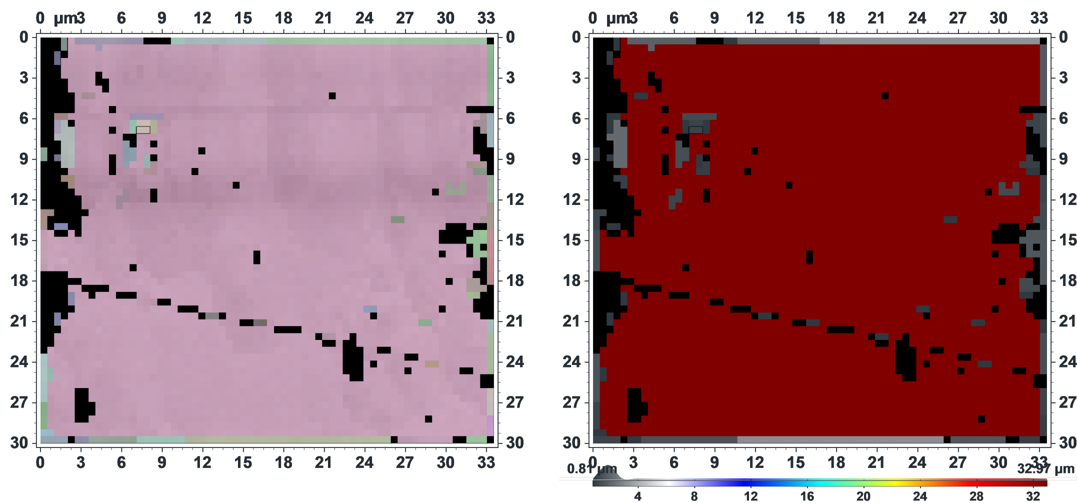

Figure 164: Grain determination map of the hillock present on the surface of Y064V for a tolerance angle of 5 degrees.

In figure 164 for a tolerance angle of 5 degrees, no grains were detected which means that the hillock's misorientations are less than this value.

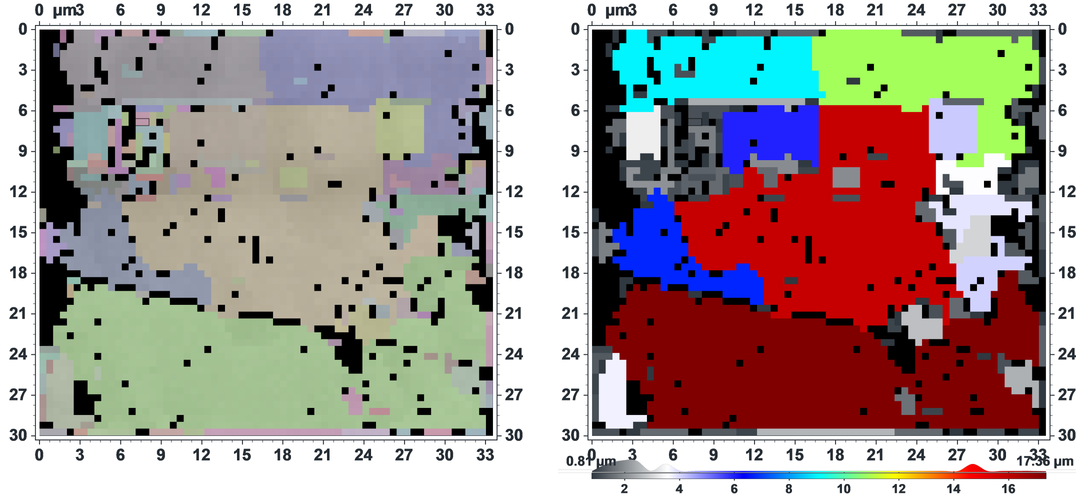

Figure 165: Grain determination map of the hillocks present on the surface of Y064V for a tolerance angle of 3 degrees.

Figure 165 depicts the grain determination map with a tolerance angle of 3 degrees. Relating this map to the band contrast map (fig.160) one can notice that the green area on the left-hand side image or the brown area on the right-hand side image is an area without hillocks. Therefore it makes sense that only one grain for this part of the image was detected. The other grains detected are the grains relative to the hillock. The grain determination map is composed of 6 different grains which means that in this part of the image we have 6 areas with a misorientation angle of 3 degrees. This is a significant piece of information telling that the hillocks have a misorientation angle of 3 degrees in this area.

4.5 Conclusion

Hillocks				
Name	RMS(nm)	Max Height (nm)	X length (μm)	X length (μm)
Y064V	18.0	65.8	5.5	9.5
Y067V	13.5	55	6.2	11.2
Y074V	17.8	23.7	4.1	7.2

Table 5: Hillocks characteristics of the Y series table.

Several years ago, a study of the surface morphology of InSb quantum-well structures on GaAs substrates highlighted the presence of hillocks.[26] A density of hillocks of ca. 2.00 x 10^7 cm^{-2} with a lateral size of 2 μm and an overall height of ca. 20 nm was measured. As shown in table 5, the height of the hillocks is shorter in our study of the interband cascade devices. However, the lateral size is larger.

Name	Background irregularities		Defect Density (cm^{-2})	Number of Stages
	RMS(nm)	Max Height (nm)		
Y064V	2.7	9.0	1.18 x 10^8	8
Y067V	5.8	11.5	2.80 x 10^4	8
Y074V	10.4	4.8	9.50 x 10^4	15

Table 6: Background Irregularities table.

As shown in table 6, the Antimony soaks during the growth process were effective in reducing the density of hillocks on the surface of the sample. If one had to choose a sample as the best one, it would be a hard task because both Y074V and Y067V have pros and cons. Indeed the density of defects is lower in the case of Y067V but the thickness of Y074V is almost 2 times thicker. Therefore it is a normal consequence to have a higher density of defects for Y074V. Concerning the height of the defects on the surface, Y074V is the best sample due to the fact that their height is almost 2 times smaller than the ones present on the surface of Y067V.

5 Conclusion

In the first section of this thesis, the different characterization techniques that were used to analyze the surface condition of three types of semiconductors were explained. We used the Field Emission Scanning Electron Microscope and the Atomic Force Microscope to determine the roughness or height of various defects present on the surface of semiconductors. This enables a clear analysis about which growth parameters affect the surface condition of the semiconductor. Moreover, DIC (Differential Interference Contrast) microscope capabilities provide qualitative information that checks the surface condition from another point of view. Lastly, using an SEM related technique called Electron Backscattered Diffraction, we can relate the texture of a semiconductor to its microstructure providing local misorientations and crystallographic orientations of the defects.

In the second section, we compared two InSb quantum well devices with the same structure. A conclusion was made that the theoretical layer structure that was used for the two samples is marginally inaccurate and results in structures that are marginally strain balanced. The presence of lines due to misfit dislocations was noticed in both samples even though the second sample, B051, has a better surface condition with minimized lines due to misfit dislocations. Future work concerning this two samples would be to do an X-ray diffraction study to determine the concentration of each alloy in the two samples to determine why one sample has a better surface condition.

In the third part, we compared four different GaSb homoepitaxial samples to explore the effects of different growth conditions. The samples were a 1-μm GaSb layer grown on a GaSb substrate. This experimental analysis was aimed at finding the best growth parameters to make the buffer layer as smooth as possible. The best sample of this study was M373, with the highest growth temperature of 498°C and a V/III ratio of 2.5. It had the lowest density of defects on its surface. Another sample of this study, M374, had also interesting properties, with the smoothest background and shallowest irregularities of this study. Unfortunately, a higher density of defect in comparison to M373 was observed due to a lower V/III ratio, which caused the desorption of group V material and increased the metallic droplet density on its surface. Future work concerning this study will be to grow a semiconductor with growth conditions in between M373 and M374, by keeping a high V/III ratio of 2.5 and a high growth temperature close to 490°C.

Lastly, in the fourth section, a study involving three interband cascade photovoltaic prototypes was conducted. Two of them had 8-stages with one employing Antimony soaks during the growth (Y067V) and the other did not (Y064V). The last sample,

Y074V, was a 15-stages device with Antimony soaks during the growth. The effect of the Antimony soak process and of increasing the number of stages in this study was compared. An improvement in the surface condition with the Antimony soak was observed. Indeed the density of hillocks on the surface of Y067V was 50 times smaller than the density of hillocks of Y064V by adding this antimony soak process during the growth. The reason was that the residual Arsenic present in the chamber interfered with the composition of the layer one was trying to grow after an arsenide layer. AlAs or AlAsSb layers were created which made the overall semiconductor not strain balanced. The last sample of this study, Y074V, had also some interesting properties, with a shallower average hillock height and a smaller hillock size observed on its surface. However, a hillock density 5 times higher than Y067V was observed which means that more experiments have to be made to determine the best growth conditions for structures with many stages.

References

[1] Aimo Winkelmann, Carol Trager-Cowan and Austin P. Day, ”Simulation of electron backscatter diffraction patterns”, Ultramicroscopy,107,414, (2007).

[2] Arantxa Vilalta-Clementa, Katrin Gloystein, Nikos Frangis, Principles of Atomic Force Microscopy (AFM), Nanomagnetics AFM Manual, 2008.

[3] B. Z. Nosho, B. R. Bennett, E. H. Aifer and M. Goldenberg, ”Integration of broken-gap heterojunction InAs/GaSb Esaki tunnel diodes on silicon”, J. Cryst. Growth 236,155, (2002).

[4] Ben G. Streetman, Sanjay Kumar Banerjee, Solid State Electronic Devices, Pearson, 2006.

[5] Crystallography365, Classical crystal structures – sphalerite, crystallography365.wordpress.com, 2014.

[6] E. H. Aifer, E. M. Jackson, B. R. Bennett, I. Vurgaftman, J. R. Meyer and G. G. Jernigan, ”Relaxed InAsP layers grown on step graded InAsP buffers by solid source MBE”, Mat. Res. Soc. Symp. Proc., 722,287, (2002).

[7] Robin F. C. Farrow, Molecular Beam Epitaxy, Applications to Key Materials, Noyes Publications, 1995.

[8] Austin Fox, Atomic Force Microscopy Tips and Tricks, openafox.com, 2017.

[9] G. Binnig, C. F. Quate and C. Gerber, ”Atomic Force Microscope”, Physical Review Letters 56,9,930, (1986).

[10] G. T. P. Frigeri, L. Seravalli and S. Franchi, Molecular beam epitaxy: An overview, Comprehensive Semiconductor Science and Technology 3,12, 480, (2011).

[11] J.I. Goldstein, D.E Newbury, J.R. Michael, N.W.M. Ritchie, J.H.J. Scott, D.C. Joy, Scanning Electron Microscopy and X-ray Microanalysis, Third Edition, Kluwer Academic/ Plenum Publishers, 2003.

[12] Marian A. Herman, Helmut Sitter, Molecular Beam Epitaxy Fundamentals and Current Status, Springer-Verlag Berlin Heidelberg, 1996.

[13] Nanoscience Instruments, Scanning Electron Microscopy, www.nanoscience.com, 2019.

[14] Nanoscience Instruments, Scanning Tunneling Microscopy, www.nanoscience.com, 2019.

[15] Oxford Instruments, Electron backscattered diffraction, Oxford Instruments Analytical–technical briefing, 2004.

[16] Oxford Instruments, Electron Backscattered Diffraction, www.ebsd.com, 2019.

[17] K. Klima, M. Kaniewska, K. Reginski, J. Kaniewski, "Oval Defects in the MBE Grown AlGaAs/InGaAs/GaAs and InGaAs/GaAs Structures", Cryst. Res. Technol 34, 5-6,683, (1999).

[18] Preston Larson, Introduction to the SEM class, EM INTRO SEM Class, 2018.

[19] Lee M. Murray, Asli Yildirim, Sydney R. Provence and Dennis T. Norton, "Causes and Elimination of pyramidal defects in GaSb-based epitaxial layers", J. Vac. Sci. Thechnol. B 31,3, (2013).

[20] Victor Mironov, Fundamentals of scanning probe microscopy, sites.google.com/site/vmironovipm/SPM-textbook, 2004.

[21] N. Lokesh, Crystal Analysis: Miller Indices of a Crystal, www.engineeringenotes.com, 2019.

[22] Oxford Instruments NanoAnalysis, Generating Orientation Maps to Present EBSD Data, AZO Materials, 2015.

[23] O. Yastrubchak, T. Wosinski, T. Figielski, E. Lusakowska, B. Pecz and A.L. Toth, "Misfit dislocations and surface morphology of lattice-mismatchedGaAs/InGaAs heterostructures", Physica E 17, 561, (2003).

[24] Olympus, Fundamental Concepts in DIC Microscopy, www.olympus-lifescience.com, 2019.

[25] Rebecca C. Hildyard, Sergio Llana-Funez, John Wheeler, Daniel R. Faulkner and David J. Prior, "Electron Backscatter Diffraction (EBSD) Analysis of Bassanite Transformation Textures and Crystal Structure Produced from Experimentally Deformed and Dehydrated Gypsum", J. Petrology 52,839, (2011).

[26] S. J. Chung, M. A. Ball, S. C. Lindstrom, M. B. Johnson, and M. B. Santos, "Improving the surface morphology of InSb quantum-well structures on GaAs substrates", J. Vac. Sci. Technol. B 18,1583, (2000).

[27] Sergey Smirnov, "Critical Thickness and Dislocations", J. Appl. Phys.95, 12, (2019).

[28] Anandh Subramaniam, "Critical thickness of equilibrium epitaxial thin films using finite element method", www.iue.tuwien.ac.at, 2004.

[29] Susan Swapp, University of Wyoming, Electron Backscatter Diffraction (EBSD), serc.carleton.edu, 2019.

[30] Warwick, Critical Thickness, warwick.ac.uk, 2010.

[31] Wenxiang Huang, Lin Lei, Lu Li, Jeremy A. Massengale, Rui Q. Yang, Tetsuya D. Mishima, and Michael B. Santos, "Enhanced collection efficiencies and performance of interband cascade structures for narrow bandgap semiconductor thermophotovoltaic devices", J. Appl. Phys. 124, 023101, (2018).

[32] Wikimedia, Molecular Beam Epitaxy, commons.wikimedia.org, 2019.

[33] Robert A. Wilson and Heather A. Bullen, Basic Theory Atomic Force Microscopy (AFM), Nanomagnetics AFM Manual, 2019.

[34] Winson C. H. Kuo, Martha Briceno and Dogan Ozkaya, "Characterisation of Catalysts Using Secondary and Backscattered Electron In-lens Detectors", Platinum Metals Rev.58,2,106, (2014).

[35] Chris Woodford, Molecular Beam Epitaxy, www.explainthatstuff.com, 2018.

[36] R. Q. Yang, "Infrared Laser based on Intersubband Transitions in Quantum Wells", Superlattices and Microstructures 17,77, (1995).

[37] Hao YE, Optimization of InAs (001) layers grown by Molecular Beam Epitaxy, MS Thesis, University of Oklahoma, 115, 2012.

Appendices

A Electron Backscattered Diffraction of a Hole Droplet on the surface of M374

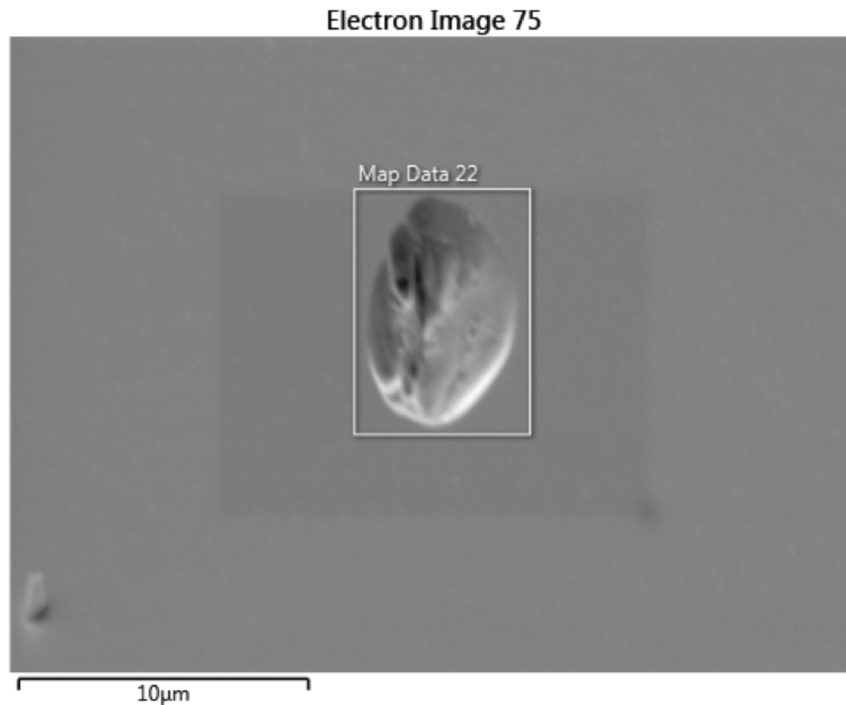

Figure 166: Secondary image of the first hole droplet on the surface of M374 used for the EBSD analysis.

Figure 166 shows a hole droplet on the surface of M374 using secondary electrons. Many irregularities inside the hole were noted.

A.1 Quality of the scan

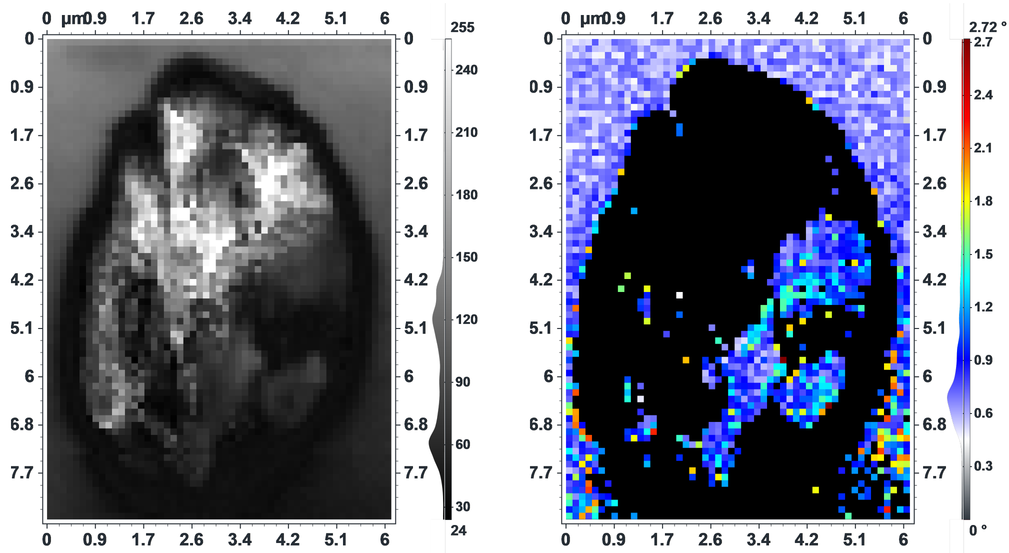

Figure 167: Mean Angular Deviation (MAD) map and Band contrast Map of the first Hole Droplet taken on the surface of M374.

As seen in figure 167, from the band contrast vertical greyscale bar, two different greyscale values were obtained. One of them, corresponding to the background at a greyscale value of 120, which is very close to the median value of 122. The other peak at 60 corresponds to the dark edges around the droplet. Indeed as seen previously for the metallic droplet, the edges of the defect suffer from a shadow effect. No information was transmitted from the incoming electrons since they were not reflected on the phosphor screen of the EBSD camera.

Concerning the Mean Angular Deviation (MAD) map, an average misfit angle of 0.6 degrees was observed, close to the optimum misfit angle of 0.5 and therefore considered as an excellent fit. Considering the random orientation of the matter inside the hole and the omnipresence of shadow effect throughout the scan, one can conclude that the band contrast map and the MAD map confirm that the scan is reliable.

A.2 Orientation Study

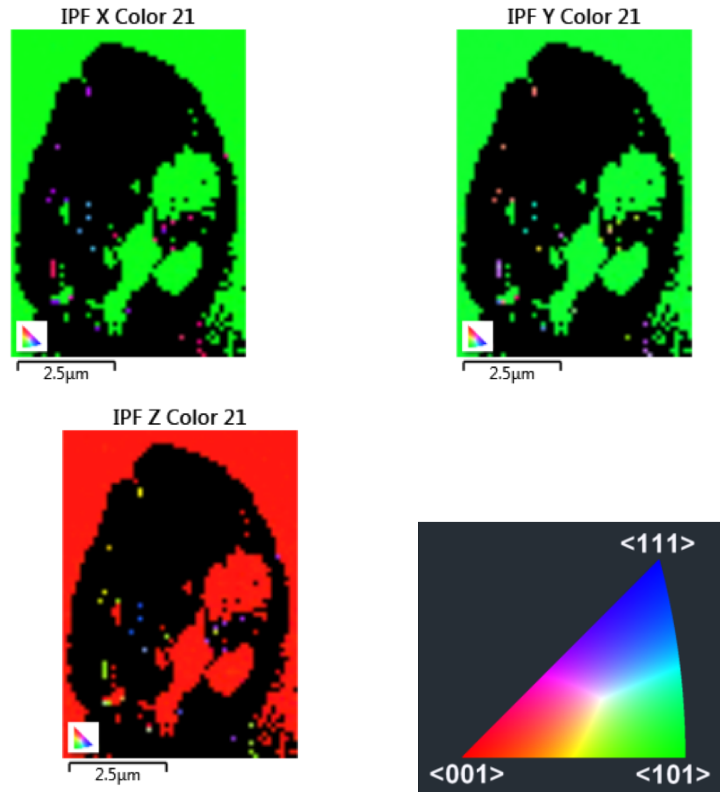

Figure 168: Inversion Pole Figure X,Y,Z of the first hole droplet.

Figure 168 depicts the inverse pole figure maps related to the three orientations X, Y, Z. On the X and Y inverse pole figure maps, the overall background in both cases is pointing in the 101 direction. Concerning the Z inverse pole figure map, a direction for the background pointing in the 001 direction was noted.

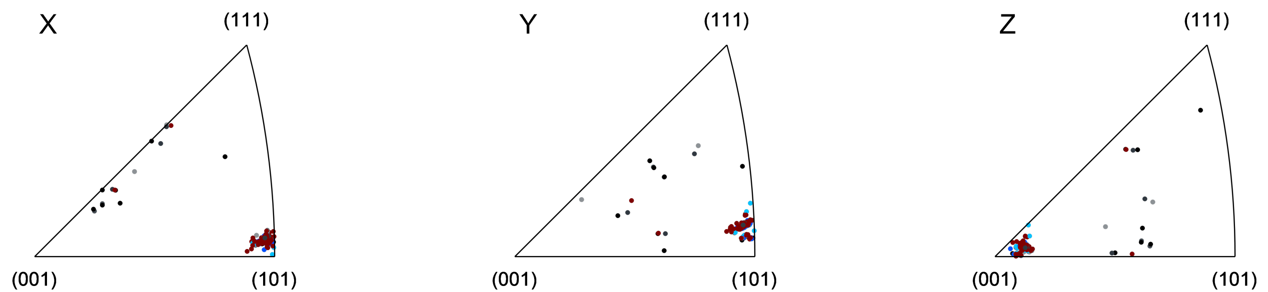

Figure 169: Inversion Pole Figure map with direct projection of the first hole droplet.

Figure 169 presents accurate information of the X,Y,Z orientations of the hole droplet.

From the previous figure, figure 168, an overall background pointing in the 101 direction concerning the X direction was observed. Accordingly, in the inversion pole figure map along the X direction, the group of points near the 101 direction corresponds to the background and the points in between the 001 and 111 directions are the irregularities inside the droplet. Using the same reasoning for the Y map, the group of points spread in the IPF map are the orientation detected inside the hole, which do not have a proper orientation as observed. Finally concerning the Z-map, the group of points near the 001 direction is the background and the others are the orientations detected inside the hole, mostly situated between the 001 and 101 directions.